

NUMERICAL SIMULATIONS OF THE FORMATION
OF LARGE-SCALE STRUCTURE OF THE UNIVERSE

Dissertation der Fakultät für Physik
der
Ludwig-Maximilians-Universität München

vorgelegt von Naoki Yoshida
aus Chiba, Japan

München, den 4. Juli 2001

1. Gutachter: Prof. Dr. Simon D. M. White
2. Gutachter: Prof. Dr. Ralf Bender

Tag der mündlichen Prüfung: 25. Februar 2002

CONTENTS

1	Introduction	1
1.1	General relativity and cosmology	2
1.2	The Friedmann models	3
1.2.1	Perfect fluid models	4
1.2.2	Cosmological constant	5
1.2.3	Evolution of the density parameter	5
1.2.4	Growth of inhomogeneities in an expanding universe	6
1.2.5	The Zel'dovich approximation	7
1.3	Dark matter	9
1.4	Inflationary universe and the density fluctuation spectrum	11
1.4.1	Primeval fluctuations in the inflationary universe	11
1.4.2	Transfer function	12
1.5	Hydrodynamics and dissipation	13
1.5.1	Smoothed Particle Hydrodynamics	13
1.5.2	Cooling	15
1.5.3	Star formation and feedback	15
1.6	Clustering of galaxies and bias	17
1.6.1	Correlation functions and the power spectra	17
1.6.2	Biased galaxy formation	18
1.7	Cosmic microwave background radiation	19
1.7.1	The 3-K radiation	19
1.7.2	Anisotropy mechanisms	19
1.8	Outline	21
2	Statistics of galaxy clustering by pencil-beam surveys	23
2.1	Introduction	24
2.2	N -body simulation	26
2.3	Galaxy selection	27
2.3.1	Lagrangian Bias	29
2.4	Survey strategy	34
2.4.1	Geometry	34
2.4.2	Radial selection	35
2.4.3	Peculiar velocities	35
2.5	Galaxy distribution and power spectrum analysis	36
2.5.1	One-dimensional distribution	36

2.5.2	Pairwise separation histograms	45
2.5.3	Power spectra	45
2.6	PG Δ -test	50
2.7	Supercluster statistics	51
2.8	Discussion and conclusion	55
3	Self-interacting dark matter	57
3.1	Introduction	58
3.2	Crisis on small scales...?	59
3.3	Strongly self-interacting dark matter	60
3.3.1	Scattering with a large cross-section	60
3.3.2	The N -body/SPH simulation	60
3.3.3	Matter distribution	61
3.3.4	Substructure abundance	62
3.3.5	Discussion	66
3.4	Weakly self-interacting dark matter	69
3.4.1	Scattering with a finite cross-section	69
3.4.2	The N -Body/Monte-Carlo simulations	69
3.4.3	Matter distribution	70
3.4.4	Substructure abundance	72
3.4.5	Summary and discussion	75
3.5	Lensed arcs as a constraint on the scattering cross-section	77
4	The Sunyaev-Zel'dovich effect	81
4.1	Theory	82
4.1.1	The thermal Sunyaev-Zel'dovich effect	82
4.1.2	The kinematic Sunyaev-Zel'dovich effect	85
4.2	Non-Gaussian CMB temperature fluctuations	86
4.2.1	Introduction	86
4.2.2	The simulations	86
4.2.3	Kinematic effect	87
4.2.4	Analytic model	93
4.2.5	Thermal effect	99
4.2.6	Mean relation between τ and t_{SZ}	100
4.2.7	Distribution of τ and t_{SZ}	102
4.2.8	Discussion	105
4.3	The SZ power spectrum	111
4.3.1	Map making	111
4.3.2	The angular power spectrum	112

4.3.3	Discussion	115
5	Gas cooling and the formation of galaxies in clusters	119
5.1	Introduction	120
5.2	The N -body/SPH simulations	121
5.3	Cluster properties	123
5.4	Baryons in dark matter halos	128
5.4.1	Gas mass fraction	128
5.4.2	Galaxies in the SPH simulation	129
5.5	Semi-analytic modelling of galaxy formation	133
5.5.1	Gas cooling	133
5.5.2	Stripped down semi-analytic model	133
5.5.3	Galaxies in the semi-analytic model	134
5.6	Object-by-object basis comparison	136
5.7	Summary and discussion	145
6	Concluding remarks	147
6.1	Summary and conclusions	148
6.2	Future prospect	150

DEUTSCHE ZUSAMMENFASSUNG

In dieser Arbeit beschäftige ich mich mit einer Reihe verwandter Aspekte der Theorie der Entstehung von großräumiger Strukturen in Universum.

DIE “PERIODISCHE” VERTEILUNG DER GALAXIEN

Im Jahr 1990 beobachteten Broadhurst, Ellis, Koo, und Szalay, daß Galaxien in regelmäßigen Abständen verteilt sind. Die Beobachtung war sehr umstritten, und die Existenz der periodische Verteilung ist seit über zehn Jahren ein langstehendes Problem in der Kosmologie. In Kapitel 2 präsentiere ich eine Arbeit über die großräumige Materieverteilung in einem Universum mit kalter dunkler Materie. Die Ausgaben von sehr großen kosmologischen N -Körper Simulationen des Hubble Volumens werden dabei benutzt. Die Hubble Volumen Simulationen machen es zum ersten Mal möglich, direkt zu prüfen, ob solche offensichtlichen periodische Strukturen im kalten dunklen Materie-Universum gefunden werden. Die so genannte “lightcone” Ausgabe schließt die räumliche Entwicklung der Materieverteilung ein, und ist deshalb ideal geeignet, mit den Beobachtungen bei hoher Rotverschiebung verglichen zu werden. Im Verlauf der Arbeit wird auch der “Galaxien-Bias” quantitativ untersucht und eine empirische Zuordnung des Galaxien-Bias wird angewendet, um ‘Galaxien-Kataloge’ aus der Simulations Ausgabe zu extrahieren.

Etwa zwei tausend Realisierungen der simulierten ein-dimensionalen Galaxienverteilung im Modell-Universum werden erstellt. Durch Vergleich mit den Beobachtungsdaten wird die *a priori* Wahrscheinlichkeit geschätzt, daß die populären kosmologischen Modelle ähnliche großräumige (auf einigen hundert Millionen Lichtjahren) Strukturen produzieren. Das Resultat zeigt, daß diese Wahrscheinlichkeit kleiner als 10^{-3} ist.

DUNKLE MATERIE

Die derzeit favorisierten kosmologischen Modellen für die Entstehung von Strukturen im Universum nehmen an, daß ein Großteil der Masse im Universum aus dunkler Materie besteht, bei der es sich etwa um ein lediglich schwach wechselwirkendes Elementarteilchen handeln könnte. Es gibt viele indirekte Hinweise auf ihre Existenz, aber die Eigenschaften der dunklen Materie sind noch unbekannt. Die Kosmologien, die von kalter dunkler Materie dominiert sind, erklären erfolgreich eine Reihe von Beobachtungen auf großen Skalen. Jedoch sind in den letzten Jahren Hinweise gefunden worden, daß die Standardmodelle, die auf kalter kollisionsfreier dunkler Materie basieren, mit Beobachtungen auf den galaktischen und sub-galaktischen Skalen in Konflikt stehen. Die Studien in Kapitel 3 werden durch den Vorschlag motiviert, daß eine Erklärung für die Diskrepanz in der grundlegenden Physik gesucht werden sollte. Vor kurzem sorgte eine wiederbelebte Theorie der selbst-wechselwirkenden dunklen Materie für ziemlich viel Interesse der Astrophysiker, denn damit ist eine Möglichkeit gegeben, daß die dunkle Materie durch Selbst-Wechselwirkung weithin bekannte Konflikte lösen kann. Es wird vorausgesagt, daß dieses Modell mit der beobachteten Menge dunkler Materie in den Zentren von Zwerggalaxien besser übereinstimmt als das der kollisionsfreien Teilchen.

Motiviert durch diese Idee, studiere ich wie solche Änderungen der Eigenschaften der dunklen Materie die interne Struktur der nichtlinearen Objekte ("dark halos") ändert. Ich führe Simulationen von Galaxienhaufen mit dem GADGET SPH/ N -Körper Code durch. Als zwei Extremfälle, untersuche ich die Dynamik von stoßfreier dunkler Materie und ganz stoßiger ("flüssiger") dunkler Materie. Der Gebrauch einer identischen Ausgangsmaterieverteilung ermöglicht es, einen klaren Unterschied der inneren Struktur der dunklen Materie-Halos nachzuweisen. Es wird gefunden, daß fluide dunkle Materie zu hohen Dichten in den Zentren der Galaxienhaufen voraussagt. Deshalb ist fluide dunkle Materie keine vielversprechende Lösung. Weitere Simulationen für eine ganze Reihe von verschiedenen Streuquerschnitten werden durchgeführt. Diese wurden dabei so gewählt, daß die Teilchen der dunklen Materie im Zentrum der Galaxienhaufen während der Zeitspanne, in der sich das Universum entwickelt, wenige, einige zehn, oder etwa hundert Kollisionen haben. Die Kollisionen der Teilchen beeinflussen die Struktur des Galaxienhaufens deutlich. Kollisio-

nen führen im allgemeinen zu runderen und weniger konzentrierten Galaxienhaufen. Schon wenige Kollisionen im Laufe der Entwicklung des Universums sind genug, um die Wirksamkeit der Galaxienhaufen als Gravitationslinsen so stark zu reduzieren, daß sie derart eindrucksvolle Bögen, wie sie beobachtet werden, nicht mehr produzieren können. Damit bietet der Gravitationslinseffekt nicht nur eine Möglichkeit, bestimmte intrinsische Eigenschaften der dunklen Materie zu limitieren, sondern sogar zu messen.

DER SUNYAEV-ZEL'DOVICH EFFEKT

Heißes Plasma in Galaxienhaufen bewirkt eine spektrale Verzerrung der kosmischen Hintergrundstrahlung (CMB, englisch "cosmic microwave background") durch Compton Streuung. Der so genannte Sunyaev-Zel'dovich Effekt wird als Absenkung in der Temperatur des CMB beobachtet. In einem dritten Schwerpunkt meiner Arbeit studiere ich die Sekundären Anisotropien der kosmischen Hintergrundstrahlung durch den thermischen und kinetischen Sunyaev-Zel'dovich Effekt von Galaxienhaufen. Ich benutze die Ausgabe von sehr großen kosmologischen Simulationen und mache Himmelskarten der Temperaturschwankungen des CMB durch simulierte Galaxienhaufen. Ein analytisches Modell wird entwickelt, um die Verteilung der Höhe in den CMB Temperaturschwankungen vorauszusagen. Das Modell nimmt an, daß die Verteilung der baryonischen Materie ähnlich wie die der dunkle Materie ist (aufgrund der großen Masse von Galaxienhaufen mußte die Materie aus einer sehr großen Region des frühen Universums kollabieren), und daß Pekuliargeschwindigkeiten von Galaxienhaufen durch die lineare Theorie beschrieben werden können. Die Vorhersage des Modells wird mit dem Ergebnis der numerischen Simulation verglichen. Es zeigt sich, daß das Modell eine erfolgreiche Beschreibung der Verteilung der Höhe des Sunyaev-Zel'dovich Effekt liefert. Diese Verteilung kann daher für jedes vorgegebene Materiedichtefluktuation im frühen Universum gerechnet werden. Damit ist es möglich, die Materieverteilung innerhalb der Gaußschen Modelle einzuschränken. Nicht-Gaußsche Signaturen in den Temperaturschwankungen des CMB werden auch untersucht. Ich finde, daß der Sunyaev-Zel'dovich Effekt bedeutende nicht-Gaußsche Signaturen in der CMB hinterläßt.

STRAHLUNGSKÜHLUNG DES GASES IN GALAXIENHAUFEN

Die neuen Röntgenstrahlbeobachtungen mit den Satelliten *Chandra* und *XMM Newton* liefern viele interessante Daten, die vorschlagen, daß die Wechselwirkung zwischen Galaxien und dem Intraclustermedium sehr wichtig ist. Deshalb ist die Einbeziehung der gasdynamische Prozesse in frühen Stufen der Entwicklung der Galaxienhaufen notwendig.

In Kapitel 5 studiere ich die Strahlungskühlung des Gases und die Entstehung von Galaxien in Galaxienhaufen. Ich führe eine Reihe hochaufgelöster Simulationen durch, die Gasdynamik durch ein teilchenbasiertes hydrodynamisches Verfahren (SPH, englisch Smoothed Particle Hydrodynamics) sowie Strahlungskühlung des Gases einschließen. Die Dynamik in Galaxienhaufen wird hauptsächlich durch Gravitation, die aus der Verteilung der dunkler Materie resultiert bestimmt. Um jedoch die Entstehung und Entwicklung von Galaxien zu studieren, müssen wir auch die Verteilung der Baryonen und ihr zeitabhängiges Verhalten kennen. Die semi-analytischen Modelle der Galaxienentstehung in ihrer jetzigen Ausgestaltung verwenden viele vereinfachte, jedoch physikalisch motivierte Beschreibungen für die Strahlungskühlung des Gases, die Sternentstehung, u.s.w. Unter diesen komplizierten physikalischen Prozessen ist die Strahlungskühlung des Gases der wichtigste und noch verhältnismäßig gut verstandene Prozeß. Ich studiere wie sich das Gas in Halos dunkler Materie verhält, und ich prüfe die Annahmen in den populären semi-analytischen Modellen explizit in Vergleichen mit der hochaufgelösten hydrodynamischen Simulation. Es zeigt sich, daß die Beschreibung in den semi-analytischen Modellen weitgehend übereinstimmende Ergebnisse wie die direkte Simulation ergibt. Trotzdem wird eine kleine Abweichung in der Masse der kalten Gases gefunden. Dieses Ergebnis kann zur Kalibration benutzt wird, um die analytischen Modelle weiter zu verbessern.

Teile dieser Arbeit (Kapitel 2 und 3) sind in den Artikeln Yoshida et al. (2001), Yoshida, Springel, White, & Tormen (2000a) und Yoshida, Springel, White, & Tormen (2000b) bereits veröffentlicht worden oder befinden sich im Druck.

CHAPTER 1

Introduction

1.1 GENERAL RELATIVITY AND COSMOLOGY

This chapter gives an introduction and the basic theoretical foundations of modern cosmology. I begin with a brief description of General Relativity. Its application to the dynamics of an expanding universe is described in some detail.

Only four kinds of force have so far been discovered: gravity, electromagnetism, the strong force, and the weak force. Gravity is the simplest force in the sense that it acts on any kind of matter, and it is the strongest on large scales –on scales of galaxies, galaxy clusters–, so the most important part in cosmology is a theory of gravity. In the context of Einstein’s General Theory of Relativity the force is translated to being a property of space-time. The *metric* contains all the information about the space-time, and Einstein’s equations relate the geometrical properties, expressed by the metric tensor $g_{ij}(x_k)$, to the matter content of the universe, expressed by the energy-momentum tensor $T_{ij}(x_k)$. The Einstein equations are:

$$R_{ij} - \frac{1}{2}g_{ij}R = \frac{8\pi G}{c^4}T_{ij}, \quad (1.1)$$

where R_{ij} and R are the Ricci tensor and Ricci scalar, respectively, G is the gravitational constant, and c is the speed of light. For a perfect fluid, the energy-momentum tensor is given by

$$T_{ij} = (p + \rho c^2)U_i U_j - p g_{ij}, \quad (1.2)$$

where p is the pressure, ρc^2 is the energy density and U_k is the fluid four-velocity.

The simplest approach we can take to obtain a solution of equation (1.1) is to assume that the Universe is homogeneous and isotropic on large scales; the assumption usually known as the *Cosmological Principle*. We begin by investigating the geometrical properties of such a homogeneous and isotropic universe. The most general space-time metric describing a homogeneous and isotropic universe is known to be of the form

$$ds^2 = (cdt)^2 - a^2(t)\left[\frac{dr^2}{1 - Kr^2} + r^2(d\theta^2 + \sin^2\theta d\phi^2)\right], \quad (1.3)$$

where we have used spherical polar coordinates (r, θ, ϕ) . The coordinates are *comoving* with the expansion of the Universe, whose spatial extent grows proportional to the dimensionless expansion parameter $a(t)$. The curvature parameter K is a constant determining the global geometry of the Universe, conventionally referred to as closed ($K > 0$), flat ($K = 0$), and open ($K < 0$). The metric (1.3) is called the *Friedmann-Robertson-Walker metric*.

1.2 THE FRIEDMANN MODELS

For a homogeneous and isotropic universe with matter content specified by pressure p and density ρ , the mathematics for relating the scale factor a and the variables p and ρ becomes simple. In this case, the Einstein equations with the Friedmann-Robertson-Walker metric reduce to just two equations:

$$H^2 := \left(\frac{\dot{a}}{a}\right)^2 = \frac{8\pi G}{3}\rho - \frac{Kc^2}{a^2} + \frac{\Lambda c^2}{3}, \quad (1.4)$$

$$\frac{\ddot{a}}{a} = -\frac{4\pi G}{3}\left(\rho + 3\frac{p}{c^2}\right) + \frac{\Lambda c^2}{3}. \quad (1.5)$$

Equation (1.4) is often referred to as the Hubble equation. We shall now introduce commonly used quantities, termed *cosmological parameters*:

$$\text{the Hubble constant:} \quad H_0 = \left(\frac{\dot{a}}{a}\right) \Big|_{t=t_0} \quad (1.6)$$

$$\text{the critical density:} \quad \rho_c = \frac{3H_0^2}{8\pi G} \quad (1.7)$$

$$\text{the density parameter:} \quad \Omega_0 = \frac{\rho_0}{\rho_c} \quad (1.8)$$

$$\text{the cosmological constant:} \quad \Lambda. \quad (1.9)$$

The global geometry and the dynamics of the universe are determined by these cosmological parameters via equations (1.4) and (1.5), and therefore, measurement and determination of the values is one of the fundamental goals of astronomical observations.

Table 1.1 Equation of state

σ	Form of energy
0	Nonrelativistic matter (“dust”)
+1/3	Relativistic matter (e.g. neutrinos) Radiation (photons, gravitational waves)
-1	Cosmological constant

If one takes the adiabatic expansion of the universe into account, equation (1.5) can be recovered from equation (1.4). It will become clear later in this chapter that using the energy equation

$$d(\rho c^2 a^3) = -p da^3 \quad (1.10)$$

or equivalently

$$\dot{\rho} + 3 \left(\rho + \frac{p}{c^2} \right) \frac{\dot{a}}{a} = 0 \quad (1.11)$$

is more useful for the description of various matter contents in the universe.

1.2.1 Perfect fluid models

The Friedmann equations give a full description of the relationship between the geometric variable a and the matter variables p, ρ . To obtain a solution to the dynamics of the universe, another equation which relates p to ρ is necessary – an equation of state. In cosmology, a generally useful form for the equation of state is

$$p = \sigma \rho c^2. \quad (1.12)$$

For a wide range of cases of interest σ is in fact constant. Table 1.1 shows the values of σ for various form of energy density.

It is straightforward to solve equation (1.11) for a matter component with its equation of state constant σ :

$$\rho a^{3(1+\sigma)} = \text{constant}. \quad (1.13)$$

In particular, for a matter-dominated *dust* universe ($\sigma = 0$), the density evolution is described by

$$\rho a^3 = \text{constant}, \quad (1.14)$$

and for a radiation-dominated universe ($\sigma = 1/3$),

$$\rho a^4 = \text{constant}. \quad (1.15)$$

1.2.2 Cosmological constant

We have been using the cosmological constant Λ somewhat ambiguously without physical definition. In this section, before describing the evolution of the density parameter, we give a brief introduction to the cosmological constant. Einstein (1917) modified the field equation (1.1) by introducing an additional term Λ

$$R_{ij} - \frac{1}{2}g_{ij}R - \Lambda g_{ij} = \frac{8\pi G}{c^4}T_{ij}. \quad (1.16)$$

Einstein's original idea was to obtain a static cosmological model, which he later called "the biggest blunder in my life". Equation (1.16) represents the most general modification of the Einstein equations, because, with the modification, a tensor T_{ij} in equation (1.16) can still be constructed from the metric g_{ij} and its first and second derivatives. Although a non-vanishing Λ is not motivated from fundamental physics, a positive and small value of Λ is favoured from observations of Type Ia supernovae (Riess et al. 1998). The smallness of this value still remains a deep mystery within the standard framework of particle physics (see Carroll, Press & Turner 1992 for an excellent review).

The modification in equation (1.16) is equivalent to considering a matter content with $\sigma = -1$, often referred to as the vacuum energy, so that its energy-momentum tensor is given by

$$T_j^i = \Lambda \delta_j^i. \quad (1.17)$$

This vacuum energy contributes $\Omega_\Lambda = 8\pi G\Lambda/3H_0^2$ to the critical density at the present epoch. Currently popular models assume that about 70 per cent of the energy in the present Universe is in the form of the vacuum energy: $\Omega_\Lambda \approx 0.7$ (Ostriker & Steinhardt 1995).

1.2.3 Evolution of the density parameter

In the beginning of this section we introduced the density parameter Ω_0 to refer to the value at the present time. Similarly, we define the density parameter at an arbitrary time as

$$\Omega(a) = \frac{\rho(a)}{[3H^2(a)/8\pi G]}. \quad (1.18)$$

The density $\rho(a)$ is given by equation (1.13). For a “dust” universe with a cosmological constant, the Hubble parameter $H(a)$ is given by

$$H^2(a) = H_0^2 [\Omega_0 a^{-3} + (1 - \Omega_0 - \Omega_\Lambda) a^{-2} + \Omega_\Lambda], \quad (1.19)$$

and the density parameter is expressed as

$$\Omega(a) = \frac{\Omega_0}{\Omega_0 + a(1 - \Omega_0 - \Omega_\Lambda) + a^3 \Omega_\Lambda}. \quad (1.20)$$

1.2.4 Growth of inhomogeneities in an expanding universe

We assume for the moment that the Universe is dominated by pressureless material. Let us work with a comoving coordinate $\mathbf{x} = \mathbf{r}/a$ and the peculiar velocity $\mathbf{v} = a d\mathbf{x}/dt$, and define the overdensity with respect to the global mean $\bar{\rho}$ as

$$\rho(\mathbf{x}, t) = \bar{\rho}(t) \cdot (1 + \delta(\mathbf{x}, t)). \quad (1.21)$$

The continuity equation, the Euler and the Poisson equations can be written

$$\frac{\partial \delta}{\partial t} + \nabla \cdot \mathbf{v} + \nabla \cdot (\mathbf{v} \delta) = 0, \quad (1.22)$$

$$\frac{\partial \mathbf{v}}{\partial t} + (\mathbf{v} \cdot \nabla) \mathbf{v} + 2 \frac{\dot{a}}{a} \mathbf{v} = -\frac{1}{a^2} \nabla \phi, \quad (1.23)$$

$$\nabla^2 \phi / a^2 = 4\pi G \bar{\rho} \delta, \quad (1.24)$$

where ϕ denotes the gravitational potential. Assuming that the perturbations in the early Universe are very small, we can combine the above equations and obtain the linear growth equation

$$\ddot{\delta} + 2 \frac{\dot{a}}{a} \dot{\delta} - 4\pi G \bar{\rho} \delta = 0. \quad (1.25)$$

Equation (1.25) can be solved easily for $\Omega_0 = 1$. The expansion factor grows as $a \propto t^{2/3}$ and the mean density of the universe decreases as $\bar{\rho} \propto t^{-2}$. Then equation (1.25) becomes

$$\ddot{\delta} + \frac{4}{3t} \dot{\delta} - \frac{2}{3t^2} \delta = 0. \quad (1.26)$$

Solutions for equation (1.26) are

$$\Delta \propto t^{2/3} \propto a \quad (\text{growing mode}) \quad (1.27)$$

$$\propto t^{-1} \propto a^{-3/2} \quad (\text{decaying mode}). \quad (1.28)$$

Note that for any value of Ω_0 , $\Omega(a)$ asymptotically approaches unity when $a \rightarrow 0$. Therefore the solution given in the above is valid at a sufficiently early epoch, although it fails at epoch earlier than $z \simeq 1000$ because radiation becomes dominant and the above equations are no longer valid then. For a general cosmology, the growing solution $D(t)$ is obtained by integrating

$$D(t) = H(t) \int_0^t \frac{dt'}{a^2(t')H^2(t')}. \quad (1.29)$$

1.2.5 The Zel'dovich approximation

Once perturbations grow beyond the linear regime, it becomes difficult to treat the density evolution analytically. Although a full treatment of the non-linear regime requires numerical simulations, an approximation scheme developed by Zel'dovich (1970) proves remarkably successful to the regime where caustics form and the associated gas dynamics or other dissipative processes are important. The Zel'dovich approximation is a commonly used technique to set up initial conditions for N -body simulations, so we describe the method in this section.

Let the initial Lagrangian coordinate of a particle in an unperturbed distribution be \mathbf{q} . Then each particle is subject to a displacement corresponding to a density perturbation. In the Zel'dovich approximation the Eulerian coordinate of the particle at time t is

$$\mathbf{r}(t, \mathbf{q}) = a(t)[\mathbf{q} - b(t)\nabla_{\mathbf{q}}\Phi_0(\mathbf{q})], \quad (1.30)$$

where $\mathbf{r} = a(t)\mathbf{x}$ with \mathbf{x} being a comoving coordinate. The velocity field is obtained from equation (1.30),

$$\mathbf{v} = a \frac{d\mathbf{x}}{dt} = -ab\nabla_{\mathbf{q}}\Phi_0(\mathbf{q}) \quad (1.31)$$

The quantity $\Phi_0(\mathbf{q})$ is related to, via the Poisson equation, the density perturbation in the linear regime:

$$\delta = b\nabla_{\mathbf{q}}^2\Phi_0. \quad (1.32)$$

Particles in the Zel'dovich approximation execute a motion on straight line trajectories.

To calculate the density evolution we need only the volume transformation between the Lagrangian and Eulerian frames, because mass is conserved:

$\rho(\mathbf{r}, t)d^3r = \langle \rho(t_i) \rangle d^3q$. The Jacobian $\partial\mathbf{r}/\partial\mathbf{q}$ yields

$$\rho(\mathbf{q}, t) = \bar{\rho} \left(1 - \alpha_1 \frac{b}{a}\right)^{-1} \left(1 - \alpha_2 \frac{b}{a}\right)^{-1} \left(1 - \alpha_3 \frac{b}{a}\right)^{-1}, \quad (1.33)$$

where α_i are the eigenvalues of the distortion tensor. Density evolution of a triaxial matter distribution is illustrative. The collapse is expected to occur first along the shortest axis (q_1 for example), to form a flattened, sheet-like structure termed ‘‘pancake’’ in a time given implicitly by $\alpha_1 b(t) = a(t)$. Only if two negative eigenvalues are nearly equal in magnitude, the collapse occurs to a quasi one-dimensional ‘‘filament’’.

It can be proven that $b(t)$ must be proportional to the linear growth factor $D(t)$ from the requirement that the first order Lagrangian perturbation theory agree with the first order Eulerian perturbation theory. From equation (1.31), the growth of peculiar velocities is

$$\mathbf{v} \propto a\dot{D} = aH(a)f(\Omega), \quad (1.34)$$

where the logarithmic derivative $f(\Omega)$ is given by

$$f(\Omega) \equiv \frac{dD}{da} \frac{a}{D} \approx \Omega^{0.6}(a). \quad (1.35)$$

The last approximation is derived by Peebles (1980) (see also Lahav et al. 1991).

1.3 DARK MATTER

The most convincing observational evidence for the existence of dark matter involves galactic dynamics. The inferred amount of mass from observed rotation curves of spiral galaxies is much larger, typically a few to ten times larger, than that of luminous matter. One may simply speculate that most of the matter might be just dark, hence not necessarily some exotic matter. Such *baryonic dark matter* can explain, at least partially, the mass-to-light discrepancy on galactic scales. On larger scales, however, the problem seems harder to solve as explained in the following argument. The contribution from baryonic material to the density of the present-day universe is estimated by comparing the observed relative abundances of light elements such as deuterium and helium with respect to hydrogen, against the predictions from primordial nucleosynthesis. The latest measurement suggests (Tytler et al. 2000)

$$\Omega_b h^2 = 0.019 \pm 0.0024. \quad (1.36)$$

By applying Newton’s law to the motion of galaxies in clusters assuming that the system is virialised, one infers a universal mass density of $\Omega \approx 0.1 - 0.3$, which cannot be accounted for by baryonic material. Gravitational lensing offers a way to *map* the mass distribution in galaxy clusters; nowadays routinely observed giant arcs (distorted images of the background galaxies) are a strong evidence for mass concentration in the centres of clusters; the inferred amount of mass is much larger than the total mass of luminous matter within the region. Another theoretical reason for the existence of dark matter is provided by the fluctuations in the microwave background radiation. Gravitational instability alone cannot make the rich structures as we see today from the smooth initial density fluctuations if there is no other additional material than baryons. A simple and generally accepted solution is to introduce some kind of *dark* matter, which neither emit nor absorb electromagnetic radiation.

Historically dark matter candidates are classified according to their velocities when they decoupled from other materials in the early universe. We list their properties in terms of structure formation.

- Hot dark matter: Neutrinos are the best candidate since they do exist and have a non-vanishing mass. However, neutrino’s relativistic velocity (hence “hot”) at the decoupling epoch is so high that the small fluctu-

ations that could form galaxies are washed out. Conventional neutrino-dominated universe models have a number of inconsistencies with the observed properties of large-scale structure, and the hot dark matter models with density fluctuations generated by inflation were ruled out in the pioneering work of White, Frenk & Davis (1983).

- Warm dark matter: There is no natural candidate for warm dark matter within the standard models of particle physics (Schaeffer & Silk 1988). However, recent debates on the viability of the standard models that involve collisionless cold dark matter motivated re-examination of warm dark matter models. In warm dark matter models density fluctuations on small scales are suppressed due to free-streaming, which appear to be preferable to cold dark matter models. Various constraints have been made to warm dark matter models (Croft et al. 1999, Bode et al. 2000, Haiman et al. 2000), and it appears unlikely that the warm dark matter models within the allowed range of the particle mass resolve the possible problems.
- Cold dark matter: Because of natural motivation from the standard models of particle physics and its success in reproducing the observed properties of large scale structure (Bahcall et al. 1999), cold dark matter remains the best candidate. (Although the lack of experimental evidence for particles which can form the cold dark matter makes the scenario still speculative.) In a series of studies, Davis, Efstathiou, Frenk, & White (1985) showed that cold dark matter models explain beautifully a broad set of large-scale structure observations. Theoretically preferred cold dark matter candidates are either very heavy particles such as neutralinos with mass ~ 100 GeV, which are non-relativistic very early, or they are created essentially with zero-random velocity, as would be the case for axions with a mass of $\sim 10^{-5}$ eV.

In chapter 3 we summarise what *appear* to be problems with the CDM models and discuss the possible alternative models.

1.4 INFLATIONARY UNIVERSE AND THE DENSITY FLUCTUATION SPECTRUM

1.4.1 Primeval fluctuations in the inflationary universe

If the Universe were completely homogeneous on all scales, structures like galaxies, galaxy clusters, and voids would not have formed. In order for such rich structure to form via gravitational instability, the generation of density fluctuations is needed at some initial epoch. The mechanism for generating the primeval density fluctuations is not understood (as usual in cosmology), and is very difficult to probe directly from current observations. Among the competing theories, the most promising and broadly accepted scenario is the so-called “inflationary model” (Guth & Pi 1982; Starobinskii 1982; Hawking 1982; Bardeen, Steinhardt & Turner 1983). It involves a rapid expansion of the Universe at an early epoch for a brief period. The full description of the inflationary theory (if ever understood) would require more than a chapter, so in this section we focus on the main consequences of the inflationary scenario. A good review on inflation in the context of astronomy is given by Narlikar & Padmanabhan (1991).

The basic property common to most of the inflationary scenarios is that a scalar field ϕ , called the Higgs field, is governed by a potential $V(\phi)$ and the energy density of the vacuum state of the scalar field $\rho_v \simeq V(\phi)$ contributes dominantly. For a nearly flat, slowly changing potential, $\rho_v \simeq V(\phi) \simeq \text{constant}$, and the scalar field acts like a cosmological constant in the Friedmann equation:

$$\left(\frac{\dot{a}}{a}\right)^2 \simeq \frac{8\pi G}{3} V(\phi). \quad (1.37)$$

The equation has the de-Sitter universe solution

$$a \propto \exp\left(\frac{t}{\tau}\right), \quad (1.38)$$

with

$$\tau \simeq \left[\frac{3}{8\pi G V(\phi)} \right]^{1/2}. \quad (1.39)$$

During this phase, for a time τ of order 10^{-34} seconds, the universe expands exponentially. At the last stage of the rapid expansion when the field settles

to equilibrium, it oscillates around the minimum, which causes particle production known as “reheating”. Quantum fluctuations in ϕ in this phase give rise to the density fluctuations which have random phases –hence are Gaussian. Inflation thus naturally gives an explanation for the generation of density fluctuations.

In addition to generating fluctuations, inflation also solves other cosmological puzzles such as the flatness of the universe and the absence of monopoles, which are indeed the observed properties of the Universe.

Let us discuss the actual *shape* of the spectrum of the density perturbations generated by inflation. In describing the galaxy formation process, one usually just *postulates* a spectrum of initial density fluctuation. Conventionally a power law

$$|\delta(k)|^2 \sim k^n \quad (1.40)$$

is assumed. In fact, inflation generically predicts a particular case $n = 1$. (To be more precise, the spectrum generated by inflation is close to the $n = 1$ case.) This spectrum, called the Harrison-Zel’dovich spectrum, has a special property; it gives fluctuations which enter the cosmological horizon with constant characteristic amplitude.

1.4.2 Transfer function

Physical processes that change the shape of the primordial fluctuation spectrum can be summarised in the transfer function, which includes effects such as the Jeans scale oscillations and radiation damping. The transfer function relates the primordial power spectrum to the actual, processed spectrum:

$$P(k) = T^2(k)P_i, \quad (1.41)$$

where P_i is the primordial spectrum. For CDM models, the following parametric form introduced by Bond & Efstathiou (1984) is commonly used:

$$P(k) = \frac{Ak}{(1 + [ak/\Gamma + (bk/\Gamma)^{3/2} + (ck/\Gamma)^2]^\nu)^{2/\nu}}, \quad (1.42)$$

where $a = 6.4h^{-1}\text{Mpc}$, $b = 3.0h^{-1}\text{Mpc}$, $c = 1.7h^{-1}\text{Mpc}$, and $\nu = 1.13$. The so-called shape parameter Γ characterise the typical *scale* of the spectrum, and the normalisation constant A is observationally determined either by using the CMB measurements or by relating it to the rms linear fluctuations in the mass

distribution on a scale of $8h^{-1}$ Mpc, σ_8 , defined by

$$\sigma_8^2 = \frac{1}{(2\pi)^3} \int P(k) \left(\frac{3}{kR_8} j_1(kR_8) \right)^2 d^3k, \quad (1.43)$$

where $R_8 = 8h^{-1}$ Mpc and j_1 is a spherical Bessel function. The overall amplitude of the power spectrum can be fixed by matching the abundance of rich clusters to the observed abundance. This matching can be carried out using the masses of rich clusters (White et al. 1993) or their X-ray temperatures (Eke, Cole & Frenk 1996, Viana & Liddle 1996).

1.5 HYDRODYNAMICS AND DISSIPATION

So far we have not dealt with gas pressure of the intergalactic medium (IGM). This may be a good approximation when gravity is the dominant force. However, in the late non-linear phase of structure formation, hydrodynamical and radiative effects become important.

In this section, we describe the relevant physical processes with a particular attention to the implementations in the currently popular semi-analytic modelling of galaxy formation and in Smoothed Particle Hydrodynamics.

1.5.1 Smoothed Particle Hydrodynamics

The basic fluid equations are the continuity equation

$$\frac{d\rho}{dt} + \rho \nabla \cdot \mathbf{v} = 0, \quad (1.44)$$

the Euler equation

$$\frac{d\mathbf{v}}{dt} = -\frac{\nabla P}{\rho} - \nabla\Phi, \quad (1.45)$$

and the energy equation

$$\frac{du}{dt} = -\frac{P}{\rho} \nabla \cdot \mathbf{v} + \frac{\Gamma - \Lambda}{\rho}. \quad (1.46)$$

In the above equations P is the gas pressure, u is the specific energy per unit mass, and Γ and Λ are the heating and cooling terms.

In Smoothed Particle Hydrodynamics (SPH) the above equations are solved numerically by employing an ensemble of, say N , particles. A smoothed estimate of the density at position \mathbf{r} is computed by

$$\langle \rho(\mathbf{r}) \rangle = \int d^3r' \rho(\mathbf{r}') W(\mathbf{r} - \mathbf{r}', h) \approx \sum m W(\mathbf{r} - \mathbf{r}'_i, h), \quad (1.47)$$

where $W(\mathbf{r}, h)$ is the so-called smoothing kernel, a function peaked around $|\mathbf{r}| = 0$, and h is the associated smoothing length. With density ρ defined in this manner, an arbitrary physical quantity $A(\mathbf{r})$ can be estimated similarly

$$\langle A(\mathbf{r}) \rangle = \int d^3r' A(\mathbf{r}') W(\mathbf{r} - \mathbf{r}', h) \approx \sum m \frac{A(\mathbf{r}_i)}{\rho(\mathbf{r}'_i)} W(\mathbf{r} - \mathbf{r}'_i, h). \quad (1.48)$$

The smoothed estimate of the time derivative of A is obtained by exchanging the order of the volume integral and differentiation in time:

$$\frac{d}{dt} \langle A(\mathbf{r}) \rangle = \left\langle \frac{dA(\mathbf{r})}{dt} \right\rangle. \quad (1.49)$$

Spatial derivatives are greatly simplified in SPH. Using integration by parts, spatial derivatives can be translated into spatial derivatives of the *kernel*, i.e.,

$$\nabla \langle A(\mathbf{r}) \rangle = \langle \nabla A(\mathbf{r}) \rangle \approx \sum m \frac{A(\mathbf{r}_i)}{\rho(\mathbf{r}'_i)} \nabla W(\mathbf{r} - \mathbf{r}'_i, h). \quad (1.50)$$

As for the exact shape of the kernel $W(\mathbf{r}, h)$, various types are suggested (see e.g., Monaghan 1985; Benz 1990). The spline kernel is commonly adopted in current SPH codes.

Once we obtain the smoothed estimates of physical quantities and their derivatives, it is straightforward (but not unique) to solve the hydrodynamic equations. In the GADGET code (Springel, Yoshida & White 2001) which we use for the SPH simulations in this thesis, the implementation follows that of Hernquist & Katz (1990). The equation of motion is given by

$$\frac{dv_i}{dt} = - \sum_j m \left(\frac{P_i}{\rho_i^2} + \frac{P_j}{\rho_j^2} + \Pi_{ij} \right) \nabla_i W(\mathbf{r}_{ij}, h_i) - \nabla_i \Phi(\mathbf{r}_i), \quad (1.51)$$

and the energy equation can be written as

$$\frac{du_i}{dt} = \frac{1}{2} \sum_j m \left(\frac{P_i}{\rho_i^2} + \frac{P_j}{\rho_j^2} + \Pi_{ij} \right) (\mathbf{v}_i - \mathbf{v}_j) \left[\frac{1}{2} \nabla_i W(\mathbf{r}_{ij}, h_i) + \frac{1}{2} \nabla_j W(\mathbf{r}_{ij}, h_j) \right], \quad (1.52)$$

where Π_{ij} is the artificial viscosity tensor. Further details of the implementations are found in Springel et al. (2001a).

In chapter 3, we study the formation of galaxy cluster for a cosmological model in which cold dark matter particles interact strongly with each other. In such systems, dark matter behaves as a “fluid” and causes an effective “pressure”. We study the simplest case where the dark matter is an ideal fluid, and we model the fluid by the Smoothed Particle Hydrodynamics.

1.5.2 Cooling

Consider a simple model of a galaxy as a spherical gas cloud. Gravitational instability drives it to collapse, and then it is expected to be in an equilibrium state and have a temperature $k_B T \approx GM\mu m_p/R$, where k_B is the Boltzmann constant, μ is the mean molecular weight, m_p is the proton mass, and R is the virial radius. If this temperature is high enough ($T \gg 10^4\text{K}$), radiation due to the bremsstrahlung process becomes important, and the gas starts to *cool*. In this situation, the balance between pressure support and gravity determines the size of the object and it depends on two characteristic time scales: the cooling time

$$t_{\text{cool}} = -\frac{E}{\dot{E}} \approx \frac{3}{2} \frac{\rho k_B T}{\mu m_p n_e^2 \Lambda(T)}, \quad (1.53)$$

and the dynamical time

$$t_{\text{dyn}} = \left(\frac{R^3}{GM} \right)^{1/2}, \quad (1.54)$$

which is defined to be the free-fall collapse time for a sphere of mass M and radius R . In equation (1.53), n_e is the electron number density and $\Lambda(T)$ is the cooling rate. In the context of galaxy formation, the main contributions to cooling are free-free (bremsstrahlung) radiation, recombination radiation from hydrogen and helium, and Compton cooling via the CMB photons.

1.5.3 Star formation and feedback

Ideally models of galaxy formation should include star formation and the subsequent energy release from supernovae as well as gasdynamics. Unfortunately,

the physics describing these two processes is complicated and the detailed mechanisms are not yet well understood. It is well known that supernova explosions in galaxies give energy back to the surrounding gas in some way, perhaps both in thermal and mechanical forms. However, the detailed physical mechanism of the process, usually referred to as *feedback*, is poorly understood. Even if we knew how to treat these processes, the resolution achieved in modern numerical simulations is still much too poor to directly solve the problem. Hence we must resort to heuristic solutions, based on *ad hoc* phenomenological models of the relevant local physics.

In chapter 5 of this thesis, we study gas cooling associated with galaxy formation. Gas cooling in this context is a relatively well understood process. We compare the evolution of cooling gas in two different models, the Smoothed Particle Hydrodynamics simulations and the semi-analytic galaxy formation model.

1.6 CLUSTERING OF GALAXIES AND BIAS

1.6.1 Correlation functions and the power spectra

In this section we discuss the statistical properties of spatial density fluctuations. The lowest order statistics which are commonly used in cosmology are the correlation functions and power spectra. Let us define the spatial correlation function in terms of the density field $\rho(\mathbf{x})$:

$$\xi(r) = \frac{\langle [\rho(\mathbf{x}) - \bar{\rho}][\rho(\mathbf{x} + \mathbf{r}) - \bar{\rho}] \rangle}{\bar{\rho}^2} = \langle \delta(\mathbf{x})\delta(\mathbf{x} + \mathbf{r}) \rangle, \quad (1.55)$$

where the mean is taken over all points \mathbf{x} in a representative volume V of the region considered. Because of our assumption of statistical homogeneity and isotropy, ξ depends only on the modulus of the vector \mathbf{r} , and not on its direction. The Fourier decomposition of the density field is

$$\delta(\mathbf{x}) = \sum_{\mathbf{k}} \delta(\mathbf{k}) \exp(i\mathbf{k} \cdot \mathbf{x}), \quad (1.56)$$

where the Fourier coefficients $\delta(\mathbf{k})$ are complex quantities given by

$$\delta(\mathbf{k}) = \frac{1}{V} \int_V \delta(\mathbf{x}) \exp(-i\mathbf{k} \cdot \mathbf{x}) d\mathbf{x}. \quad (1.57)$$

Now we expand the last expression in equation (1.55) via the Fourier decomposition (1.57)

$$\xi(\mathbf{r}) = \frac{1}{V} \int_V \sum_{\mathbf{k}} \delta_{\mathbf{k}} \exp(i\mathbf{k} \cdot \mathbf{x}) \sum_{\mathbf{k}'} \delta_{\mathbf{k}'}^* \exp(-i\mathbf{k}' \cdot (\mathbf{x} + \mathbf{r})) d\mathbf{x} = \sum_{\mathbf{k}} \langle |\delta_{\mathbf{k}}|^2 \rangle \exp(-i\mathbf{k} \cdot \mathbf{r}). \quad (1.58)$$

In the limit $V \rightarrow \infty$, this becomes

$$\xi(\mathbf{r}) = \frac{1}{(2\pi)^3} \int P(k) \exp(-i\mathbf{k} \cdot \mathbf{r}) d\mathbf{k}. \quad (1.59)$$

The above equation manifests that the power spectrum is just the Fourier transform of the correlation function – the Wiener-Khintchine theorem.

Totsuji & Kihara (1969) applied the two-point correlation function, which had been originally used in statistical mechanics, to the distribution of galaxies.

The observed two-point correlation function of galaxies is well described by

$$\xi(r) \approx \left(\frac{r}{5 \text{ Mpc}/h} \right)^{-1.8} \quad (1.60)$$

for $0.1h^{-1}\text{Mpc} \leq r \leq 30h^{-1}\text{Mpc}$.

1.6.2 Biased galaxy formation

We have discussed the correlation function of the *mass* density field. If galaxies trace the mass, the two-point correlation function of galaxies, $\xi_{\text{gg}}(r)$, coincides with $\xi(r)$. This is probably not a good representation of reality, however. Since galaxy formation involves complex gas dynamical and dissipative processes such as collapse, cooling and condensation, it is more natural to think that suitable sites for galaxy formation are peaks of the underlying initial mass density field where matter will collapse at later times. In this case, the galaxy correlation function will be no longer equivalent to the mass correlation function. It is indeed well known that the standard CDM model has some troubles unless we allow “biasing” (Davis et al. 1985). The problem can be well described by an example of numerical simulations. If one runs a N -body simulation for a SCDM model to the epoch when the *slope* of the mass correlation function matches to that of the observed galaxies, then the velocities are too high compared to the observed peculiar velocities of galaxies. One obvious resolution is to have a lower value of Ω , though it contradicts the prediction of inflation, and another way which we discuss here is to involve biasing.

Biasing is quantitatively defined by introducing a bias parameter b such that

$$\xi_{\text{gg}}(r) = b^2 \xi(r). \quad (1.61)$$

Alternatively, a more commonly used measure for b in cosmology is

$$b^2 = \frac{\sigma_8^2(\text{galaxies})}{\sigma_8^2(\text{mass})}, \quad (1.62)$$

where σ_8^2 is the mass (or galaxy count) variance in spheres of radius $8h^{-1}\text{Mpc}$ defined in equation (1.43). Observationally $\sigma_8(\text{galaxy})$ is measured to be of order unity (e.g. Maddox et al. 1996). Note that equation (1.62) follows from equation (1.61) if the bias factor is constant. It is the simplest, and indeed too idealised case. Generally the full description of bias will be non-linear and stochastic (Dekel & Lahav 1999). In chapter 2 we present a more detailed and quantitative study of biasing.

1.7 COSMIC MICROWAVE BACKGROUND RADIATION

1.7.1 The 3-K radiation

The cosmic microwave background radiation (CMB) was predicted by George Gamow (1948) as a direct relic of the hot early universe in a Big Bang theory. About 20 years later Penzias & Wilson (1965) discovered such radiation at about 3 K coming from all directions in the sky. Various experiments since then have confirmed that the radiation spectrum follows a (almost) perfect Planckian distribution at around 2.73 K. The discovery of *anisotropies* in the temperature of the cosmic microwave background radiation (CMB) by the *COBE* satellite in 1992 (Smoot et al. 1992) revolutionised cosmology and has transformed the field from a theoretical exercise to an active experimental area of research. Recent measurements of the CMB anisotropies by the Boomerang (de Bernardis et al. 2000; Netterfield et al. 2001) and the MAXIMA (Hanany et al. 2000; Lee et al. 2001) experiments have made it possible to determine the angular power spectrum of the temperature fluctuations from degree to arcminute scales. These results place a strong constraint on the fundamental cosmological parameters.

1.7.2 Anisotropy mechanisms

The *COBE* satellite discovered that the microwave background radiation is nearly isotropic, but not *perfectly* isotropic. Various physical processes cause the CMB anisotropies and each of them has its characteristic signature – fluctuation amplitude and angular dependence. First we introduce some mathematical tools to quantify the level of anisotropies. Let us define the fractional deviation in a direction ϕ in the sky of the measured (at a certain wavelength) temperature $T(\phi)$ from the global mean T :

$$\frac{\Delta T}{T}(\phi) = (T(\phi) - T)/T. \quad (1.63)$$

The angular correlation function is then defined as

$$C(\theta) = \left\langle \frac{\Delta T}{T}(\phi) \frac{\Delta T}{T}(\phi') \right\rangle_{|\theta=|\phi-\phi'|} \quad (1.64)$$

for two different points in the sky with separation θ .

An angular decomposition is useful and often used when one thinks about a specific fluctuation on an angular scale. The correlation function $C(\theta)$ can be decomposed into Legendre polynomials

$$C(\theta) = \frac{1}{4\pi} \sum_l (2l + 1) C_l P_l(\cos(\theta)). \quad (1.65)$$

The first term to be considered is the dipole term $l = 1$. We know that the Earth orbits around the sun and the sun moves relative to the Galactic centre, and so on. Let us now think about the Earth’s motion relative to the ‘rest’ frame of the CMB. If the Earth is moving at velocity v , a frequency shift $\Delta\nu/\nu$ of the CMB photons will appear as a temperature fluctuation of dipole shape. Such a dipole anisotropy is indeed observed by *COBE* satellite and it was found that the Earth is moving relative to the CMB rest frame at about 550 km s^{-1} (Kogut et al. 1993).

The next large angular scale anisotropies are caused by structure formation and by large-scale fluctuations in gravitational potential; the Sachs-Wolfe effect (Sachs & Wolfe 1967). The *COBE* satellite discovered that, at the last scattering epoch, the Universe was *almost* homogeneous; the density fluctuations at $z = 1000$ are inferred to be of the order 10^{-5} .

There are two important physical mechanisms which cause *secondary* CMB anisotropies: the Sunyaev-Zel’dovich effect and reionisation. The Sunyaev-Zel’dovich effect is caused by spatially restricted Comptonisation. Hot gas clumps such as the intracluster gas in rich clusters have X-ray temperatures above 10 keV. The CMB photons scatter off the hot electrons, causing the CMB spectrum distortion via the net gain of energy from the electrons. The amplitude of the Sunyaev-Zel’dovich effect is as high as 10^{-3} in $\Delta T/T$, being a dominant source of the secondary anisotropies on arcminutes scales. In chapter 4 we show how the secondary anisotropies due to the Sunyaev-Zel’dovich effect appear in the CMB temperature fluctuation maps.

Possible reionisation of the intergalactic medium after the recombination epoch will lead to a significant secondary anisotropy. Early star formation, active galactic nuclei or quasars could, in principle, have caused the reionisation, and it is likely to have happened in a *patchy* pattern. From the Gunn-Peterson test, we know that something reionised the Universe sometime before $z \approx 5$ but the detailed picture remains unclear. The ionisation mechanism is usually thought to be photo-ionisation by the UV radiation emitted by quasars or stars, but collisional ionisation with electrons heated up by supernovae driven winds from early ‘POP III’ objects might have contributed to some degree.

1.8 OUTLINE

The rest of the thesis is organised as follows. In chapter 2, I address a long standing problem; in a deep pencil-beam survey by Broadhurst and collaborators galaxies were observed to be regularly spaced with a period of $128h^{-1}\text{Mpc}$. By creating a large number of mock redshift survey, we estimate an *a priori* probability that such a regular pattern should be found in a Cold Dark Matter model universe. The contents are based on the article:

Yoshida, N., Colberg, J., White, S. D. M., Evrard, A. E., MacFarland, T. J., Couchman, H. M. P., Jenkins, A., Frenk, C. S., Pearce, F. R., Efstathiou, G., Peacock, J. A., Thomas, P. A. (The Virgo Consortium), *Simulations of deep pencil-beam redshift surveys*, MNRAS, 325, 803 (2001)

Chapter 3 is devoted to a study of dark matter self-interaction. We briefly review possible problems in the standard CDM models and introduce an alternative model. Then we study cluster formation in the context of this newly proposed model by carrying out large numerical simulations. The contents are based on the articles:

Yoshida, N., Springel, V., White, S. D. M, & Tormen, G., *Collisional dark matter and the structure of dark halos*, ApJ, 535, L103 (2000a)

Yoshida, N., Springel, V., White, S. D. M, & Tormen, G., *Weakly self-interacting dark matter and the structure of dark halos*, ApJ, 544, L87 (2000b)

In chapter 4, we study the statistics of CMB temperature fluctuations due to the Sunyaev-Zel'dovich effect. We develop an analytic model to predict the distribution of the thermal and kinematic SZ temperature fluctuations. We test the model against numerical simulations. We also discuss non-Gaussianity in CMB temperature fluctuations and the detectability of such signals. The contents are based on the article:

Yoshida, N., Sheth, R. K., & Diaferio, A., *Non-Gaussian CMB temperature fluctuations from peculiar velocities of clusters*, MNRAS, 328, 669 (2001)

Chapter 5 contains a study of gas cooling and the formation of galaxies. We study the hydrodynamic and radiative processes associated with galaxy formation. We compare results from a semi-analytic galaxy formation model with the outputs of hydrodynamic simulations. The contents are based on the article:

Yoshida, N., Stöhr, F., Springel, V., & White, S. D. M., *Gas cooling in simulations of the galaxy population*, submitted to MNRAS

Finally in chapter 6, I will give a summary of the results in this thesis and prospects for the future work.

CHAPTER 2

**Statistics of galaxy clustering by
pencil-beam surveys**

2.1 INTRODUCTION

The redshift distribution of galaxies in the pencil-beam survey of Broadhurst et al. (1990, hereafter BEKS) displayed a striking periodicity on a scale of $128h^{-1}\text{Mpc}$. This result has attracted a good deal of interest over the subsequent decade, and the significance and nature of periodicity or regularity in the distribution of galaxies has remained the subject of a stimulating debate in both observational and theoretical cosmology. Although a number of studies have been devoted to the BEKS pencil-beam survey and other similar surveys, several fundamental questions remain unanswered.

From the theoretical viewpoint, it is important to decide whether such apparently periodic galaxy distributions can occur with reasonable probability in a Cold Dark Matter universe, or require physics beyond the standard paradigm. Performing large simulations can directly address this question. The first simulation specifically designed for pencil-beam comparisons was that of Park and Gott (1991, hereafter PG). Their rod-shaped CDM simulation allowed them to create twelve quasi-independent mock pencil-beam surveys similar in length to that of BEKS. One of their samples appeared ‘more periodic’ than the BEKS data according to the particular statistical test they used for comparison. Other authors (Kurki-Suonio et al.; Pierre 1990; Coles 1990; van de Weygaert 1991; SubbaRao & Szalay 1992) have used purely geometrical models such as cubic lattices and Voronoi foams to explore the implications of apparent regularities similar to those found by BEKS. In particular, SubbaRao and Szalay (1992) presented a sequence of Monte Carlo simulations of surveys of Voronoi foams, showing that such a model can successfully reproduce the data as judged by a variety of statistical measures, for example, the heights, positions and signal-to-noise ratios of the highest peaks in the power spectra. Kaiser & Peacock (1991) argued that the highest such peaks in the BEKS data are not sufficiently significant to be unexpected in a CDM universe, but did not support this conclusion with detailed simulations. Dekel et al. (1992) introduced other statistics, more similar to those of PG, and again concluded that the apparent periodicity seen in the real data is not particularly unlikely in any of the toy models they used for comparison. Their models include Gaussian models with an extreme initial power spectrum with power only on scales $\sim 100h^{-1}\text{Mpc}$. They found regular ‘galaxy’ distributions a few per cent of the time and concluded that the BEKS data do *not* rule out all Gaussian

models. However, these theoretical studies did not give any clear answer to the question posed above: is the BEKS regularity compatible with the standard CDM paradigm? We attempt to answer this below using versions of all the statistical tools developed in earlier papers.

There have been several interesting observational developments after BEKS. Willmer et al. (1994) found that, if the original BEKS deep survey at the North Galactic Pole had been carried out 1 degree or more to the west, many of the peaks would have been missed. On the other hand, Koo et al. (1993) added new data from a wider survey to the original BEKS data and found the highest peak in the power spectrum to be further enhanced. They also analysed another set of deep pencil-beam surveys and found a peak of weaker significance on the *same* scale, $128 h^{-1}\text{Mpc}$. This raises another question: is $128 h^{-1}\text{Mpc}$ a preferred length scale for the galaxy distribution? Further support for such a preferred scale has been presented by Tully et al. (1992), Ettori et al. (1997) and Einasto et al. (1997). Thus one can wonder whether a single scale could be indicated with such apparent consistency within the CDM paradigm.

With the important exception of the work of PG there has been surprisingly little comparison of the BEKS data with direct simulations of standard CDM cosmogonies. Even before the BEKS discovery, White et al. (1987) had shown that pencil-beams drilled through periodic replications of their CDM simulations frequently showed a kind of ‘picket fence’ regularity in their redshift distribution. Frenk (1991) confirmed this result and concluded that regular patterns similar to that seen in the BEKS data are easy to find in their simulations. However, it is clearly dangerous to make use of periodic replications of a simulation when assessing the significance of apparent periodicities in the redshift distribution. It is preferable to simulate a volume large enough to encompass the whole survey. Furthermore, since many independent artificial surveys are needed to establish that the real data are highly unlikely in the cosmogony simulated, the simulated volume must be fully three-dimensional (unlike that of PG) to allow the creation of many quasi-independent lines-of-sight. A final consideration is that the BEKS data reach to redshifts beyond 0.3, so that evolution of clustering along the survey may not be negligible.

In this chapter we investigate the distribution of ‘galaxies’ along the past light-cones of hypothetical observers. Particle positions and velocities on these light-cones were generated as output from the Hubble Volume Simulations (Evrard et al. 2000). These very large CDM N -body simulations were recently performed by the Virgo consortium and each used 10^9 particles to follow the evolution of the matter distribution within cubic regions of an $\Omega = 1 \tau\text{CDM}$ ($\Omega = 0.3 \Lambda\text{CDM}$) universe of side $2000 h^{-1}\text{Mpc}$ ($3000 h^{-1}\text{Mpc}$). Such large

volumes allow many independent light-cones to be generated out to $z \sim 1$. The light-cone output automatically accounts for clustering evolution with redshift. The principal uncertainty lies in how to create a ‘galaxy’ distribution from the simulated mass distribution. We employ Lagrangian bias schemes similar to those of White et al. (1987) and Cole et al. (1998). Individual particles are tagged as galaxies with a probability which depends only on the smoothed *initial* overdensity field in their neighbourhood. The parameters of these schemes are adjusted so that the present-day correlations of the simulated galaxies match observation. Many quasi-independent mock pencil-beam surveys can then be created adopting the geometry and the galaxy selection probability with distance of the BEKS surveys.

Our discussions focus primarily on the significance of the BEKS data in comparison with our CDM samples. We begin by following the methods used originally by BEKS, namely, redshift counts, pair separation distributions, and the one-dimensional power spectrum. Redshift counts are translated into a distribution in physical distance assuming the same cosmological parameters as BEKS. For the one-dimensional power spectra, the height of the highest peak is the most important statistic. Szalay et al. (1991) show that the statistical significance of the highest peak of the BEKS data is at 10^{-4} level, based on the formal probability for the peak height. This calculation was disputed by Kaiser & Peacock (1991) because of the difficulty in estimating the appropriate noise level. We calculate relative peak-to-noise ratios of the highest peaks in the power spectra in identical ways for real and simulated data and so can compare the two without needing to resolve this issue. We also apply two additional statistical tests for regularity, the Δ test of PG and a ‘supercluster’ statistic designed by Dekel et al. (1992).

2.2 N -BODY SIMULATION

The simulation data we use are the so-called “light-cone outputs” produced from the Hubble Volume simulations (details are in Evrard et al. 2001). The basic simulation parameters are tabulated in Table 2.1, where L_{box} is the box size in $h^{-1}\text{Mpc}$, Γ stands for the shape parameter of the initial power spectrum

Table 2.1 Parameters of the Hubble Volume Simulations

Model	L_{box}	Ω	Λ	h	σ_8	Γ	$m_p (M_\odot/h)$
τ CDM	2000.0	1.0	0.0	0.5	0.6	0.21	2.22×10^{12}
Λ CDM	3000.0	0.3	0.7	0.7	0.9	0.21	2.25×10^{12}

and m_p is the mass per particle; other notations are standard.

The light-cone outputs are created in the following way. We define an observer at a specific point in the simulation box at the final time. The position and velocity of each particle is recorded whenever it crosses the past light-cone of this observer, and these phase-space coordinates are accumulated in a single data file. The evolution of clustering with lookback time (distance from the observer) is automatically included in such data. As we require mock pencil-beam surveys which reach $z \sim 0.5$ (spanning $\sim 1000h^{-1}\text{Mpc}$ in physical scale), such light-cone output is both realistic and desirable. We use stored data from two different light-cone outputs for each cosmology. Each covers one octant of a sphere, and they emanate in opposite directions from the same point. Figure 2.1 illustrates this geometry. In each case we use data out to a comoving distance of $1500h^{-1}\text{Mpc}$, corresponding to redshift 0.77 in the τ CDM model and 0.58 in the Λ CDM model. For the τ CDM case the total length covered is larger than the side of the simulation box, but this has a negligible effect on the mock BEKS surveys we construct.

2.3 GALAXY SELECTION

To create realistic mock surveys we have to select particles as galaxies with the same distribution in depth as the real data and with an appropriately ‘biased’ distribution relative to the dark matter. We do this in two stages.

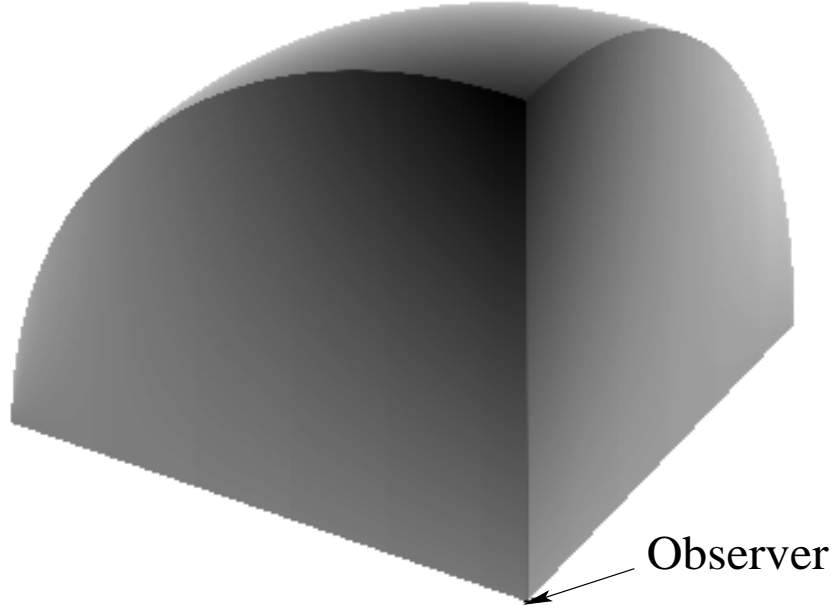


Figure 2.1 The shape of a light-cone and the observer point. The radius of the sphere is $1500 h^{-1}$ in both the τ CDM and the Λ CDM models.

First we identify a biased subset of the particles chosen according to the value of the smoothed linear mass overdensity at their position at high redshift. The parameters defining this identification are chosen so that the two-point correlation function of the identified ‘galaxies’ at $z = 0$ matches the observed correlation function of low redshift galaxies. For the τ CDM model, we are able to achieve this while retaining about two-thirds of the simulation particles as ‘galaxies’. The resulting comoving ‘galaxy’ number density is $0.08 h^3 \text{Mpc}^{-3}$. For the Λ CDM model we get a number density of ‘galaxies’ in the range 0.02 to $0.033 h^3 \text{Mpc}^{-3}$ depending on the bias scheme. This lower number density is due to the low number density of the dark-matter particles in this model. The second stage is to mimic the effect of the apparent magnitude limits of the real galaxy surveys by including ‘galaxy’ particles into the final mock catalogues with a probability which depends on distance from the observer. Since this stage is independent of the first, we are effectively assuming that the clustering of galaxies is independent of their luminosity. Our radial selection function is based on those directly estimated for the BEKS surveys.

2.3.1 Lagrangian Bias

Cole et al. (1998) developed and tested a set of bias schemes to extract ‘galaxies’ from N -body simulations. The procedure we use for the first stage of our galaxy selection is similar to their Model 1, but has a different functional form for the probability function. Since we need a bias factor greater than unity for the τ CDM model and less than unity for the Λ CDM model (a result of the differing mass correlations in the two cases) ‘galaxies’ need to avoid regions of low initial density in the τ CDM simulation and to avoid regions of high initial density in the Λ CDM simulation. We begin by smoothing the density field at an early time with a Gaussian, $\exp(-r^2/2r_o^2)$ with $r_o = 3h^{-1}\text{Mpc}$ and assigning the corresponding overdensity δ to each dark-matter particle. Then a normalised overdensity $\nu = \delta/\sigma_s$ is computed, where σ_s is the root mean square value of particle δ -values. Finally, we define a probability function $P(\nu)$ which determines whether a particle is tagged as a ‘galaxy’. We random-sample dark-matter particles for tagging as galaxies based on this probability. Once tagged as a galaxy in this way, particles remain tagged throughout the simulation, and so become potentially visible in our mock surveys whenever their world-line crosses a light-cone. For all the bias models described below the ‘galaxy-galaxy’ correlation function was calculated in real space within a cubic box of side $200 h^{-1}\text{Mpc}$ with the observer at one corner. These correlation functions are shown in Figure 2.2.

τ CDM model bias t1: For the τ CDM model, we chose a simple power law form $P(\nu) \propto (\nu - \nu_c)^{0.2}$ for the probability function. We impose a threshold at $\nu = \nu_c = -0.55$ below which the probability is set to be zero. This suppresses the formation of ‘galaxies’ in voids. These parameters were determined by matching the present-day two-point correlation function of the ‘galaxies’ to the observational result for the APM survey (Baugh 1996, see Figure 2.2) on length scales from $0.2 h^{-1}\text{Mpc}$ to $20h^{-1}\text{Mpc}$. We note here that in our N -body simulations the gravitational softening length is $0.1h^{-1}\text{Mpc}$.

Λ CDM bias model L1: For the Λ CDM model, we must ‘anti-bias’ because the predicted mass correlations on small scales are substantially larger than observed galaxy correlations (see, for example, Jenkins et al. 1998). We set a sharp *upper* cut-off at $\nu_c = 1.34$, above which $P(\nu)$ is zero. All particles below this threshold are equally likely to be ‘galaxies’ ($P = \text{const}$). Although this may seem unphysical, more realistic modelling of galaxy formation in Λ CDM models does indeed produce the anti-bias required for consistency with observation, albeit through a more complex interplay of statistical factors (Kauffmann et al. 1999; Benson et al. 2000). We use a simpler scheme in or-

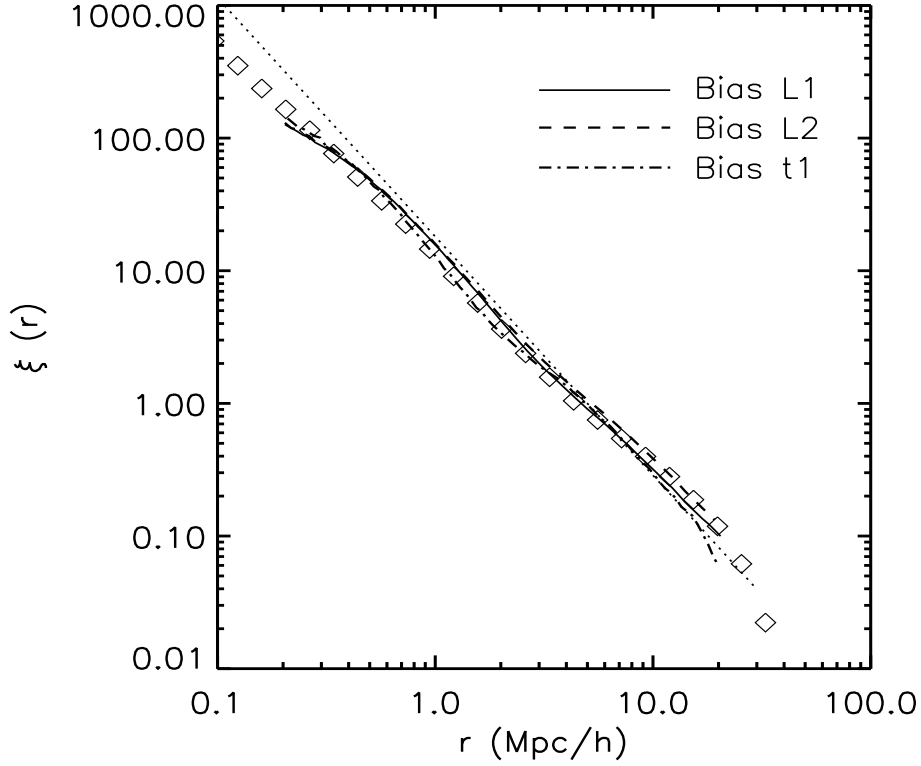


Figure 2.2 The two-point correlation functions of the biased ‘galaxies’. The dash-dotted line is the ‘galaxy-galaxy’ correlation of our model bias **t1** and the solid line is for bias **L1**, the dashed line for bias **L2**. The open squares are the observational data from the APM survey (Baugh 1996) and the dotted line is the assumed galaxy correlation function in Szalay et al. (1991) for the analysis of the BEKS survey. The curves fit well both the APM data and the Szalay et al. model.

der to produce the desired two-point correlation function; on scales of interest here, only a small anti-bias is necessary.

Λ CDM bias model L2 : For comparison purposes, we applied a second bias model to the Λ CDM simulation. We set an additional *lower* threshold at $\nu_{low} = -0.7$ below which we again set $P = 0$. Thus the probability takes a non-zero (and constant) value only in the range $\nu_{low} \leq \nu \leq \nu_{high}$, where now $\nu_{high} = 0.9$. This model fits the observed correlations of galaxies just as well as **L1** but enhances the emptiness of voids

Figure 2.3 illustrates bias effects by comparing the distribution of dark-matter particles and of ‘galaxies’ in a thin slice through part of the simulation box at $z = 0$. For model **L1** the effect is difficult to detect visually, whereas the effect of the lower cut-off in model **L2** is obvious. Similarly, for the τ CDM model, underdense regions (voids) are clearly accentuated in the ‘galaxy’ distribution relative to the dark matter distribution. Cole et al. (1998) show similar plots to demonstrate how strong bias in high density model universes maps underdense regions in the mass distribution onto voids in the galaxy distribution. Such contrasted voids are generally seen in strongly biased models regardless of the functional form of $P(\nu)$.

We can quantitatively study the bias in our models by measuring the non-linear biasing parameters introduced by Dekel & Lahav (1999) (see also Sigad et al. 2000; Somerville et al. 2000). We compute the slope \hat{b} and nonlinearity \tilde{b} following the procedure described in Somerville et al. (2000). Figure 2.4 show the biasing relation between the ‘galaxy’ density field δ_g and the dark matter density field δ_d , smoothed with a $8h^{-1}$ Mpc scale top-hat filter. For each of our bias models, the mean biasing function $b(\delta_d)$, and its moments

$$\hat{b} = \frac{\langle b(\delta_d)\delta_d^2 \rangle}{\sigma^2}, \quad \tilde{b}^2 = \frac{\langle b^2(\delta_d)\delta_d^2 \rangle}{\sigma^2}, \quad (2.1)$$

are given in Figure 2.4. In the above expression we have used $\sigma^2 = \langle \delta_d^2 \rangle$ for the standard deviation. Strong biasing in **t1** and anti-biasing (for $1 + \delta_d > 0$) in **L1** and **L2** are clearly seen, and reflected in the values for the effective *slope*; $\hat{b} = 1.44$ for **t1**, 0.84 for **L1** and 0.90 for **L2**.

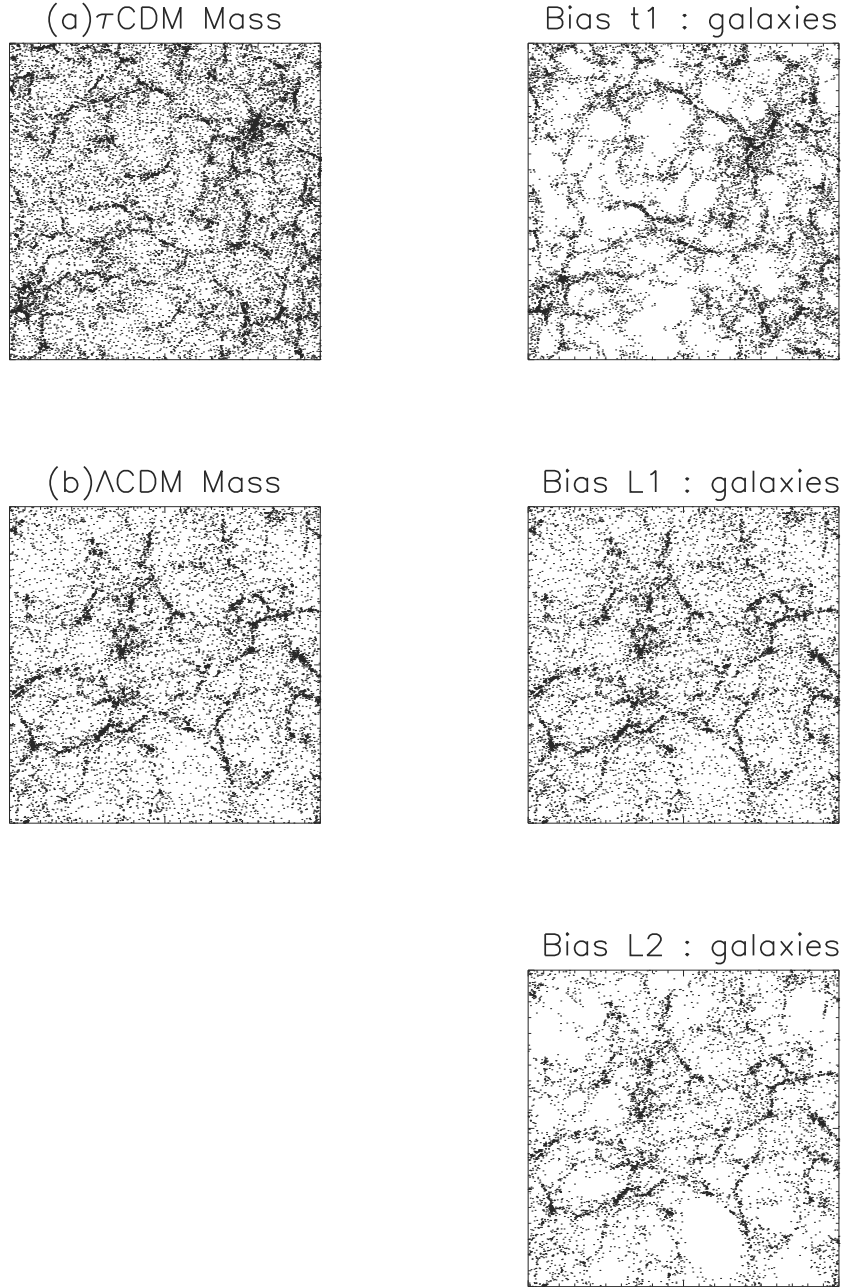


Figure 2.3 The distribution of the simulation dark-matter particles (left panels) and the biased 'galaxies' (right panels) in real space. The panels show $200 \times 200 \times 10 h^{-3} \text{Mpc}^3$ slabs. Note the difference in the number density of the simulation dark-matter particles between the τ CDM model ($0.125h^3\text{Mpc}^{-3}$) and the Λ CDM model ($0.037h^3\text{Mpc}^{-3}$). Strong-bias effects are apparent in **t1** and **L2** whereas in **L1** essentially no bias is seen.

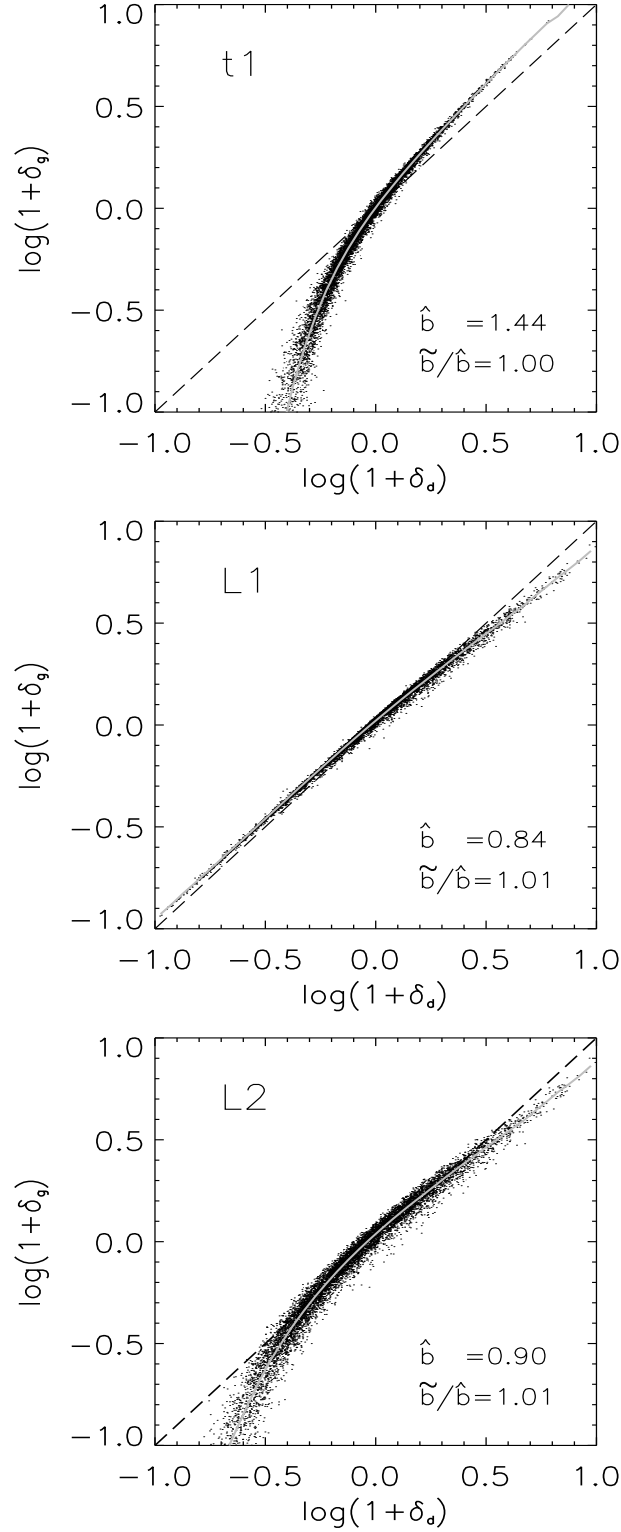


Figure 2.4 The joint distribution of the overdensity fields of ‘galaxies’ and mass, smoothed with a $8h^{-1}\text{Mpc}$ tophat window. The grey lines show the mean biasing function $b(\delta)$. Dashed lines show a linear relation $\delta_g = \delta_d$ for a reference. The measured biasing parameters \hat{b} and \tilde{b}/\hat{b} are given in each panels.

2.4 SURVEY STRATEGY

2.4.1 Geometry

We construct artificial surveys with a geometry very similar to that of the data analysed by BEKS. This consists of four surveys – a deep and a shallow survey near each Galactic Pole. The northern deep survey lies within a cone of 40-arcmin diameter about the pole and is made up of a set of roughly circular patches each 5-arcmin in diameter. About 10 small patches were surveyed but not all were completed by the time of writing so that the exact number of patches used in BEKS is unclear. For our artificial surveys we choose 9 circular patches within the 40-arcmin diameter cone, each of diameter 5 arcminutes. We place these irregularly and ensure no overlaps between them. For model **L2** the number density of ‘galaxies’ is too small to match the observations, so we increased the diameter of our patches to 7-arcmin. Although this widening results in a slight increase in the effective survey volume, the small patches still lie well within the larger cone of 40-arcmin diameter. The volume increase is compensated in the radial selection we describe below, so that the resulting ‘galaxy’ distribution is consistent with the desired distribution given in BEKS. For the deep-narrow pencil-beams, the transverse length scale is much smaller (the cone diameter is $\sim 4h^{-1}\text{Mpc}$ at $z=0.2$ where the radial selection function takes its maximum value) than the $100h^{-1}\text{Mpc}$ scale we address, so the increase in the patch width does not affect our results. In all cases the redshift counts in all patches were binned together to create a single deep survey. The northern shallow survey has a simpler geometry. A square area of about 14 square degrees is selected near the Galactic Pole, but with its centre offset by 7 degrees. The magnitude limit of the shallow survey is about 5 magnitudes brighter than that of the deep survey. Towards the South Galactic Pole both surveys are centred very close to the pole itself. The deep survey is confined within a cone of 20-arcmin diameter, while the shallow survey covers an area of 14 square degrees and has a magnitude limit about 4 magnitudes brighter.

When making an artificial survey we choose a random direction in the simulation as the Galactic polar axis and then define all areas on the artificial sky with reference to this direction. The light-cone outputs from our Hubble Volume simulations cover enough ‘sky’ to allow us to make well over 1000 near-independent artificial surveys.

2.4.2 Radial selection

‘Galaxies’ projected in our survey regions are assigned weights for selection depending on their distances. We use the estimated galaxy distributions given in Figure 1 of BEKS to define the relevant selection functions for each survey. The data are read off in redshift bins of width $\Delta z = 0.005$ for the deep surveys and $\Delta z = 0.001$ for the shallow surveys. We then derive a smoothed model galaxy distribution dN/dz for each survey and compute the corresponding comoving number densities from the number counts and the volume elements given by the survey geometry and the assumed cosmology. As explained above, we had to increase the size of the patches in the northern deep survey in case **L2** in order to get the correct mean counts. This is easily accounted for by appropriate renormalisation. These radial selection functions are used as sampling probabilities to determine whether a particular ‘galaxy’ is included in a catalogue or not. We normalise our probabilities by matching the mean number of ‘galaxies’ in each survey to the number of galaxies in BEKS data. This matching is done for the 4 surveys independently. For consistency, the normalisation coefficients obtained are then kept constant when constructing all realisations for a particular model.

2.4.3 Peculiar velocities

The peculiar velocities of ‘galaxies’ must be taken into account to create realistic mock redshift surveys. We simply assign our ‘galaxies’ the peculiar velocities of their corresponding dark-matter particles. Thus, while the spatial distribution of ‘galaxies’ is biased, there is no additional bias associated with their peculiar velocities. On small scales peculiar velocities lead to ‘finger-of-God’ effects which suppress power in the apparent spatial distribution at high wavenumber. In our mock catalogues the root mean square values of the ‘galaxy’ line-of-sight peculiar velocities are 342 km/sec in **t1**, 358 km/sec for **L1** and **L2**. The redshift bin width shown in BEKS is $\Delta z=0.005$ for the deep surveys, which translates ~ 1500 km/sec in recession velocity. Therefore, the assigned peculiar velocities of ‘galaxies’ do not smear out the *true* width of clumps in one-dimensional distributions, while they reflect properly the underlying velocity field. At the intermediate and small wavenumbers corresponding to the linear and quasi-linear regime, they increase the apparent power (e.g. Kaiser and Peacock 1991). These line-of-sight distortions reflect the enhanced contrast produced by infall onto superclusters. It is thus important to include the peculiar velocities when comparing simulations to the structures seen in the BEKS data.

2.5 GALAXY DISTRIBUTION AND POWER SPECTRUM ANALYSIS

The geometry of our light-cone datasets allows the axis of our artificial surveys to lie anywhere within one octant of the ‘sky’ (see Figure 2.1). We construct an ensemble of mock surveys with axes distributed uniformly across this octant in such a way that the areas covered by the corresponding deep surveys do not overlap. We end up with 1936 quasi-independent deep surveys for our τ CDM model. For the Λ CDM case an additional pair of light-cone outputs were stored, allowing us to construct 2625 disjoint deep surveys. To these deep pencil beams we add shallow surveys, whose volumes then have slight overlaps with those of neighbouring surveys. In practice, however, rather few ‘galaxies’ appear in more than one of our mock catalogues.

A series of plots of the redshift distribution and derived statistics are given for selected ‘mock BEKS surveys’ in Figure 2.6, which consists of 6 sets of 3 figures. These can be compared with Figure 2.5, which is actually for the real BEKS data, which we reproduce here for comparison with our simulation results. We read these data from Figure 2 in Szalay et al. (1991) where they are given as a histogram of bin width $10 h^{-1}\text{Mpc}$; when necessary for our analysis, we assume that the galaxies in each bin are uniformly distributed across the bin. The particular mock surveys in the following 6 plots were chosen to illustrate a variety of points made in the following sections.

2.5.1 One-dimensional distribution

In each set of plots in Figure 2.6, the top panel shows the distance histogram of ‘galaxies’ in the combined deep and shallow surveys. The total number of galaxies in these combined surveys is given in this panel. We have assumed an Einstein-de Sitter universe for both of our models when converting redshift to physical distance, although the actual value of Ω is 0.3 in the Λ CDM case. This apparent inconsistency is needed to allow a direct comparison with the analysis in BEKS where $\Omega = 1$ was also assumed. Szalay et al. (1991) noted that using low values of Ω to convert redshift to distance reduces the significance of the apparent periodicity in the BEKS data. Throughout this chapter we assume $\Omega = 1$ for this conversion.

In Figure 2.6, panel (a) shows one of the best catalogues in our **t1** ensemble

in that it gives the impression that ‘galaxies’ are distributed periodically and, in addition, the 1-D power spectrum shows a sharp and high peak. Panel (b) shows the same features but with a smaller characteristic spacing. In each of these plots we mark the best periodic representation of the data in the same way as BEKS. We determine the characteristic spacing from the position of the highest peak in the power spectrum, and we adjust the phase to match the positions of as many big clumps as possible. The characteristic spacing is indicated by the vertical dashed lines in the top panels in Figure 2.6. Panel (c) shows a good example whose power spectrum has a very high peak while the actual distance distribution does not show a periodic feature (discussed in section 5.3). Panels (d) and (e) show the best examples from our model **L1** and **L2**, respectively, which show a good visual impression that ‘galaxies’ are spaced regularly. Finally panel (f) shows an example from model **L2**, which has a large characteristic length scale of $\sim 200h^{-1}\text{Mpc}$.

$$\begin{aligned} \max\{P(k)\} &= 0.177 \text{ at } k = 7.5 \\ \Delta &= 0.165 \text{ with period } 130h^{-1}\text{Mpc} \\ R &= 0.330 \text{ with period } 130h^{-1}\text{Mpc} \end{aligned}$$

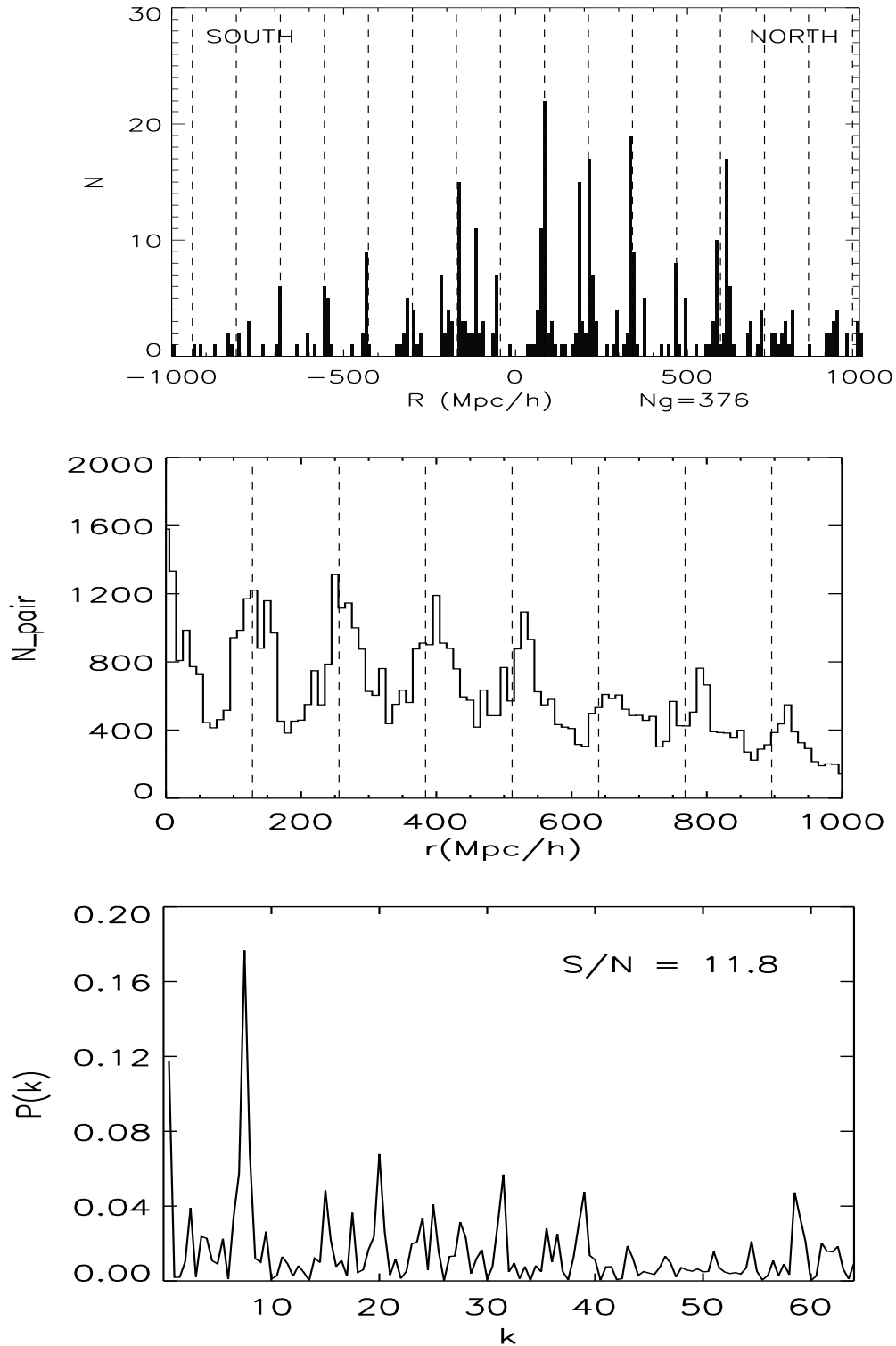


Figure 2.5 The BEKS data.

$$\begin{aligned} \max\{P(k)\} &= 0.145 \text{ at } k = 8.5 \\ \Delta &= 0.164 \text{ with period } 120h^{-1}\text{Mpc} \\ R &= 0.574 \text{ with period } 70h^{-1}\text{Mpc} \end{aligned}$$

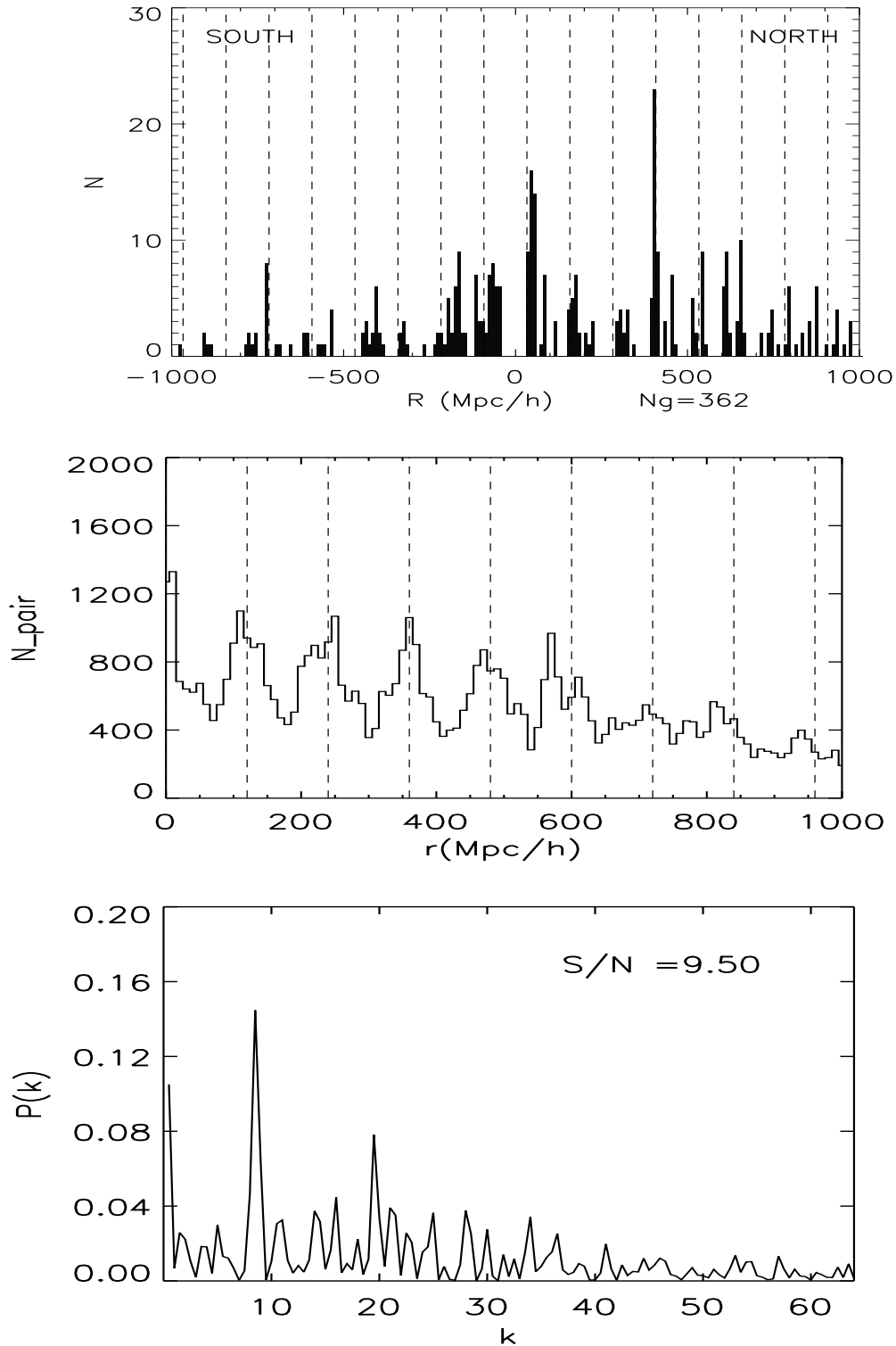
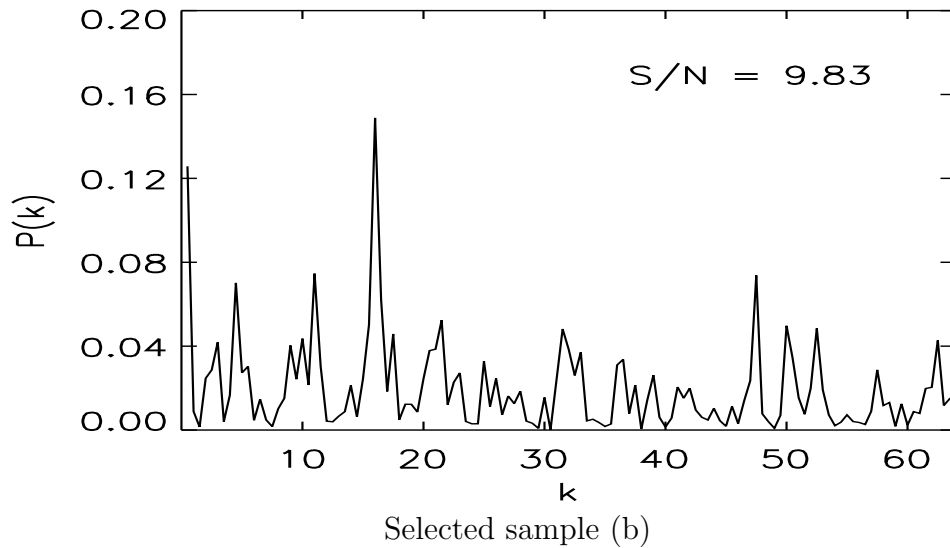
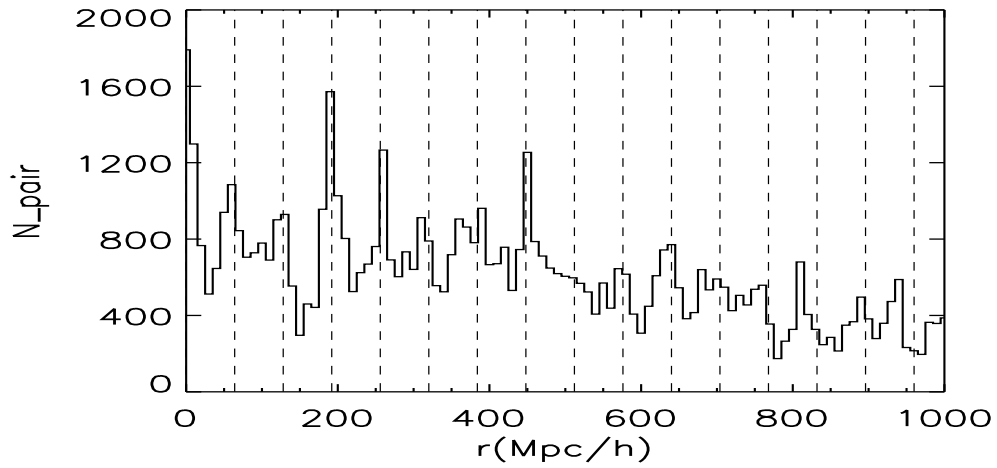
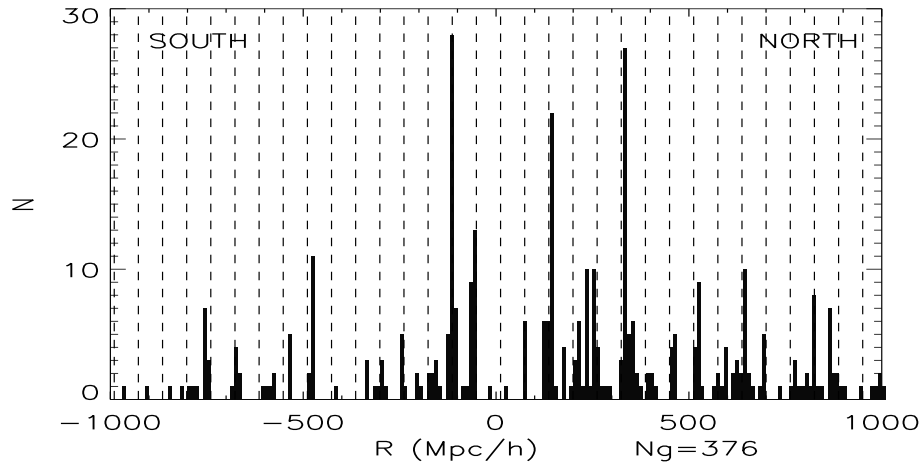
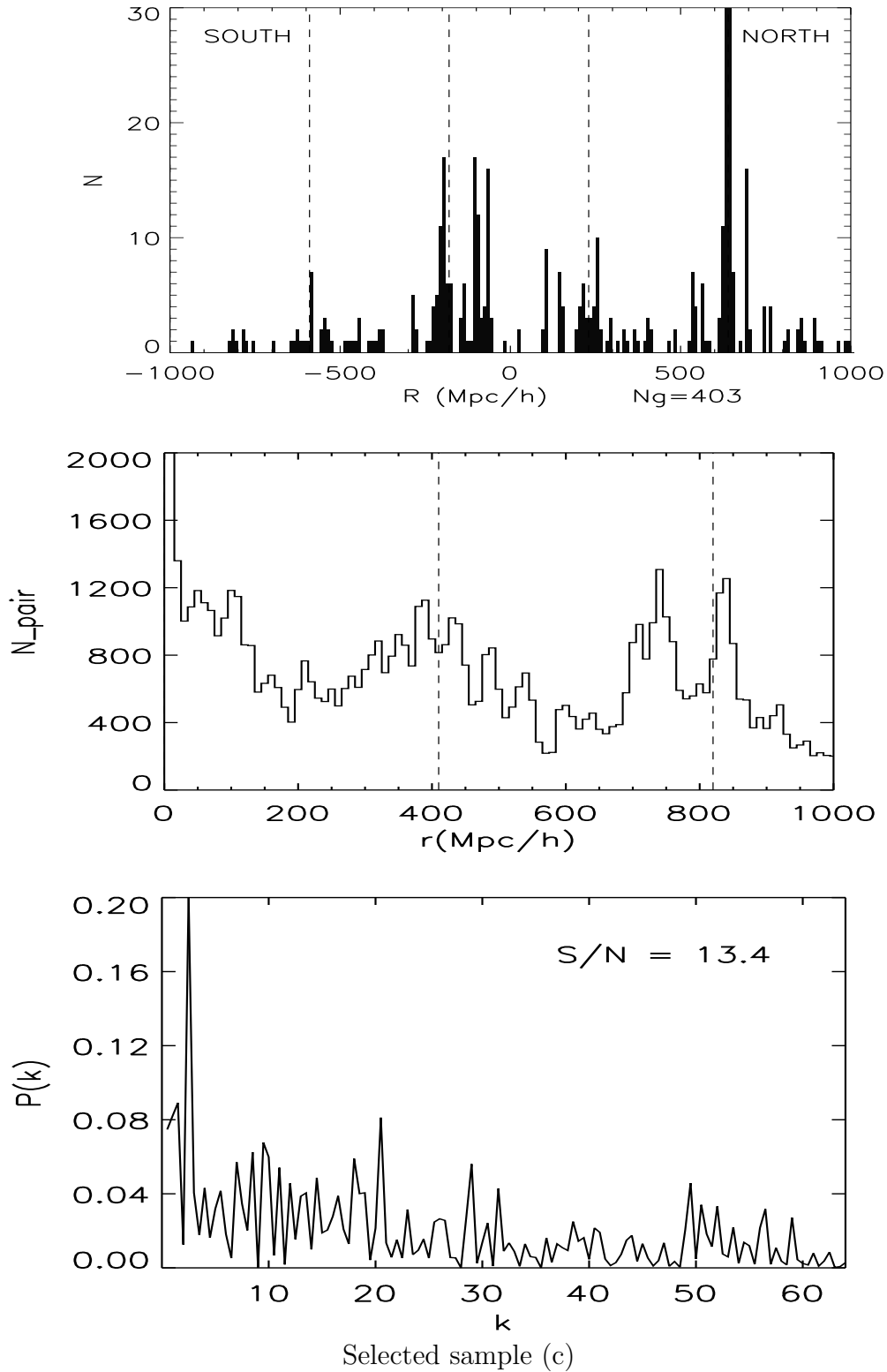


Figure 2.6 Selected sample (a)

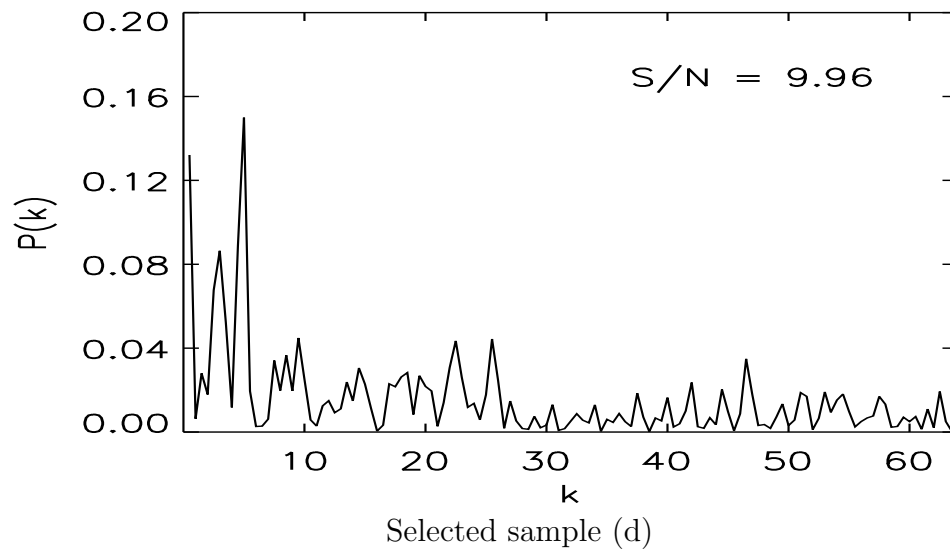
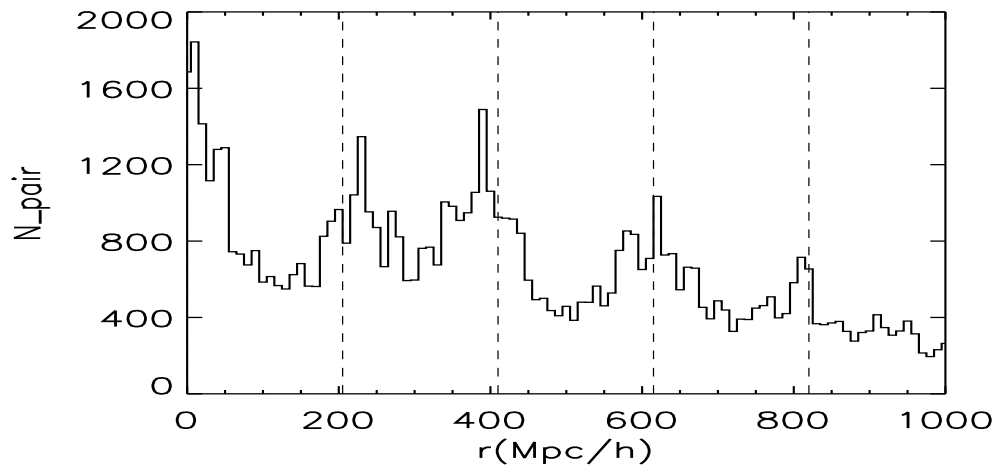
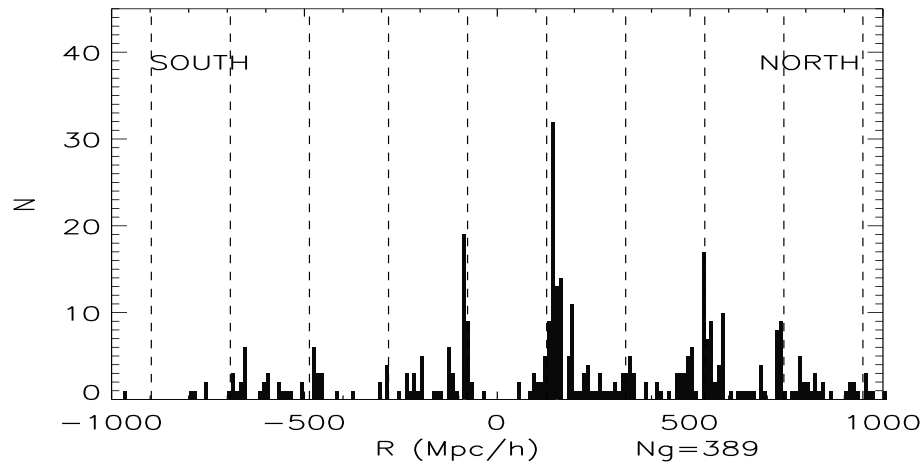
$$\begin{aligned} \max\{P(k)\} &= 0.149 \text{ at } k = 16 \\ \Delta &= 0.167 \text{ with period } 220h^{-1}\text{Mpc} \\ R &= 0.576 \text{ with period } 190h^{-1}\text{Mpc} \end{aligned}$$



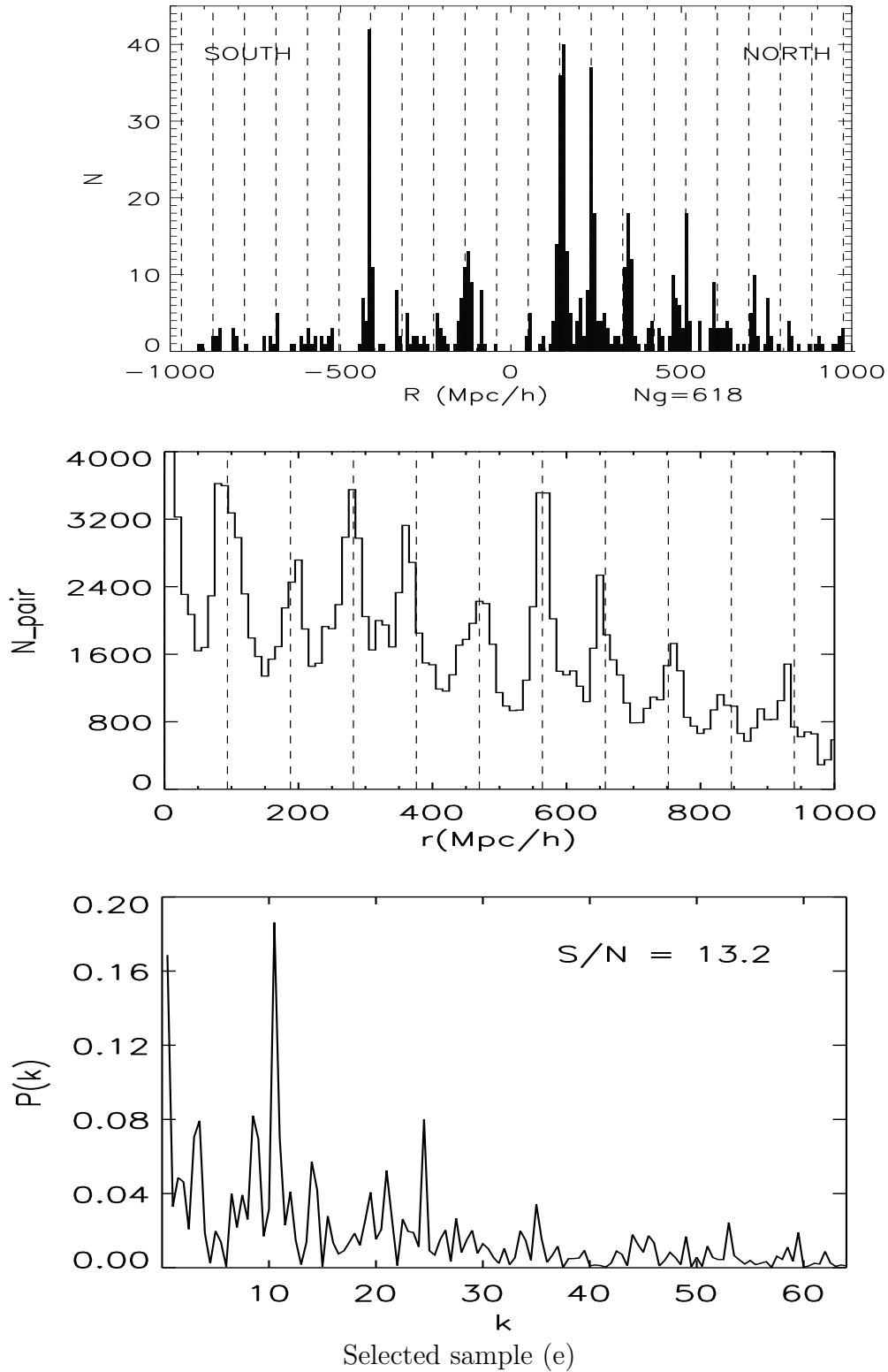
$$\begin{aligned} \max\{P(k)\} &= 0.201 \text{ at } k = 2.5 \\ \Delta &= 0.152 \text{ with period } 830h^{-1}\text{Mpc} \\ R &= 0.505 \text{ with period } 160h^{-1}\text{Mpc} \end{aligned}$$



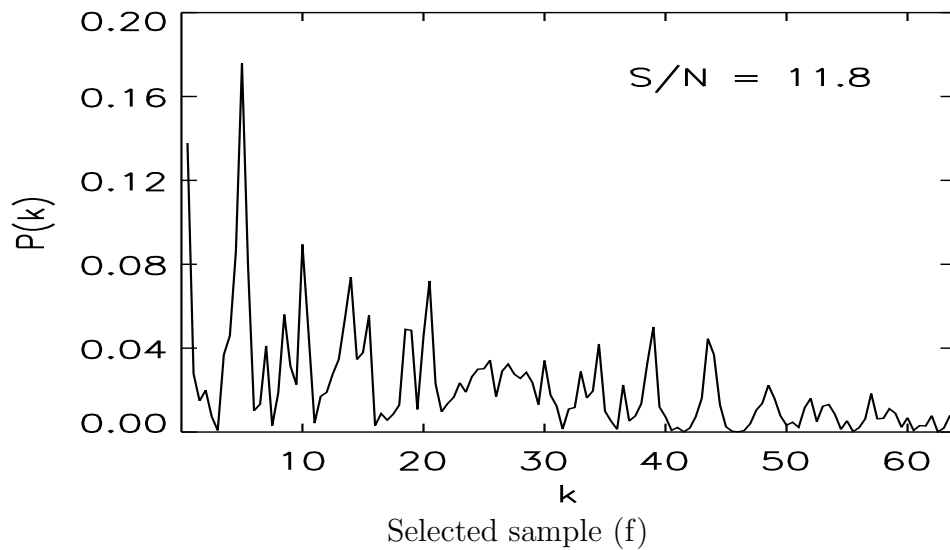
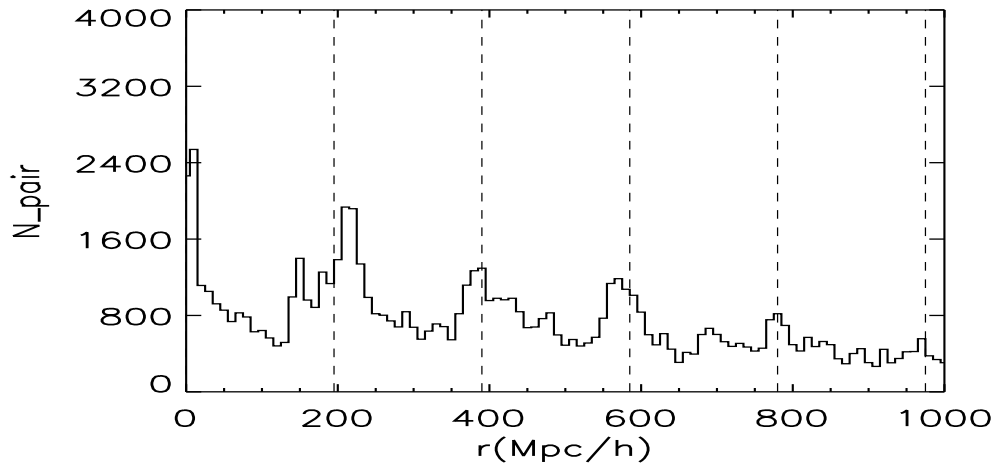
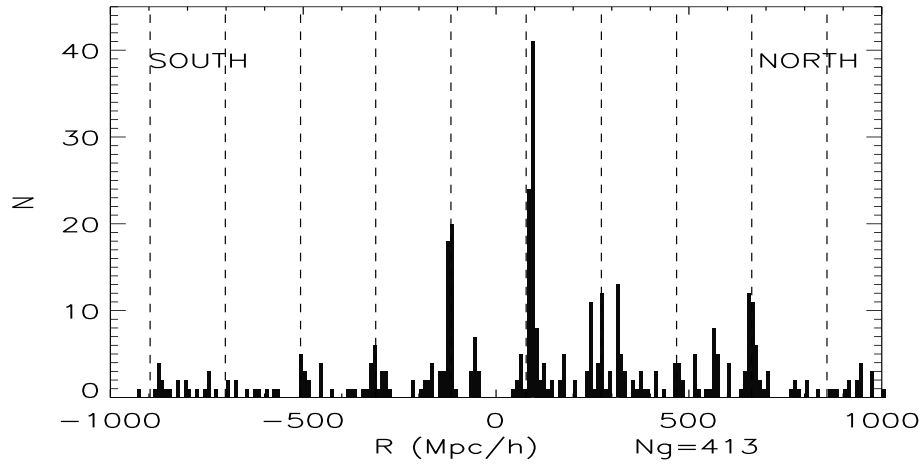
$$\begin{aligned} \max\{P(k)\} &= 0.150 \text{ at } k = 5.0 \\ \Delta &= 0.159 \text{ with period } 200h^{-1}\text{Mpc} \\ R &= 0.358 \text{ with period } 200h^{-1}\text{Mpc} \end{aligned}$$



$$\begin{aligned} \max\{P(k)\} &= 0.186 \text{ at } k = 10.5 \\ \Delta &= 0.160 \text{ with period } 90h^{-1}\text{Mpc} \\ R &= 0.475 \text{ with period } 90h^{-1}\text{Mpc} \end{aligned}$$



$$\begin{aligned} \max\{P(k)\} &= 0.176 \text{ at } k = 5.0 \\ \Delta &= 0.155 \text{ with period } 190h^{-1}\text{Mpc} \\ R &= 0.572 \text{ with period } 190h^{-1}\text{Mpc} \end{aligned}$$



2.5.2 Pairwise separation histograms

From the apparent distance distributions of the ‘galaxies’, it is easy to produce histograms of pairwise distance differences which can be used to search for characteristic scales in the structure within our pencil-beam surveys. Such pair counts are shown in the middle plot of each panel in Figure 2.6. These counts typically display a series of peaks and valleys which are particularly prominent in panels (a), (e) and (f), and, as noted by BEKS themselves, in the original BEKS data. Notice that these peaks appear regularly spaced as indicated by the dashed lines in these panels. The contrast between peaks and valleys can be used as a measure of the strength of the regularity. For the BEKS data the height difference between the first peak and the first valley is about a factor of 3, while the corresponding numbers are 2.4, 2.2 and 3.4 in panels (a), (e), and (f), respectively. Many of our artificial samples show a more complex behaviour, however. In panel (b) there is a deep valley at $150h^{-1}\text{Mpc}$ followed by a high peak at $200h^{-1}\text{Mpc}$; the contrast is a factor of 5.3 despite this uneven spacing. A robust and intuitive definition of contrast is difficult to find. An alternation of small-scale peaks and valleys can coexist with apparently significant larger scale variations as is clearly seen in panel (c). If we focus specifically on the strongest peaks and valleys, their ratio, and indeed even their identification can depend on the specific binning chosen for the histograms. Because of these ambiguities we will not use these distributions further for quantitative analysis in this chapter.

2.5.3 Power spectra

In order to compare our results directly with BEKS we calculate one-dimensional power spectra for our samples using the method described in Szalay et al. (1991). Each galaxy is represented by a Dirac delta-function at the distance inferred from its redshift (including its peculiar velocity). The power in each Fourier component is then

$$f_k = \frac{1}{N_g} \sum_n \exp(2\pi i k r_n), \quad (2.2)$$

$$P_k = |f_k|^2 \quad (2.3)$$

where N_g is the total number of galaxies in the sample. The power spectra calculated in this way for our various samples are shown in the bottom plots of each panel in Figure 2.6. Our units are such that the wavelength corresponding to wavenumber k is $1000/k h^{-1}\text{Mpc}$. In panels (a) and (b) visual impression

of the separation of clumps is consistent with the wavelength inferred from the power spectra. The highest peak is at $k=8.0$ in panel (a) and $k=16.0$ in panel (b), giving wavelengths of $125h^{-1}\text{Mpc}$ and $62.5h^{-1}\text{Mpc}$, respectively. As we shall see, there is no unique length scale inferred from the power spectra.

If a pencil-beam penetrates a rich cluster, an interesting feature can arise. For example, in panel (c) there is a single large cluster at $600h^{-1}\text{Mpc}$. Together with a few other clumps of moderate size, it produces a very high peak in the power spectrum *without* the distance distribution as a whole giving a visual impression of regularity (c.f. the top panel of panel (c)). Many of our samples in both the τCDM and ΛCDM ensembles show high peaks in the power spectra with no apparent periodicity. Thus a very high peak in the power spectrum, particularly at low wave-number, is a poor indicator of the kind of regularity which is so striking in the original BEKS data. Interestingly, as Bahcall (1991) pointed out, if one of the BEKS survey beams passed near the centre of a rich cluster, the galaxy count in the corresponding distance bin would have been much larger than the maximum of 22 seen in the actual BEKS data (see also Willmer et al. 1994). (For comparison, the maximum bin count in the histogram of panel (a) is 23.) We note that the Poisson sampling noise in each power spectrum can be estimated as $1/N_g$. As a result, a big clump raises the statistical significance of ‘structure’ both by enhancing the strength of peaks and by lowering the estimated noise.

In order to compare samples with different total numbers of ‘galaxies’, we calculate the signal-to-noise ratio of the highest peak in the power spectrum following the procedure of Szalay et al. (1991). We define the peak-to-noise ratio of a sample as, $X=(\text{peak height})/(\text{noise level})$ where the noise is estimated from the sum in quadrature of the Poisson sampling noise and the clustering noise,

$$f_0 = \frac{1}{N_g} + \frac{\xi_0}{M}, \quad (2.4)$$

where, as before, N_g is the total number of galaxies in the sample, ξ_0 is the small-scale two point correlation function averaged over a cell of depth $30h^{-1}\text{Mpc}$, and M is the number of cells along the survey axis. We use the value $\xi_0/M = 1/80$ as in Szalay et al. (1991). Although Szalay et al. derived this formula from a simple model with cylindrical geometry, they showed that this estimator agrees well with another internal estimator calculated from the cumulative distribution of power. To facilitate direct comparison with the earlier work we also use equation (2.4) to compute signal-to-noise ratios for the highest peaks in our samples. These S/N ratios are given in each of the power spectrum plots in Figure 2.6. Figure 2.7 shows both the differential and the

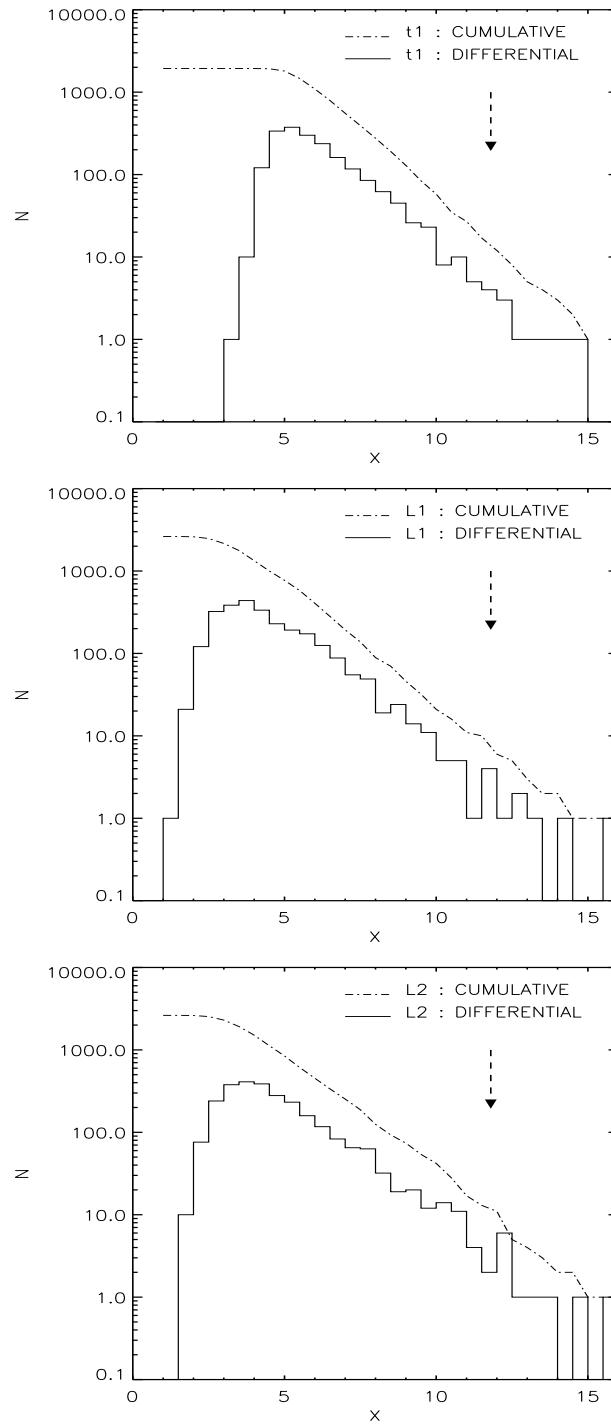


Figure 2.7 The cumulative (histogram) and the differential (dot-dashed line) distribution of the peak-to-noise ratio for τ CDM bias **t1** (top), Λ CDM bias **L1** (middle), and Λ CDM bias **L2** (bottom). Note the difference in the total number of samples in the two models. The arrow indicates the peak-to-noise ratio of the BEKS data.

cumulative distribution of peak-to-noise ratio in our mock surveys. The principal difference between the τ CDM and Λ CDM ensembles lies in the position of the peak in the differential count. For both **L1** and **L2** the peak is at smaller X than in **t1**. This difference can be traced to the value of Ω we assume for analysis. Adopting $\Omega = 1$ for converting redshift to physical distance causes the value of M , the number of cells of width $30h^{-1}\text{Mpc}$ along the survey axis, to be underestimated for Λ CDM. Using the noise estimator (3) with this value of M then overestimates the noise levels for **L1** and **L2** (see SubbaRao and Szalay (1992) for discussion of a similar point).

We plot in Figure 2.8 the wavenumber distribution of the peaks whose S/N ratios are higher than that of the original BEKS data ($X=11.8$). We find 14 samples satisfy this condition in **t1**, 7 in **L1** and 13 in **L2**. The distributions of the peaks with $X > 8.0$ (the ‘tails’ of the number count in Figure 2.7) are also shown in Figure 2.8. By checking the distance distributions we have found that highly significant peaks at $k \leq 5$ are almost always due to one or two strong clumps, as noted above. Very few catalogues give a high peak on scales similar to the BEKS data. It is interesting that the frequency of such catalogues is significantly higher in **t1** than in **L1** and **L2**. The difference is primarily due to the number density of rich clusters over the redshift range surveyed. Deep pencil-beams in our **L1** and **L2** models have more chance than in **t1** to hit a rich cluster at redshift $\sim 0.3 - 0.5$. Then high peaks in the power spectra tend to appear on small wavenumbers in **L1** and **L2** for the reason explained above.

Overall, we conclude that although roughly half a per cent of our mock surveys give a power spectrum peak stronger than that of the BEKS data, very few of these actually correspond to redshift distributions with similar regularity and similar spacing of the spikes. We now study this further by considering two additional tests for regularity which have been used on the BEKS sample.

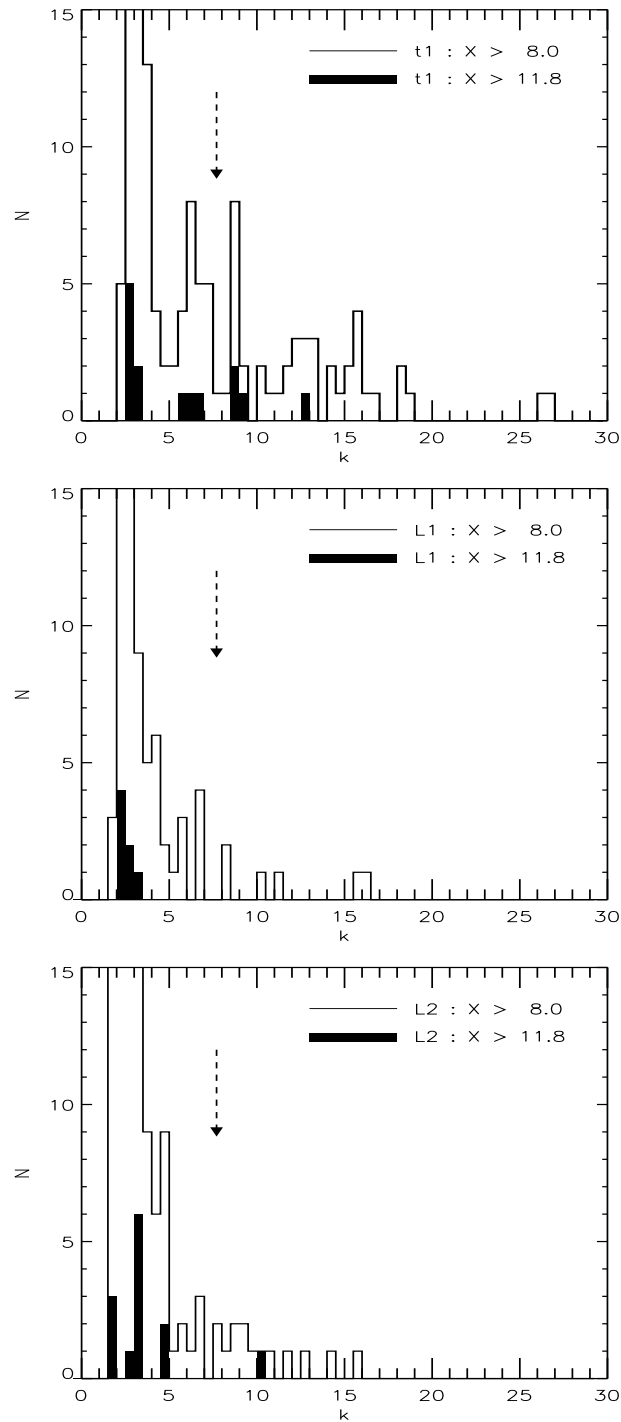


Figure 2.8 The distribution of wavenumbers for the high peaks. The shaded histograms show the number counts of the peaks with $X \geq X_{\text{BEKS}}$, and the unshaded histograms show those with $X \geq 8.0$. The arrow indicates the peak wavenumber of the BEKS data.

2.6 PG Δ -TEST

In comparing their own simulation to the BEKS data, Park & Gott (1991) made use of a test specifically designed to probe the apparent “phase-coherence” of the series of redshift spikes. For each ‘galaxy’ they calculated the distance to the nearest tooth of a perfectly regular comb-like template. They then ratioed the mean of this distance to the separation of the teeth, and minimised the result over the period and phase of the template. Let us call the resulting statistic Δ . Then a distribution in which each galaxy is at some node of a regular grid will give $\Delta = 0$, and a uniform distribution in distance would give $\Delta = 0.25$ in the large-sample limit. In our application of this test we restrict the range of possible periods to $50 - 500 h^{-1}$ Mpc. For the BEKS data we obtain $\Delta=0.165$ for a best period of $130h^{-1}$ Mpc. Our value of Δ differs from that given by PG because they applied the test only to the deep surveys while we use the combined deep and shallow BEKS data. Among the 1936 samples in our **t1** ensemble, 209 have lower values of Δ than the BEKS data; for the **L1** and **L2** ensembles the corresponding numbers are 134/2625 and 127/2625 respectively. According to this test, therefore, the observed sample appears only marginally more regular than expected in our CDM cosmologies.

Within each of our ensembles the significance of the regularity in the BEKS data appears somewhat higher than was estimated by PG. Their simulation ensemble was made up of only 12 mock catalogues of which one had lower Δ than the BEKS deep data. The median Δ for these twelve was 0.1695, while we find medians of 0.176, 0.180 and 0.189 for the combined deep and shallow data in ensembles **t1**, **L1** and **L2** respectively. The difference with PG is probably small enough to be attributed to the small number of realisations in their ensemble. Figure 2.9 shows the distribution of periods for catalogues in each of our own ensembles with lower Δ s than the BEKS data. It is interesting that relatively small periods are favoured and that there is no preference for values in the range $120 - 130h^{-1}$ Mpc. Ettori et al. (1997) used a related test, the comb-template test (Duari et al. 1992), to analyse four pencil-beam surveys near the South Galactic Pole. They found a best period near $130 h^{-1}$ Mpc in two of these four directions, in apparent agreement with the BEKS result.

In summary, the difference in regularity between the BEKS sample and our CDM mock-catalogues is less significant when measured by the Δ -test than when measured using the power spectrum test of the last section. Nevertheless,

for periods near $125h^{-1}\text{Mpc}$ there are few CDM samples which are more regular than the BEKS data. In addition, our result appears insensitive to the choice of biasing; we find essentially no difference between **L1** and **L2** in Figure 2.9. This is puzzling since Figure 2.3 shows clear differences in the emptiness of the voids in the two cases. Apparently the value of Δ is more sensitive to departures from regularity in the spacing of the walls than it is to the density contrast of the voids.

2.7 SUPERCLUSTER STATISTICS

Dekel et al. (1992) proposed an alternative technique for assessing apparent periodicity in data samples like that of BEKS. In this section we use the term ‘supercluster’ to refer to clumps in the one-dimensional redshift histograms derived from such pencil-beam surveys, even though these do not correspond precisely to the superclusters (or walls or filaments) seen in fully three-dimensional surveys. The method of Dekel et al. is based on the redshift distribution of supercluster centres rather than on that of individual galaxies. The first step is to correct the galaxy redshift histogram for the survey selection function. We do this by weighting each galaxy by the inverse of the selection function for the particular survey of which it is a part (North or South, shallow or deep). This reverses the procedure by which we created our mock catalogues from the simulations. To avoid overly large sampling noise where the selection function is small, we restrict our redshift histograms to $z \leq 0.31$ for the SGP survey and $z \leq 0.5$ for the NGP survey (see Dekel et al. 1992). We smooth these histograms with a Gaussian of variance l^2 and identify supercluster centres as local maxima of the result. (Note that, following Dekel et al., no threshold is applied.) We have tried smoothing lengths l between 20 and $40 h^{-1}\text{Mpc}$, but find our results to be insensitive to the exact value within this range. In what follows we set $l = 25 h^{-1}\text{Mpc}$.

Given a distribution of the supercluster centres, the characteristic period is determined in the following way. As a first estimate we take the mean separation L_m between neighbouring superclusters. Next we apply the PG Δ -test for periods $p \in [0.5L_m, 2.0L_m]$. The value of p in this range which

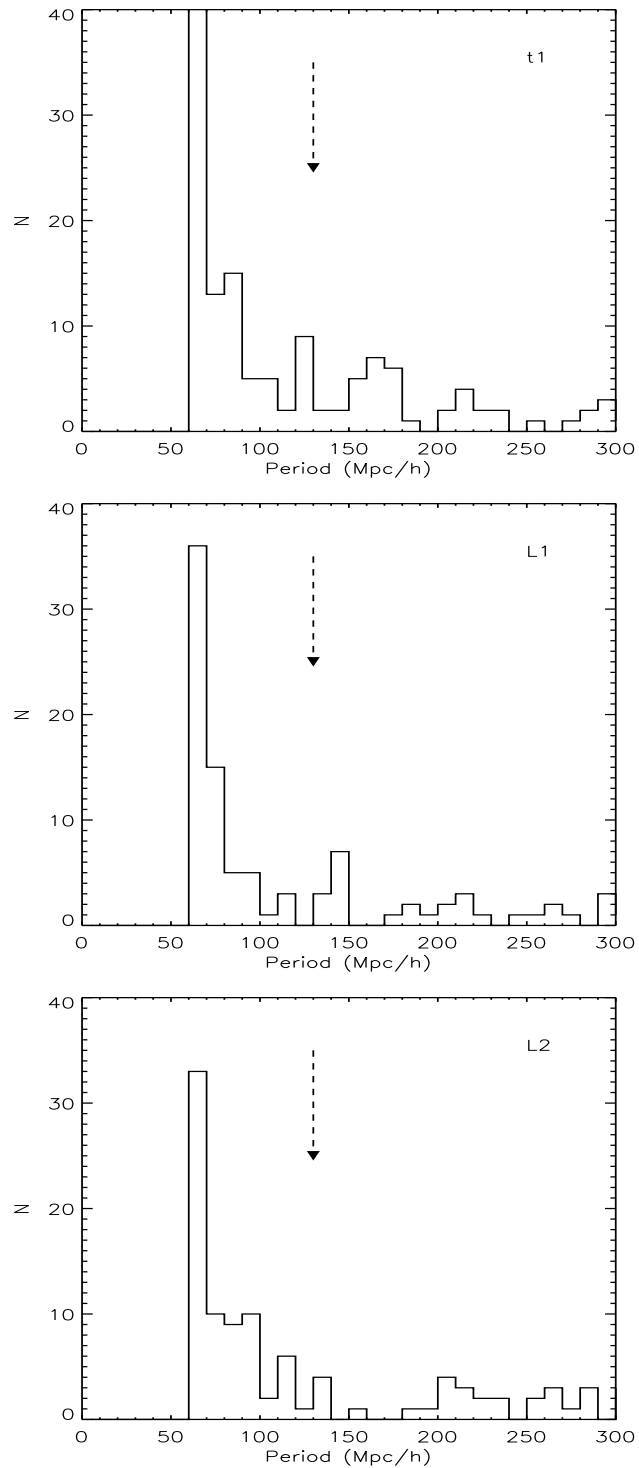


Figure 2.9 Δ -test: the number counts of selected samples with $\Delta < \Delta(\text{BEKS})$ are plotted against the measured period (see text). The period of the BEKS data is shown by an arrow at $130 h^{-1}\text{Mpc}$.

minimises Δ is taken as the characteristic period of the distribution. For this period we calculate the Rayleigh statistic R as follows (Dekel et al. (1992) and Feller(1971)). The positions of the supercluster centres are mapped onto a circle of circumference p . Consider the n unit vectors \mathbf{u}_i which point from the centre of the circle towards each of the n superclusters. Denote their vector average by $\langle \mathbf{u} \rangle$, the modulus of $\langle \mathbf{u} \rangle$ by V and define $R = 1 - V$. For an exactly periodic distribution the unit vectors would all be identical so that $V = 1$ and $R = 0$. For a distribution with no long-range phase coherence the directions of the unit vectors would be random and so in the large sample limit $V \sim 0$ and $R \sim 1$. Small values of R are thus expected for near-periodic distributions.

For the BEKS data, we find $R = 0.33$ for a period of $130 h^{-1}\text{Mpc}$ obtained as described above. Lower values of R are found for 46 samples in **t1**, for 66 samples in **L1**, and for 56 samples in **L2**. Thus, according to this test the supercluster distribution in the BEKS data is more periodic than the CDM models at the 2.4 per cent significance level for **t1**, the 2.5 per cent level for **L1** and the 2.1 per cent level for **L2**. The period distribution of the samples with $R \leq R(\text{BEKS})$ is shown in Figure 2.10. Many of these low- R samples have periods in the range $[100h^{-1}\text{Mpc}, 140h^{-1}\text{Mpc}]$. Thus in CDM model universes it is common for supercluster spikes to have a typical separation similar to that seen in the BEKS data and in a few per cent of cases the spikes are just as regularly spaced as in the real data.

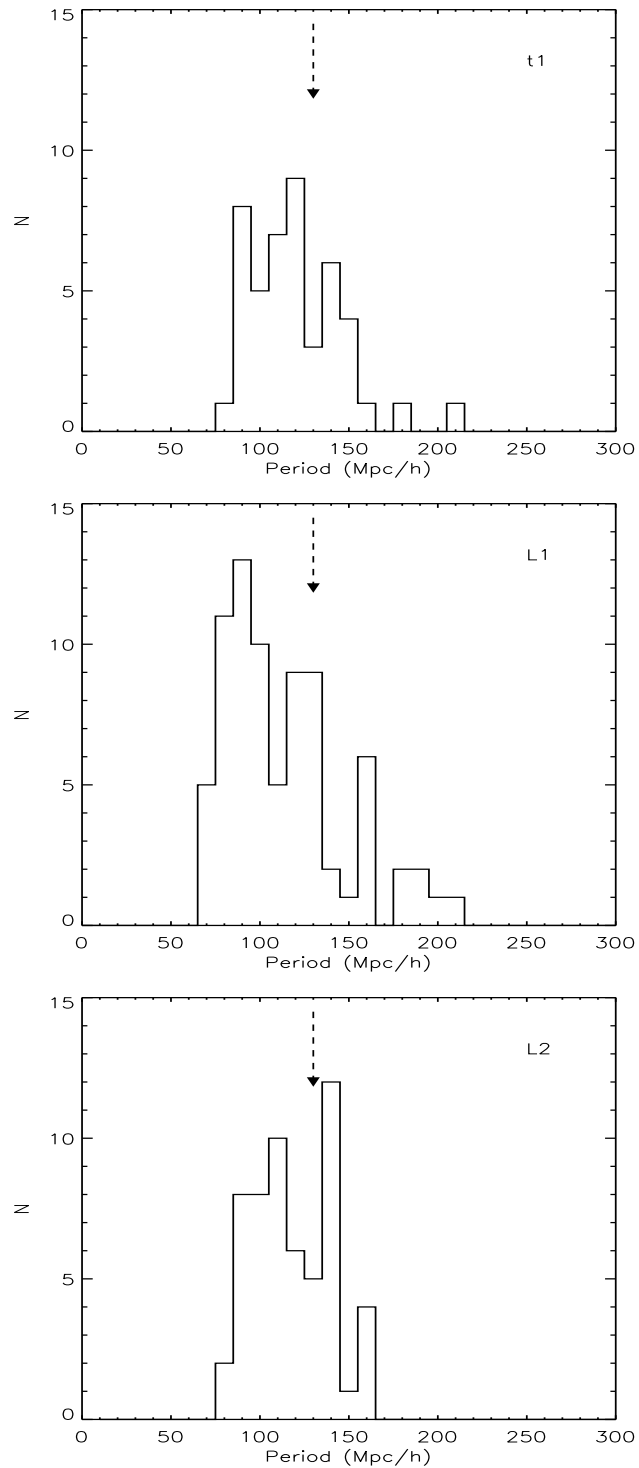


Figure 2.10 The Rayleigh statistic R . The number counts of $R < R(\text{BEKS})$, plotted against the period assigned to each of the samples for the Rayleigh statistic. The arrow indicates the period for the BEKS data.

2.8 DISCUSSION AND CONCLUSION

By creating a number of mock pencil-beam surveys we have compared the apparent periodicity in two CDM model universes with that observed in the data of Broadhurst et al. (1990). The power spectrum analysis alone shows that the BEKS data are significantly more periodic than the models at about the half per cent level, while the PG Δ -test shows less significance, about 10 per cent for **t1** and 5 per cent for **L1** and **L2**. The supercluster statistic gives a two per cent probability of finding a structure as regular as the BEKS data. Restricting to a length scale $\sim 100\text{-}150h^{-1}\text{Mpc}$, however, the number of samples which show the kind of periodicity seen in the BEKS data is extremely small for each of these statistics. Overall no sample is more regular than the BEKS data for *all* three statistics for a single period. The two popular CDM models we have studied here are apparently unsuccessful in reproducing the observed periodicity. From this result together with the fact that the statistical results appeared to be insensitive to the choice of the bias model, we conclude that CDM models conflict with the BEKS observation. Either the models need additional physics, or the data are a fluke or are somehow biased.

Various possible physical explanations have been proposed, such as coherent peculiar velocities (Hill, Steinhardt and Turner 1991) oscillations in the Hubble parameter (Morikawa 1991) or baryonic features in the power spectrum (Eisenstein et al. 1998) but all of them seem to require either additional mechanisms with fine tunings beyond the standard theory or cosmological parameters significantly different from currently favoured values. Intriguingly, Dekel et al. (1992) demonstrated that built-in power on a large ($\sim 100h^{-1}\text{Mpc}$) length scale in the initial density fluctuation could indeed reproduce periodic features on a given scale, at least by some of the tests we have considered. If such excess power on large scales (hence still in the linear regime) exists, it will be detectable in the power spectra of the future 2dF and Sloan surveys.

Having found at least a few examples that are nearly as periodic as the BEKS data, we cannot rule out the possibility that the BEKS data (or the Galactic Pole direction) are a fluke. On the other hand, one should be aware of the complexity of the original observations –an incomplete compilation of a narrow and deep, and of a wide and shallow survey at each of the Galactic Poles. It is not clear whether such a combination constitutes a fair sample. No evidence for periodic structure on $\sim 130h^{-1}\text{Mpc}$ has been found so far

in two other deep redshift surveys, the ESO-Sculptor Survey (Bellanger and de Lapparent 1995) and the Caltech Faint Galaxy Redshift Survey (Cohen 1999). Follow-up observations to BEKS by Koo et al. (1993) did *not* show a strong regularity in two other directions, although around the Galactic Pole the regularity was found to be further strengthened. Our results give the *a priori* probability for such apparent periodicity in CDM models. Several more deep surveys might suffice to judge whether the discrepancy with BEKS reflects a major inconsistency. The planned VIRMOS Deep Survey (Le Fèvre et al. 1998, see also Guzzo 1999) will survey the range $0.3 \leq z \leq 1$ and will provide, together with the large volume 2dF and Sloan surveys, much larger and more complete samples in the near future.

CHAPTER 3

Self-interacting dark matter

3.1 INTRODUCTION

By comparing the mass of all the individual galaxies in the Coma cluster with the total mass required for gravity to produce their observed motions, Fritz Zwicky showed in 1933 that most of the mass of the cluster must be in some unknown and invisible form. Nearly seventy years later his conclusion has been confirmed for many other galaxy clusters, and it is now generally believed that the most of the mass in the universe is in some dark form which has still been detected only through its gravitational effects. Currently popular models for the formation of structure in the universe assume that this dark matter is made of vast numbers of free elementary particles which are *collisionless*, that is that they interact with each other and with other matter only through gravity. Cold dark matter, which was non-relativistic (hence “cold”) when it decoupled from other matter in the early universe, has proven to be the most promising candidate due to its natural motivation from particle physics and its success at reproducing a host of observations on large scales (Davis et al. 1985). However, it was recently argued that observations on galactic scales, such as the rotation curves of dwarf galaxies and the abundance of substructure in our Milky Way’s halo, appear to conflict with the predictions from the conventional CDM models. David Spergel and Paul Steinhardt (2000) proposed that the conflict might be resolved if the cold dark matter particles are self-interacting with a large scattering cross-section. In their model the dark matter particles occasionally collide elastically as they move through galaxies and galaxy clusters, and it is expected that such collisions significantly alter the matter distribution in galaxies and galaxy clusters.

In this chapter we investigate the viability of the proposed model in which dark matter is cold but has a large cross-section for elastic collisions. We carry out a set of large numerical simulations of galaxy cluster formation. We show how the internal structure of nonlinear objects (“dark halos”) is affected by the self-interaction.

3.2 CRISIS ON SMALL SCALES...?

Recent measurements of structure in the microwave background radiation (Lange et al. 2000; Hanany et al. 2000; Lee et al. 2001; Netterfield et al. 2001) provide strong support for the general theoretical paradigm on which the CDM model was based. Such cold dark matter scenarios within the standard inflationary universe have been remarkably successful in fitting a wide range of observations. While structure on large scales ($\gg 1$ Mpc) is well reproduced by the models, the structure of nonlinear dark matter dominated systems predicted by the models may be inconsistent with a class of observations on galactic and subgalactic scales. Navarro, Frenk & White (1997, hereafter NFW) claimed that the density profiles of virialised CDM halos are well approximated by a “universal” form with singular behaviour near its centre. More recent simulations with higher resolution have confirmed this result, suggesting that the central cusps may be even steeper than the NFW profile (Moore et al. 1999b; Klypin et al. 1999, see also Jing & Suto 2000). Such structures appear inconsistent with published data on the rotation curves of dwarf galaxies (Moore 1994; Flores and Primack 1994) although this inconsistency may reflect limitations of the data rather than of the theory (van den Bosch et al. 1999; van den Bosch & Swaters 2000). There seems to be a discrepancy between the rich substructure seen in simulations of CDM halos and the small number of satellite galaxies observed in the Milky Way’s halo (Moore et al. 1999a; Klypin et al. 1999).

Ordinary astrophysical processes are unlikely to resolve the problems. Since the baryon fraction in the centres of low surface brightness galaxies is low, hydrodynamic processes are unable to alter their dark matter distribution (Moore 1994, Flores & Primack 1994). Supernova explosions might cause the core density of galaxies to be made smoother, but numerical simulations by MacLow & Ferrara (1999) show that star bursts in dwarf galaxies are very inefficient at removing gas or matter from the centre. One might consider whether the discrepancy in the abundance of subhalos can be explained if star formation in dwarf galaxies is sufficiently suppressed. Even if some physical mechanisms work successfully to remove the baryonic contents from dwarf galaxies, there still remains the disk heating problem; the existence of old thin disks with no halo components suggest that there have not been many infall of compact discrete halos (Moore et al. 1999a).

3.3 STRONGLY SELF-INTERACTING DARK MATTER

3.3.1 Scattering with a large cross-section

On the assumption that an explanation should be sought in fundamental physics, Spergel & Steinhardt (2000) have argued that a large cross-section for elastic collisions between CDM particles may reconcile data and theory. They suggest a number of modifications of standard particle physics models which could give rise to such self-interacting dark matter, and claim that cross-sections which lead to a transition between collisional and collisionless behaviour at radii of order 10 – 100 kpc in galaxy halos are preferred on astrophysical grounds. Ostriker (2000) argues that the massive black holes observed at the centres of many galactic spheroids may arise from the accretion of such collisional dark matter onto stellar mass seeds. Miralda-Escude (2000) argues that such dark matter will produce galaxy clusters which are rounder than observed and so can be excluded.

At early times the CDM distribution is indeed cold, so the evolution of structure is independent of the collision cross-section of the CDM particles. At late times, however, a large cross-section leads to a small mean free path and so to fluid behaviour in collapsed regions. In this section we explore how the structure of nonlinear objects (“dark halos”) is affected by this change. We simulate the formation of a massive halo from CDM initial conditions in two limits: purely collisionless dark matter and “fluid” dark matter.

3.3.2 The N -body/SPH simulation

Our simulations use the parallel tree code GADGET (Springel, Yoshida & White 2001). Our chosen halo is the second most massive cluster in the Λ CDM simulation of Kauffmann et al. (1999). We analyse its structure in the original simulation and in two higher resolution resimulations. In the collisionless case these are the lowest resolution members of a set of four resimulations carried out by Springel et al. (2001a) using similar techniques to those of NFW. Details may be found there and in Springel et al. (2001c). These collisionless resimulations use GADGET as an N -body solver, whereas our collisional resimulations start from identical initial conditions but use the code’s Smoothed Particle Hydrodynamics (SPH) capability to solve the fluid equations. The SPH method regards each simulation particle as a “cloud” of

Table 3.1 Parameters of the S-cluster simulations

Run	N_{tot}	N_{high}	$m_p (h^{-1}M_{\odot})$	$l_s (h^{-1}\text{kpc})$
S0	3.2×10^6	0.2×10^6	1.4×10^{10}	30
S1	3.5×10^6	0.5×10^6	0.68×10^{10}	20
S2	5.1×10^6	2.0×10^6	0.14×10^{10}	3.0

fluid with a certain kernel shape. These clouds interact with each other over a length scale which is determined by the local density and so varies both in space and time. The basic parameters of our simulations are tabulated in Table 3.1, where N_{tot} is the total number of particles in the simulation, N_{high} the number of particles in the central high-resolution region, m_p is the mass of each high-resolution particle, and l_s stands for the gravitational softening length. Our cosmological model is flat with matter density $\Omega_m = 0.3$, cosmological constant $\Omega_{\Lambda} = 0.7$ and expansion rate $H_0 = 70\text{km}^{-1}\text{Mpc}^{-1}$. It has a CDM power spectrum normalised so that $\sigma_8 = 0.9$. The virial mass of the final cluster is $M_{200} = 7.4 \times 10^{14}h^{-1}M_{\odot}$, determined as the mass within the radius $R_{200} = 1.46h^{-1}\text{Mpc}$ where the enclosed mean overdensity is 200 times the critical value.

3.3.3 Matter distribution

On scales larger than the final cluster, the matter distribution in all our simulations looks similar. This is no surprise. The initial conditions in each pair of simulations are identical, so particle motions only begin to differ once pressure forces become important. Furthermore the initial perturbation fields in simulations of differing resolution are identical on all scales resolved in both models, and even S0 resolves structure down to scales well below that of the cluster. As is seen clearly in Figure 3.1, a major difference between the collisional and collisionless models is that the final cluster is nearly spherical in the former case and quite elongated in the latter. The axial ratios determined from the inertia tensors of the matter at densities exceeding 100 times the critical value are 1.00:0.96:0.84 and 1.00:0.72:0.63 respectively. Again this is no surprise. A slowly rotating fluid body in hydrostatic equilibrium is required to be nearly spherical, but no such constraint applies in the collisionless case

(see also Miralda-Escude 2000).

In Figure 3.2 we show circular velocity profiles for our simulations. These are defined as $V_c(r) = \sqrt{GM(r)/r}$, where $M(r)$ is the mass within a sphere radius r ; they are plotted at radii between $2l_s$ and $5R_{200}$. They agree reasonably well along each sequence of increasing resolution, showing that our results have converged numerically on these scales. Along the fluid sequence the profiles resemble the collisionless case over the bulk of the cluster. In the core, however, there is a substantial and significant difference; the fluid cluster has a substantially steeper central cusp. The difference extends out to radii of about $0.5R_{200}$ and has the wrong sign to improve the fit of CDM halos to published rotation curves for dwarf and low surface brightness galaxies. (Note that in the fluid case we expect small halos to approximate scaled down but slightly *more* concentrated versions of cluster halos, as in the collisionless case studied by Moore et al. (1999a); this scaling will *fail* for intermediate cross-sections because the ratio of the typical mean free path to the size of the halo will decrease with halo mass.)

3.3.4 Substructure abundance

In Figure 3.3 we compare the level of substructure within R_{200} in our various simulations. Subhalos are identified using the algorithm SUBFIND by Springel (1999) which defines them as maximal, simply connected, gravitationally self-bound sets of particles which are at higher local density than all surrounding cluster material. (Our SPH scheme defines a local density in the neighbourhood of every particle.) Using this procedure we find that 1.0%, 3.4% and 6.7% of the mass within R_{200} is included in subhalos in S0, S1 and S2 respectively. Along the fluid sequence the corresponding numbers are 3.0%, 6.4% and 3.1%. The difference in the total amount results primarily from the chance inclusion or exclusion of infalling massive halos near the boundary at R_{200} . In Figure 3.3 we show the mass distributions of these subhalos. We plot each simulation to a mass limit of 40 particles, corresponding approximately to the smallest structures we expect to be adequately resolved in our SPH simulations. Along each resolution sequence the agreement is quite good, showing this limit to be conservative. For small subhalo masses there is clearly less substructure in the fluid case, but the difference is more modest than might have been anticipated.

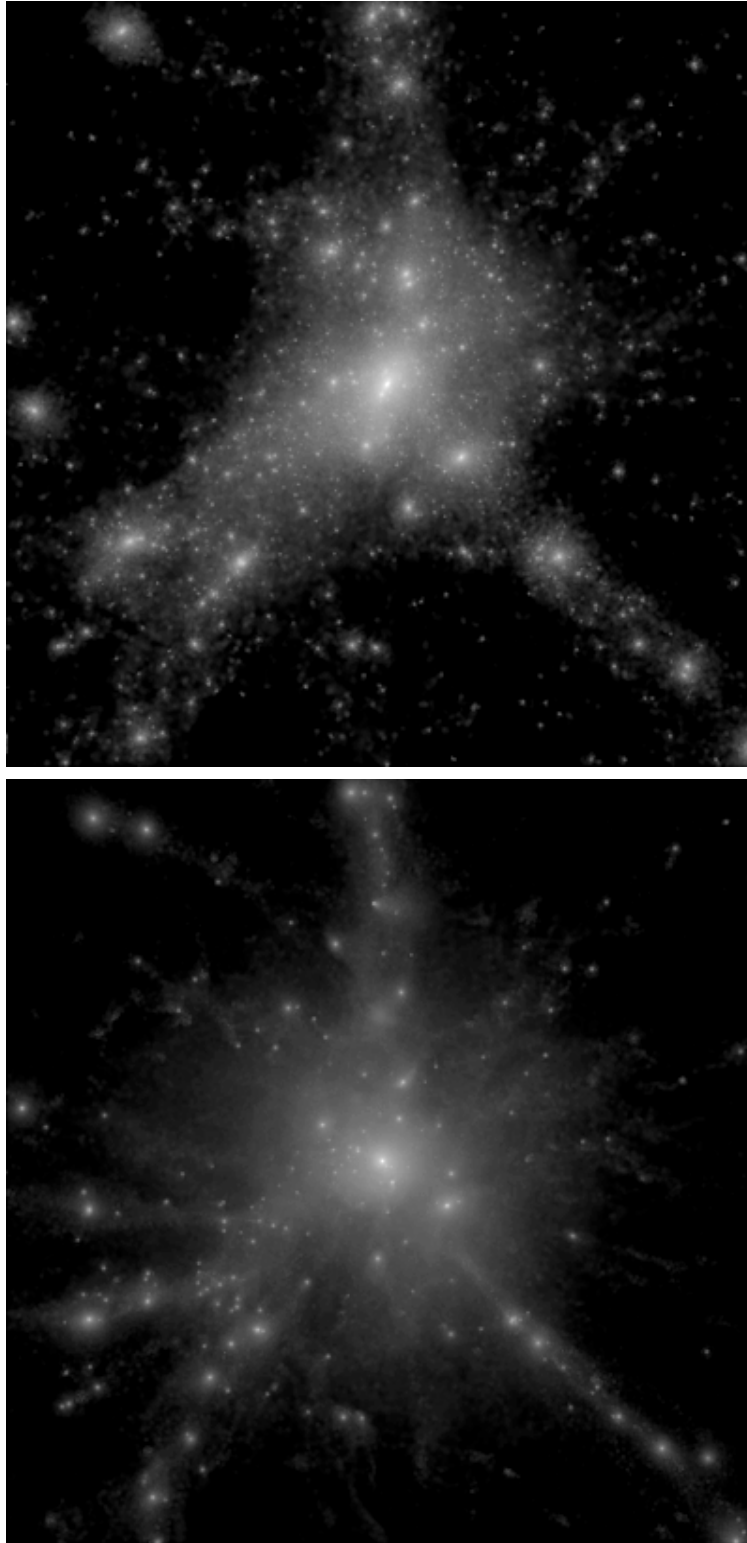


Figure 3.1 The projected mass distribution in our two highest resolution simulations. The collisionless case (S2) is on the top and the fluid case (S2F) is on the bottom. The region shown is a cube of $15h^{-1}\text{Mpc}$ on a side.

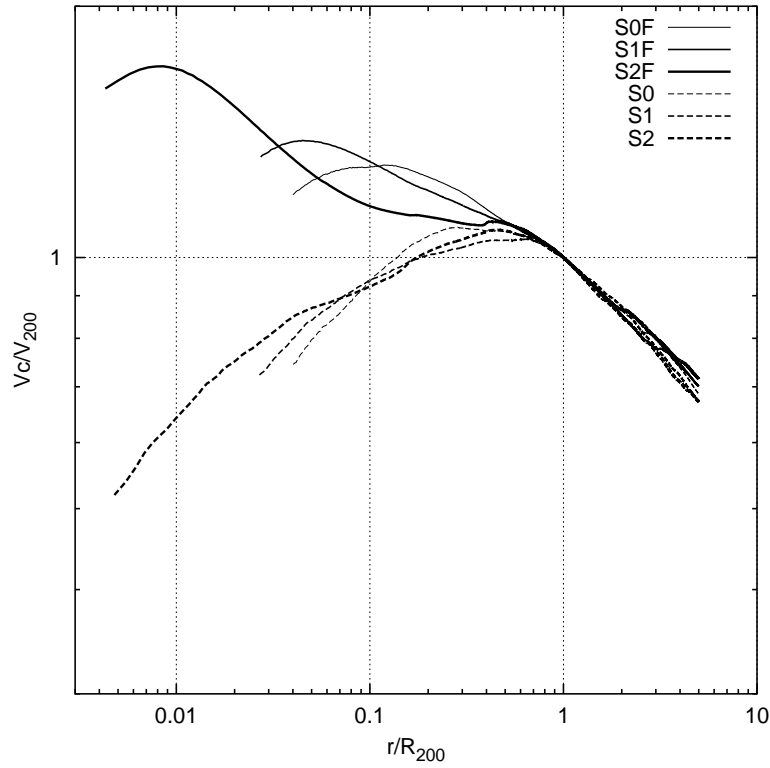


Figure 3.2 Circular velocity profiles for our cluster simulations, each normalised to its own R_{200} and V_{200} . These are plotted between twice the gravitational softening and $5R_{200}$. The collisionless sequence is plotted using dashed lines and the fluid sequence using solid lines.

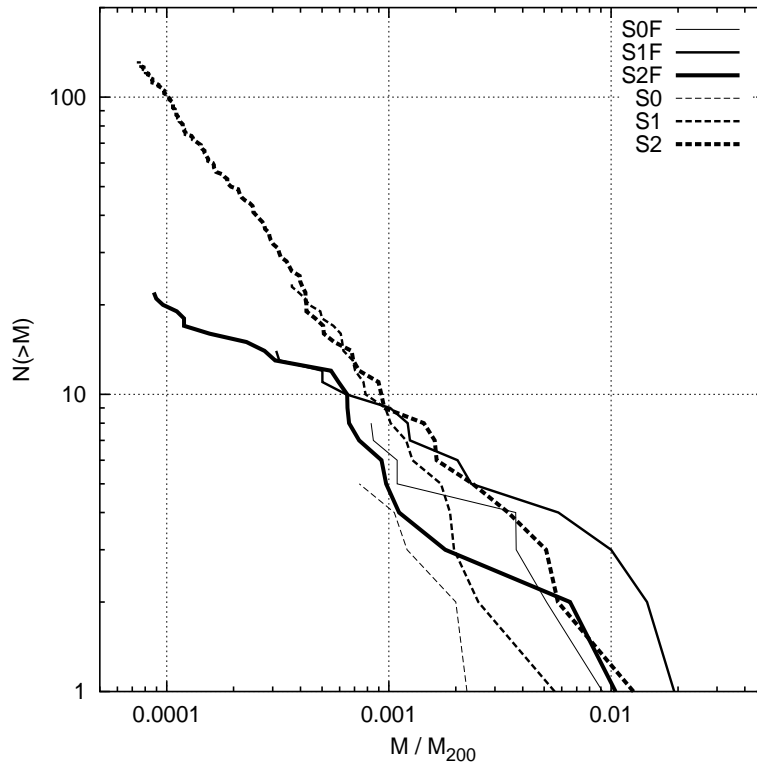


Figure 3.3 The total number of subhalos within R_{200} is plotted as a function of their mass in units of M_{200} . Dashed and solid lines correspond to the collisionless and fluid cases respectively. Results for each simulation are plotted only for halos containing more than 40 particles.

3.3.5 Discussion

An interesting question arising from our results is *why* our fluid clusters have more concentrated cores than their collisionless counterparts. The density profile of an equilibrium gas sphere can be thought of as being determined by its Lagrangian specific entropy profile, i.e. by the function $m(s)$ defined to be the mass of gas with specific entropy less than $s = m_g T^{1.5} / \rho$. The larger the mass at low specific entropy, the more concentrated the resulting profile. Thus our fluid clusters have more low entropy gas than if their profiles were similar to those of the collisionless clusters. The entropy of the gas is produced by a variety of accretion and merger shocks during the build-up of the cluster, so the strong central concentration reflects a relatively large amount of weakly shocked gas. We study gas shocking in our models by carrying out one further simulation. We take the initial conditions of S1 and replace each particle by two superposed particles, a collisionless dark matter particle containing 95% of the original mass and a gas particle containing 5%. These two then move together until SPH pressure forces are strong enough to separate them. The situation is similar to the standard 2-component model for galaxy clusters except that our chosen gas fraction is significantly smaller than observed values.

In this mixed simulation the evolution of the collisionless matter (and its final density profile) is almost identical to that in the original S1. This is, of course, a consequence of the small gas fraction we have assumed. In agreement with the simulations in Frenk et al. (1999) we find that the gas density profile parallels that of the dark matter over most of the cluster but is significantly *shallower* in the inner $\sim 200h^{-1}\text{kpc}$. Comparing this new simulation (S1M) with its fluid counterpart (S1F) we find that in both cases the gas which ends up near the cluster centre lay at the centre of the most massive cluster progenitors at $z = 1 \sim 3$. In addition it is distributed in a similar way among the progenitors in the two cases. In Figure 3.4 we compare the specific entropy profiles of the cluster gas. These are scaled so that they would be identical if gas each particle had the same shock history in the two simulations. Over most of the cluster there is indeed a close correspondence, but near the centre the gas in the mixed simulation has higher entropy. (This corresponds roughly to $r < 100h^{-1}\text{kpc}$.) As Figure 3.4 shows, this is partly a numerical artifact; the two entropies differ only at radii where two-body heating of the gas by the dark matter particles is predicted to be important in the mixed case. (The effect is absent in the pure fluid simulation.) The weaker shocking in the fluid case is evident from the equivalent ‘‘entropy’’ profile of S1 in Figure 3.4. This lies between those of the two fluid simulations, and in particular significantly

above that of S1F in the central regions.

In conclusion the effective heating of gas by shocks in the fluid case is similar to but slightly weaker than that in the mixed case. This is presumably a reflection of the fact that the detailed morphology of the evolution also corresponds closely. The difference in final density profile is a consequence of three effects. In the mixed case the gas is in equilibrium within the external potential generated by the dark matter, whereas in the pure fluid case it must find a self-consistent equilibrium. In addition the core gas is heated by two-body effects in the mixed case. Finally in the pure fluid case the core gas experiences weaker shocks.

Overall our results show that in the large cross-section limit collisional dark matter is not a promising candidate for improving the agreement between the predicted structure of CDM halos and published data on galaxies and galaxy clusters. The increased concentration at halo centre will worsen the apparent conflict with dwarf galaxy rotation curves. Furthermore, clusters are predicted to be nearly spherical and galaxy halos to have similar mass in substructure to the collisionless case, although with fewer low mass subhalos. Intermediate cross-sections would lead to collisional behaviour in dense regions and collisionless behaviour in low density regions with a consequent breaking of the approximate scaling between high and low mass halos. The resulting structure may not lie between the two extremes we have simulated. Self-interacting dark matter might then help resolve the problems with halo structure in CDM models, if indeed these problems turn out to be real rather than apparent.

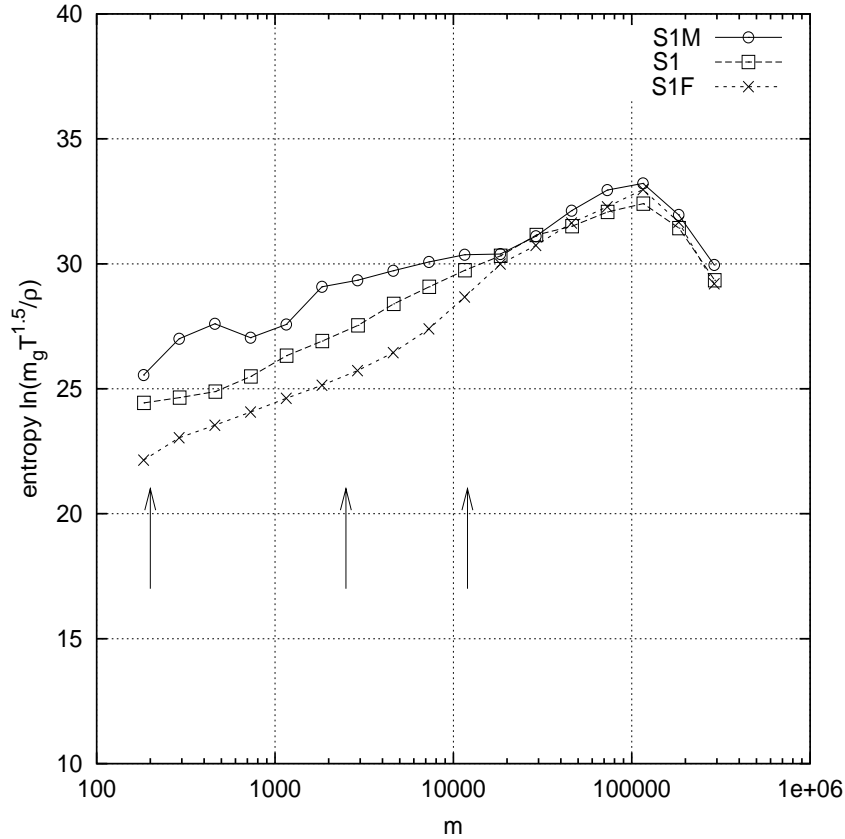


Figure 3.4 We plot Lagrangian specific entropy profiles for the gas fluid simulation (S1F: crosses) and for the mixed simulation (S1M: open circles). In each case $m(s)$ is given in units of the individual gas particle mass, m_g , and the specific entropy of a particle is defined as $\ln(m_g T_g^{1.5}/\rho_g)$. The arrows indicate where the timescale t_{2b} for 2-body heating of the gas by encounters with dark matter particles (see equation (5) of Steinmetz & White (1997)) is 0.1, 1, and 10 times the age of the Universe. For each s we calculate t_{2b} at the radius where the median specific entropy equals s . The dashed line with open squares is an “entropy” profile for S1 calculated by using the SPH kernel to calculate the density and velocity dispersion in the neighbourhood of each particle, and then converting from velocity dispersion to temperature using the standard relation for a perfect monatomic gas.

3.4 WEAKLY SELF-INTERACTING DARK MATTER

3.4.1 Scattering with a finite cross-section

In the previous section we showed that in its “fluid” limit the collisional dark matter model gives a poorer fit to the rotation curves of dwarf galaxies. However, the cross-section range proposed by Spergel & Steinhardt (2000) is the intermediate regime, such that the mean free path of CDM particles is short in halo cores but long in their outer parts.

Mo & Mao (2000) and Firmani et al. (2000) investigated how self-interacting dark matter might effect galaxy rotation curves. Hogan & Dalcanton (2000) considered how the structural properties of halos might scale with their mass. Burkert (2000) and Kochanek & White (2000) studied how collisional relaxation would affect the structure of isolated equilibrium halos, while Moore et al. (2000) and Yoshida et al. (2000a) simulated cluster evolution in a cosmologically realistic context but in the fluid limit (very short mean free path). In this limit collisional dark matter produces more cuspy profiles than collisionless CDM, and so gives even poorer fits to published rotation curves for dwarf galaxies.

We continue exploring how collisions affect the structure of dark halos. We simulate the formation of a massive halo in a Λ CDM universe assuming scattering cross-sections varying over a wide range. The inclusion of the infall and merging which occur when halos are embedded in their proper cosmological context leads to core evolution which is considerably more complex than the expansion followed by collapse seen in the simulations of Burkert(2000) and Kochanek & White(2000). Cross-sections which would significantly modify the core structure of dwarf galaxies produce galaxy cluster cores which are inconsistent with observation.

3.4.2 The N -Body/Monte-Carlo simulations

Our simulations use the parallel tree code GADGET (Springel, Yoshida & White 2001). We study the same cluster as Yoshida et al. (2000a). In order to simulate elastic scattering of CDM particles we adopt the Monte Carlo method introduced by Burkert (2000). We implement this scheme in the following manner. At each time step we evaluate the scattering probability for particle

i ,

$$P = \rho_i \sigma^* V_{\text{rel}} \Delta t, \quad (3.1)$$

where ρ_i is the local density at the particle's position, σ^* is the scattering cross-section per unit mass, $V_{\text{rel}} = |\mathbf{v}_i - \mathbf{v}_{\text{ngb}}|$ is the relative velocity between the particle and its nearest neighbour, and Δt is the time step. This prescription is similar to Burkert's, but uses the relative velocity rather than the absolute velocity of particle i . Kochaneck & White (2000) use a similar scheme but estimate the scattering rate more accurately by looping over a certain number of neighbours. However, the larger smoothing involved in such a procedure can itself introduce difficulties in regions with significant velocity gradients (Meiburg 1986), and so we prefer our simpler scheme which should be unbiased even if somewhat noisier. We choose timesteps small enough to ensure that a particle travels only a minor fraction of its mean free path within Δt . We assume each collision to be elastic, of hard-sphere type, and to have a cross-section independent of velocity. Scattering is assumed isotropic in the centre-of-mass frame, so that relative velocities are randomly reoriented in each collision. We carry out simulations for three values of σ^* differing by factors of ten.

Most of our simulations employ 0.5×10^6 particles in the high resolution region, with a mass per particle $m_p = 0.68 \times 10^{10} h^{-1} M_\odot$. The gravitational softening length is set to $20 h^{-1} \text{kpc}$, which is $\sim 1.4\%$ of the virial radius of the final cluster. We ran one simulation with 5 times better mass resolution and 7 times better spatial resolution to check for numerical convergence. All of our resimulations start from the same initial conditions. The background cosmology is flat with matter density $\Omega_m = 0.3$, cosmological constant $\Omega_\Lambda = 0.7$ and expansion rate $H_0 = 70 \text{ km}^{-1} \text{Mpc}^{-1}$. It has a CDM power spectrum normalised so that $\sigma_8 = 0.9$. The virial mass of the final cluster is $M_{200} = 7.4 \times 10^{14} h^{-1} M_\odot$, determined as the mass within the radius $R_{200} = 1.46 h^{-1} \text{Mpc}$ where the enclosed mean overdensity is 200 times the critical value.

3.4.3 Matter distribution

The large-scale matter distribution in all our simulations looks very similar. Because we start from identical initial conditions, the particle distributions differ only in regions where collisions are important. Figure 3.5 shows that the final cluster is more nearly spherical and has a larger core radius for larger collision cross-section. The quoted axial ratios are determined from the inertia tensors of the matter at densities exceeding 100 times the critical value. Miralda-Escude (2000) argues that the ellipticity of cluster cores, as inferred from gravitational lensing observations, can be used to limit the interaction

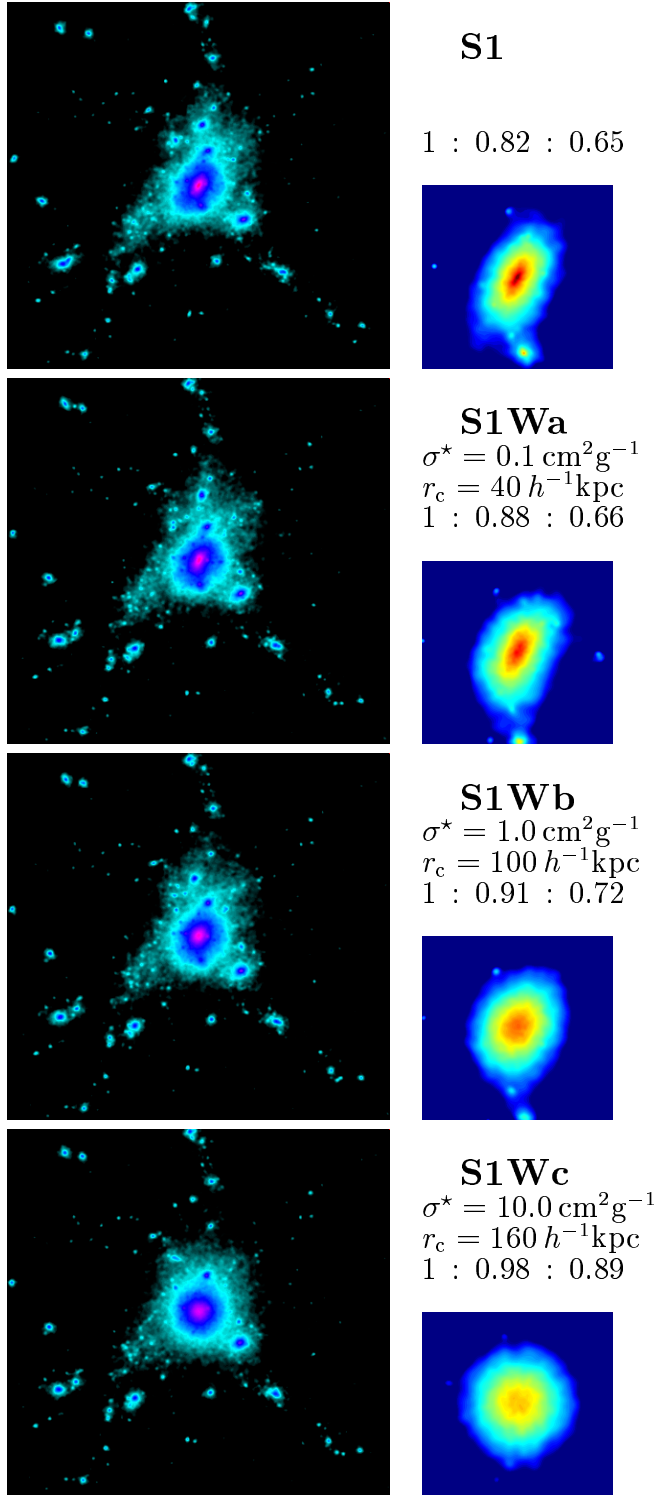


Figure 3.5 Projected mass distributions in a box $15h^{-1}\text{Mpc}$ on a side. The collision cross-sections per unit mass, core radii, axis ratios for each model and small panels showing the central region ($2h^{-1}\text{Mpc}$ on a side, enlarged) in a different colour scale are given to the right of the corresponding image.

cross-section. Among our final clusters, S1W-b and S1W-c are severely constrained by the limits he quotes.

In Figure 3.6 we show density profiles for all of our simulations. Also plotted in the bottom panel is the mean collision number per particle. (We counted collisions for each particle throughout the simulation.) Figure 3.6 clearly shows the presence of a core whose extent depends on the cross-section. For our intermediate cross-section case (S1W-b), we also carried out a higher resolution simulation. The two density profiles agree very well (see Figure 3.6) showing that our simulations have converged numerically on scales larger than the gravitational softening length. The mean collision count at cluster centre is 3 for S1W-a, 8 for S1W-b, and 35 for S1W-c. Thus only a few collisions per particle in a Hubble time suffice to affect the central density profile, and about 10 collisions per particle result in a core with $r_c \geq 100h^{-1}\text{kpc}$. (We define the core radius as the point where the density profile becomes steeper than $\propto r^{-1}$. Core radii by this definition are given on the right of Figure 3.5.)

Unlike an isolated system, our cluster grows through successive mergers. Thus the material in its central region is a mixture of the material from a number of its progenitors. Figure 3.7, a time sequence of density profiles for our S1W-c simulation, shows clearly how merger events interrupt the core evolution and produce low density cores. We let this simulation run beyond the present time to $a=1.72$, where a is the expansion parameter normalised to its present value. During the time interval plotted, the cluster experiences major mergers at $a \sim 0.75$ and $a \sim 1.4$. Each of these events is associated with an increase of the core radius. Subsequent relaxation causes the core to shrink again and the central density to rise. For this relatively large cross-section, relaxation-driven core expansion does not occur within the time interval shown. In contrast to this complex behaviour, the virial mass of the cluster grows quite smoothly, approximately doubling between $a = 0.73$ and $a = 1.72$. Clearly, the core radius of the cluster at $a = 1$ results from an interplay between collisional relaxation driven by particle collisions and violent relaxation caused by mergers.

3.4.4 Substructure abundance

In Figure 3.8 we compare the amount of substructure within R_{200} in our various simulations. We use the SUBFIND algorithm by Springel (1999) to identify subhalos in the final cluster. This identifies gravitationally self-bound sets of particles that are at higher density than the smooth background of cluster material. Local density is defined at each particle's position in a SPH fashion.

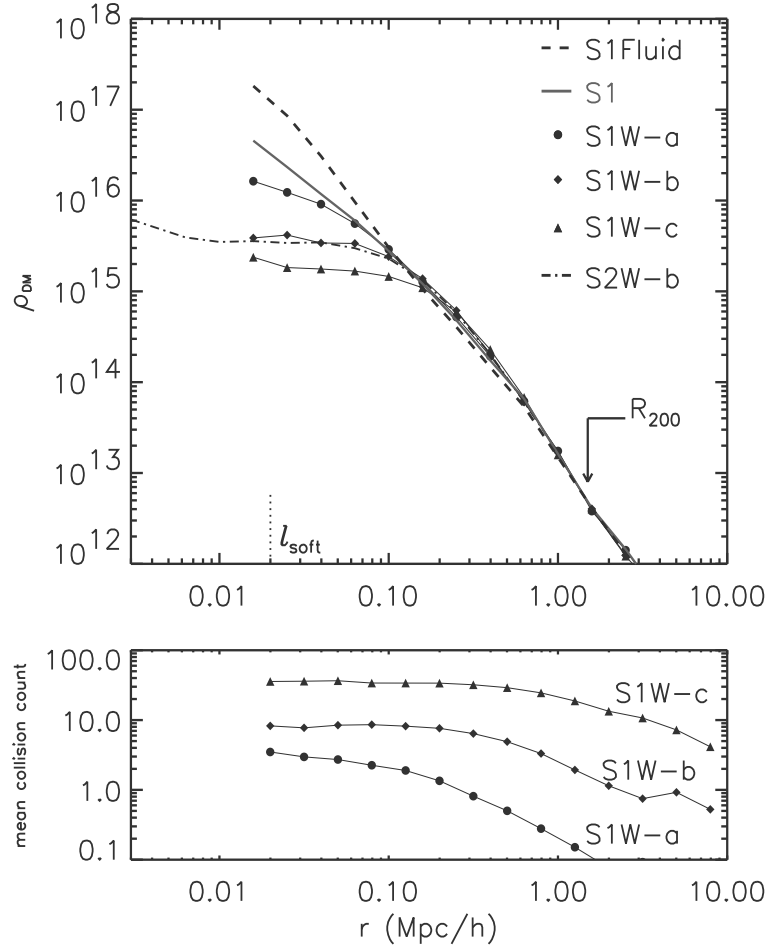


Figure 3.6 Density profiles (top) and mean collision counts per particle (bottom). The vertical dotted line in the top panel indicates the gravitational softening length of our S1 simulations. The virial radius R_{200} of the final cluster is shown as an arrow. The “fluid” dark matter case from Yoshida et al. (2000a) is plotted as the dashed line, while the dash-dotted line represents our higher resolution simulation of the medium cross-section case (S2W-b).

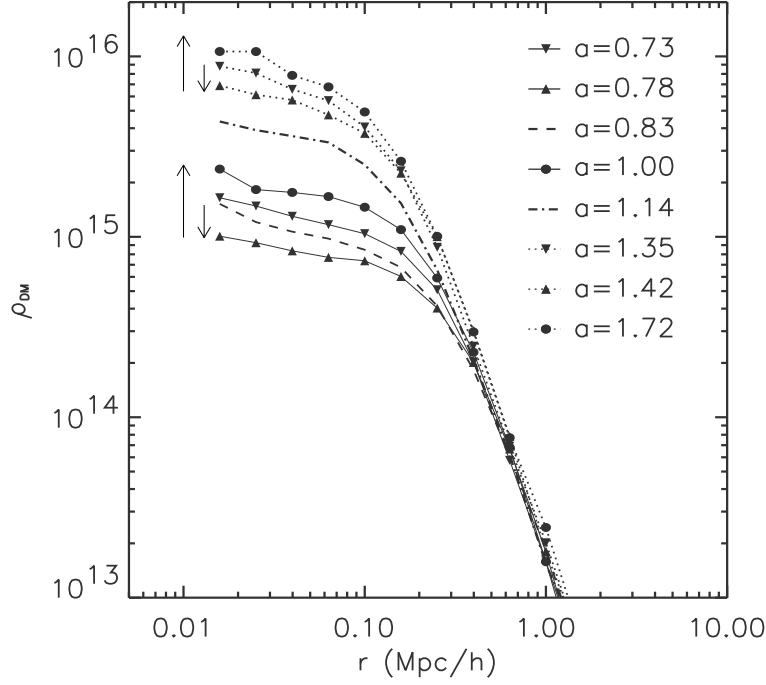


Figure 3.7 We plot the time evolution of the density profile in S1W-c (the largest cross-section case). Time is indicated by the expansion parameter a . The series starts at $a = 0.73$ just before the final merger occurs. After the merger the core settles down again by $a = 0.78$ and then enters a core-collapse phase which is interrupted by another major merger at $a = 1.4$. Note that we let the simulation run beyond the present time $a=1.0$.

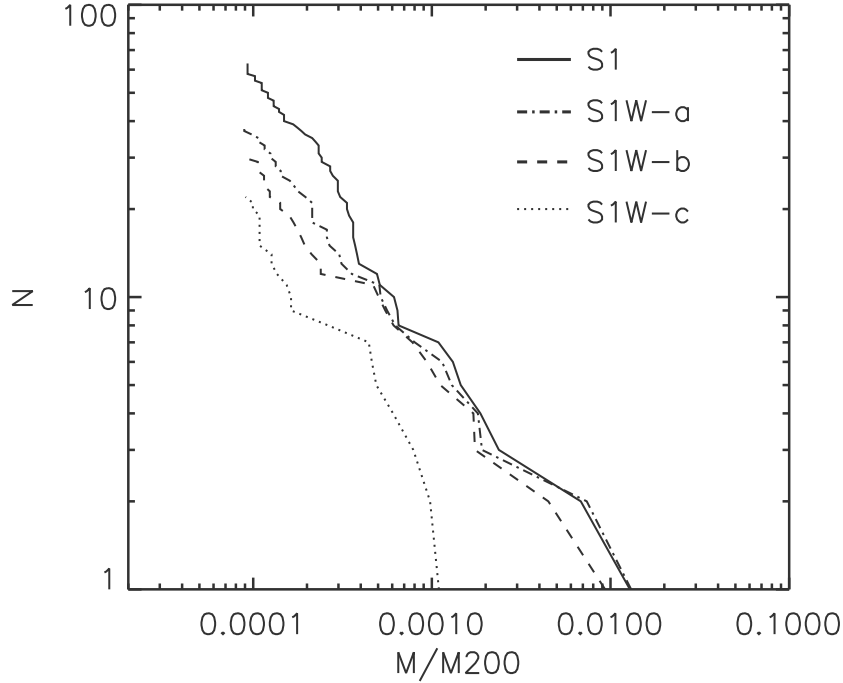


Figure 3.8 The total number of subhalos within R_{200} is plotted as a function of the lower limit to their mass in units of M_{200} . Results are plotted for halos containing 10 or more particles.

Using this procedure we find that 3.7%, 3.6%, 2.5%, and 0.7% of the cluster mass is included in subhalos in S1, S1W-a, S1W-b and S1W-c respectively. Although low mass substructures are somewhat less abundant for larger cross-sections, massive subhalos are *not* substantially disrupted in S1W-a and S1W-b. Many of the massive subhalos are at $\sim 1h^{-1}\text{Mpc}$ from the cluster centre, where particle collisions are rare in these models (see the bottom panel of Figure 3.6). Hence “dark matter evaporation” (Spergel & Steinhardt 2000) is ineffective for them. On the other hand, the massive subhalos in S1W-c are totally disrupted. Infalling halos are rapidly stripped by collisions with “diffuse” cluster dark matter in this case.

3.4.5 Summary and discussion

Our simulations of cluster formation in a ΛCDM universe made of self-interacting dark matter show that collision rates exceeding one or two per particle per Hubble time at cluster centre are sufficient to produce a constant density core.

Observations of strong lensing by clusters require their cores to be dense and small. Thus to fit the cluster Cl0024+1654 Tyson et al. (1998) needed a core radius of $35h^{-1}$ kpc and a central surface density of $7900h M_{\odot}/\text{pc}^2$. Recent HST observations of an unbiased sample of X-ray luminous clusters at $z \sim 0.2$ find thin giant arcs at similar radii (10 to 25 arcsec) in almost all of them (J.-P. Kneib, private communication) showing Cl0024+1654 to be quite typical. We find core radii of this order in our simulations for a cross-section of $0.1 \text{ cm}^2/\text{g}$ (see Figure 3.5).

Predicted collision rates in dwarf galaxy cores are much smaller than in clusters for the core radii usually inferred from rotation curve data. Thus for the archetypal example DDO154, Carignan and Beaulieu (1989) give as best fit parameters a core radius $r_c = 3$ kpc and a central surface density $\Sigma_o = 141 M_{\odot}/\text{pc}^2$. (Note the lack of h dependence because the distance is measured directly.) The central collision rate scales as $\Sigma_o^{1.5}/r_c^{0.5}$, so collisions are inferred to be 60 times less frequent in DDO154 than in Cl0024+1654 (for $h = 0.7$). Since particles in the cluster core have no more than a couple of collisions in a Hubble time (see Figure 3.6) it is difficult to see how collisions could produce the large apparent core in DDO 154. This agrees with the recent results of Davé et al. (2001) who concluded from their own simulations that cross-sections of order $5 \text{ cm}^2/\text{g}$ are needed to produce good agreement with the apparent cores of dwarf galaxies; they found at best marginal consistency for $0.5 \text{ cm}^2/\text{g}$, a value which is still 5 times the upper limit we find to be consistent with cluster data.

A possible solution might seem to be a cross-section about two orders of magnitude larger than in S1W-c. Dwarf galaxy haloes would then look similar to a scaled version of S1W-c, with a core radius of about $4h^{-1}$ kpc for the parameters considered above, while rich clusters would be highly collisional and might have profiles approaching that in our “fluid” simulation. Our earlier work confirmed, however, that such clusters would be almost spherical; such large cross-sections can thus be excluded following Miralda-Escude’s (2000) argument.

A different resolution might be to introduce an interaction law which implies an energy dependent cross-section such that scattering is less effective in high velocity encounters. This would reduce the difference between cluster and dwarf galaxy halos. This idea requires a more detailed physical model for the dark matter, and we do not pursue it further here. We note that $\sigma^* \propto V^{-1}$ is required to make the collision rate at r_s approximately independent of halo mass. Hui (2001) recently studied the particle scattering model which might give rise to a cross section that scales inversely with velocity, and concluded

that such an interaction law will be likely only for a limited range of V .

Another loophole might be for the cores of clusters to contain large amounts of baryonic dark matter, perhaps deposited by cooling flows. The cooling rates inferred from X-ray data appear too small for this to be viable (see, e.g. Peres et al. 1998).

In summary our results suggest that collisional dark matter cannot produce core radii in dwarf galaxy halos as large as those inferred from rotation curve observations without simultaneously producing cluster cores which are too large and too round to be consistent with gravitational lensing data.

3.5 LENSED ARCS AS A CONSTRAINT ON THE SCATTERING CROSS-SECTION OF DARK MATTER

Although the dark matter in galaxy clusters cannot be seen directly, a very direct way to measure its properties is offered by the phenomenon of gravitational lensing. The images of distant galaxies lying far behind the cluster are gravitationally distorted into giant arcs as the light passes through the cluster on its journey to our telescopes. The shapes and positions of these arcs provide a detailed picture of how matter is distributed near the cluster centre. It is natural to ask how self-interacting dark matter would affect the strong gravitational properties of galaxy clusters.

In the self-interacting dark matter model, the density profiles of rich clusters would show cores similar to that seen in our model S1W-c, i.e. $r_c \sim 150h^{-1}\text{kpc}$. Such large cores are not consistent with the mass distributions inferred from the presence of giant arcs in clusters. Analyses by a number of authors (Kneib et al. 1993; Luppino et al. 1993; Bonnet et al. 1994; Tyson et al. 1998) suggests core radii in the range $35\text{--}100h^{-1}\text{kpc}$, typically a factor of two below the value we estimate. These upper limits are actually conservative, since the observed thinness of giant arcs requires substantially smaller cores (Miralda-Escude 1995).

Detailed modelling of gravitational lensing was done by Meneghetti and Yoshida et al. (2001) using our simulated clusters. They carry out ray tracing through five high resolution simulations of a galaxy cluster to study how its

ability to produce giant gravitationally lensed arcs is influenced by the collision cross-section of the dark matter. In three cases typical dark matter particles in the cluster core undergo between 1 and 100 collisions per Hubble time; two more simulations explore the long (“collisionless”) and short (“fluid”) mean free path limits. Meneghetti et al. studied the size and shape distributions of arcs and compute the cross-section for producing giant arcs of various sizes. Figure 3.9 shows distorted source image produced by their ray-tracing simulations. It is clearly seen that the dark matter self-interaction substantially reduces the number of strongly lensed images. Even a few collisions per particle modify the core structure enough to destroy the cluster’s ability to produce long, thin arcs. For larger collision frequencies the cluster must be scaled up to unrealistically large masses before it regains the ability to produce giant arcs. None of our models with self-interacting dark matter (except the “fluid” limit) is able to produce radial arcs; even the case with the smallest scattering cross-section must be scaled to the upper limit of observed cluster masses before it produces radial arcs. Apparently the elastic collision cross-section of dark matter in clusters must be very small, below $0.1 \text{ cm}^2\text{g}^{-1}$, to be compatible with the observed ability of clusters to produce both radial arcs and giant arcs. Recent studies by Meneghetti (2001, private communication) confirmed that even if there are giant cD galaxies in the cluster centre, it is difficult to recover the lensing ability to the observed level. The study essentially constrains the value of the scattering cross section of dark matter, to be below $0.1 \text{ cm}^2\text{g}^{-1}$. We note that with cross-sections much smaller than $0.1 \text{ cm}^2\text{g}^{-1}$, the system is essentially collisionless, as dark matter particles will not experience a collision in a Hubble time. Therefore, the result indeed favours the *collisionless* cold dark matter rather than collisional.

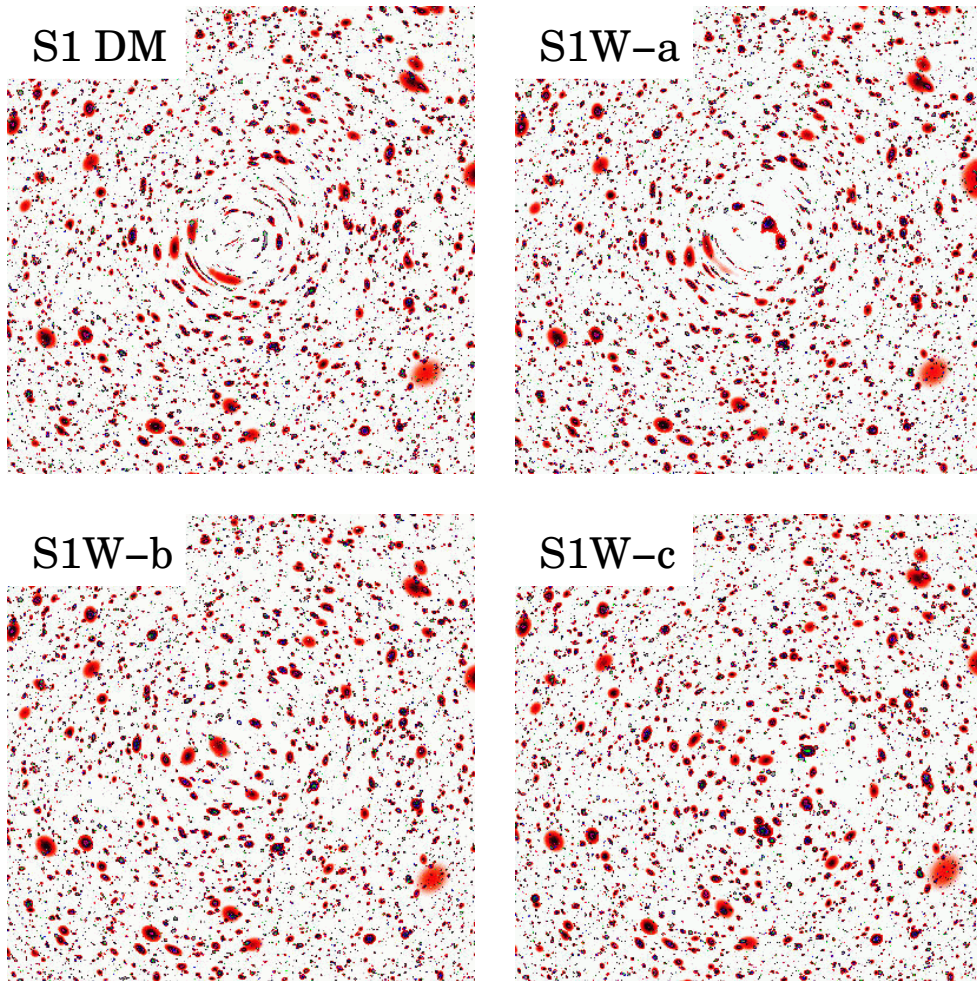


Figure 3.9 Distorted source images produced by ray-tracing simulations of gravitational lensing using our S1 clusters. The regions shown are $1.5h^{-1}\text{Mpc}$ on a side around the main cluster. We put the clusters at redshift 0.28 and distribute the sources (assumed to be elliptical) in redshift space in such as to reproduce the redshift distribution of the galaxies in the *Hubble Deep Field North* and *South*. (Pictures kindly provided by Massimo Meneghetti.)

CHAPTER 4

The Sunyaev-Zel'dovich effect

4.1 THEORY

Compton scattering of cosmic microwave background (CMB) photons by electrons in the hot intergalactic gas in clusters of galaxies causes a spectral distortion of the CMB in the direction of such clusters. The physical process, referred to as the Sunyaev-Zel'dovich effect (Sunyaev-Zel'dovich 1980a), imprints a redshift-independent signature in the CMB, and so the effect serves as a unique probe of structure formation in the Universe on the largest scales.

It was proposed that, from measurements of the effect, together with measurements of thermal X-ray emission, the value of the Hubble constant (Cavaliere et al. 1977, Gunn 1978, Silk & White 1978), and peculiar velocities of clusters (Sunyaev & Zel'dovich 1980b) can be determined. The Sunyaev-Zel'dovich effect is also a dominant source of secondary CMB anisotropies on arcminute scales, and therefore it is important to know the spatial distribution of the effect. So far the Sunyaev-Zel'dovich effect has been detected for a few dozen clusters. Considerable progress will be made by future ground-based experiments such as ALMA, and by the satellite mission *Planck*. The *Planck* satellite will detect the thermal Sunyaev-Zel'dovich effect for tens of thousands(!) of galaxy clusters over the whole sky.

4.1.1 The thermal Sunyaev-Zel'dovich effect

Data obtained by X-ray satellites such as *ROSAT*, *ASCA* and their predecessors show that rich clusters of galaxies contain a large amount of hot ($T \sim 10^8\text{K}$) plasma. While emission due to bremsstrahlung by the hot plasma is observed at X-ray frequencies, Compton scattering of the CMB photons by free electrons leads to many important features. Conservation of the net photon number in the scattering implies that there is a systematic shift in the energy distribution from the Rayleigh-Jeans to the Wien side. The rate of change of the photon occupation number \bar{n} due to Compton scattering by isotropic, non-relativistic, Maxwellian electron gas is described by the Kompaneets equation (Kompaneets 1957)

$$\frac{\partial \bar{n}}{\partial t} = \frac{kT_o}{m_e c} \frac{\sigma_T n_e}{x^2} \frac{\partial}{\partial x} \left[x^4 \left(\frac{T_e}{T_o} \frac{\partial \bar{n}}{\partial x} + \bar{n} + \bar{n}^2 \right) \right], \quad (4.1)$$

where σ_T is the Thomson cross-section, since the Compton scattering we consider here is in the Thomson limit $h\nu/kT \rightarrow 0$. The electron number density and temperature are denoted n_e and T_e , and T_o is the radiation temperature. Sunyaev & Zel'dovich originally used this non-relativistic treatment, but the full calculation of the relativistic kinetic equation is necessary for the change of the photon distribution at high frequencies (see, e.g. Raphaeli 1995). Nevertheless the Kompaneets-based treatment of Sunyaev & Zel'dovich yields a sufficiently adequate description at low frequencies.

In equation (4.1), the first term of the right-hand side is much larger than the second and third terms when $T_e \gg T_o$. The equation is then greatly simplified

$$\frac{\partial \bar{n}}{\partial t} = \frac{kT_e \sigma_T n_e}{m_e c} x^4 \left(\frac{\partial \bar{n}}{\partial x} \right). \quad (4.2)$$

By substituting the expression for the occupation number of a purely Planckian radiation field (we assume that the incident radiation is only weakly affected by scattering), we obtain an approximate solution for equation (4.2):

$$\bar{n}_p(x) = \frac{1}{e^x - 1}. \quad (4.3)$$

Integrating along the line-of-sight through the cluster, we obtain the change of spectral intensity $I = 2(kT_o)^3/(hc)^2 x^3 \bar{n}$:

$$\Delta I = 2 \frac{(kT_o)^3}{(hc)^2} y g(x). \quad (4.4)$$

The *spectral* character of this thermal Sunyaev-Zel'dovich effect is contained in the function

$$g(x) = \frac{x^4 e^x}{(e^x - 1)^2} \left[\frac{x(e^x + 1)}{e^x - 1} - 4 \right], \quad (4.5)$$

which becomes zero at the crossover frequency $x_o = 3.83$, or $\nu_o = 217$ GHz for $T_o = 2.726$ K (Mather et al. 1994). This spectral feature of the thermal effect makes it possible to disentangle it from the kinematic effect discussed below. The Comptonisation parameter, which describes the *spatial* dependence of the effect, is given by

$$y = \left(\frac{k}{m_e c^2} \right) \int \sigma_T n_e T_e dl, \quad (4.6)$$

where the integration is carried out along a line-of-sight through the cluster.

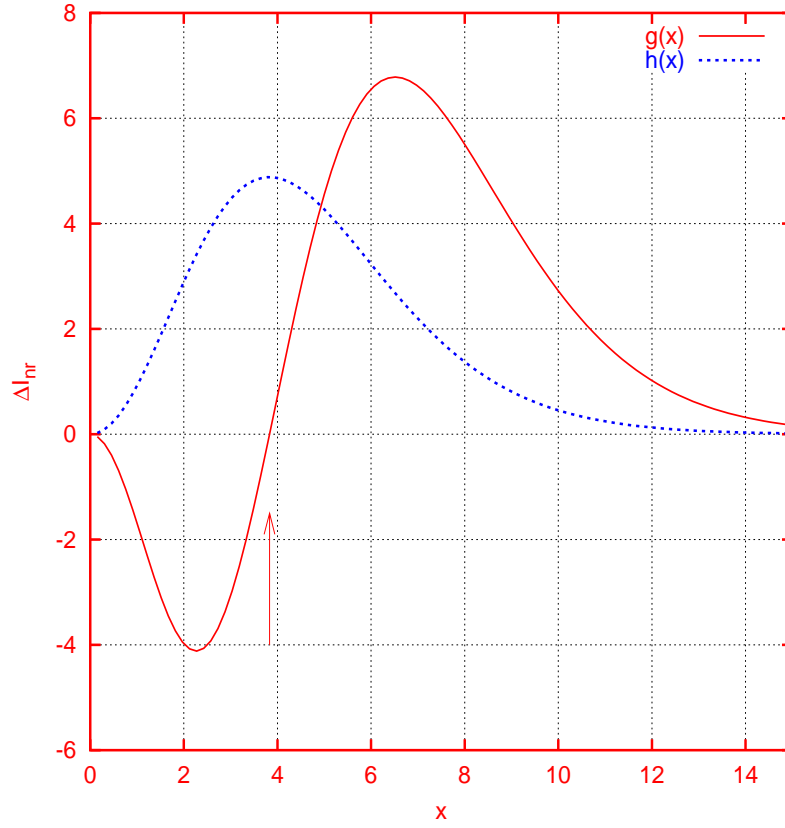


Figure 4.1 The spectral dependence of the non-relativistic thermal intensity change, $g(x)$, and that of the kinematic effect, $h(x)$, as functions of the dimensionless frequency $x = h\nu/kT$. The arrow indicates the cross-over frequency $x_o = 3.83$.

The resulting change in brightness temperature is

$$\frac{\Delta T}{T_o} = \left[\frac{x(e^x + 1)}{e^x - 1} - 4 \right] y. \quad (4.7)$$

At low frequencies (in the Rayleigh-Jeans limit $x \ll 1$), the amplitude is just $-2y$, so the effect depends on the line-of-sight integral of the electron pressure alone. Figure 4.1 show the spectral feature of the effect.

4.1.2 The kinematic Sunyaev-Zel'dovich effect

When the hot plasma causing the thermal Sunyaev-Zel'dovich effect is moving relative to the CMB rest frame, another effect, termed the *kinematic effect*, is caused by the bulk motion of the plasma. In the reference frame of the scattering medium the microwave background radiation appears anisotropic, and the effect of the inverse-Compton scattering is to re-isotropise the radiation. Back in the rest frame of the observer, the resulting radiation field is not isotropic, but shows a dipole structure towards the direction of the bulk peculiar velocity of the plasma. An interesting aspect of the kinematic effect is that it provides a method to measure the line-of-sight component of the peculiar velocity.

Note that the distinction between the thermal and kinematic effects is somewhat arbitrary since both effects result from electron motions. Phillips (1995) showed that the two effects are separable when the bulk velocity is much smaller than the thermal velocities of the electrons. On these assumptions, the additional kinetic intensity change is

$$\Delta I_k = -2 \frac{(kT_o)^3}{(hc)^2} h(x) \frac{V_r}{c} \tau, \quad (4.8)$$

where the spectral form is given by

$$h(x) = \frac{x^4 e^x}{(e^x - 1)^2}. \quad (4.9)$$

We have expressed the line-of-sight peculiar velocity of the cluster as V_r and defined the optical depth as

$$\tau = \sigma_T \int n_e dl. \quad (4.10)$$

The consequent change in the brightness temperature is

$$\frac{\Delta T_k}{T_o} = -\frac{V_r}{c} \tau. \quad (4.11)$$

4.2 NON-GAUSSIAN CMB TEMPERATURE FLUCTUATIONS FROM PECULIAR VELOCITIES OF CLUSTERS

4.2.1 Introduction

Coherent bulk motions of the intracluster plasma cause secondary CMB temperature fluctuations, as described in the previous section. Recent cosmological simulations suggest that the distribution of these temperature fluctuations will be quite non-Gaussian, and that, because of the amplitude of the effect relative to that of the primordial fluctuations (*rms* $\Delta T/T \approx 4 \times 10^{-5}$), the best hope of detecting the effect is in the tails of the distribution (da Silva et al. 2000, Seljak, Burwell & Pen 2001). In this section we study the distribution of fluctuations in pixels in CMB maps which are peaks. Peaks can be easily located in a robust manner by finding the local maxima and minima in two-dimensional maps. We show that the distribution of these peak heights is expected to be highly non-Gaussian, and that the exact shape of the distribution can be computed if the spectrum of initial density fluctuations is specified. We develop an analytic model to predict the distribution and compare the result with estimates of the peak height distribution from large N -body simulations. We show that our model quite accurately predicts the distribution for the given initial power spectrum. This in turn implies that observations of the peaks will allow one to place constraints on the initial density fluctuations. We restrict our attention to the simplest case in which signals come from a single redshift, chosen to be close to the present epoch, when nonlinear structures have already grown. Even when a range of redshifts contribute, our finding will remain unaltered. The final distribution of fluctuations should be non-Gaussian and related to the initial density fluctuation distribution.

4.2.2 The simulations

The simulation we use was recently carried out by the Virgo Consortium. It employs 512^3 CDM particles in a cosmological box of $480h^{-1}\text{Mpc}$ on a side. The cosmological model is flat with matter density $\Omega_0 = 0.3$, cosmological constant $\Omega_\Lambda = 0.7$ and expansion rate at the present time $H_0 = 70\text{km}^{-1}\text{Mpc}^{-1}$. It has a CDM initial power spectrum computed by CMBFAST (Seljak & Zaldarriaga 1996), normalized to the present abundance of galaxy clusters so that

$\sigma_8=0.9$. We emphasize that, since the kinematic Sunyaev-Zel'dovich effect arises from the peculiar velocities of clusters, a large simulation box such as ours is essential for studying this effect: smaller boxes miss a significant fraction of the power which generates velocities, so they are liable to underestimate the magnitude of the effect (see Sheth & Diaferio 2001 for more discussion on the finite box size effect). In addition, our large simulation contains a sufficiently large number of massive halos which smaller simulation boxes are likely to under- or over-estimate. The proper population of massive halos is essential for studying the distribution of the thermal effect (e.g. Refregier & Teyssier 2000).

From the simulation outputs we create two-dimensional maps of the thermal Sunyaev-Zel'dovich effect, the kinematic Sunyaev-Zel'dovich effect, and the Thomson optical depth, following the procedure outlined in Diaferio, Sunyaev, & Nusser (2000). We note slight differences between our procedure and that in Diaferio et al. We compute the local density and the velocity dispersion (to be converted into gas temperature for a standard choice of β parameter) in a Smoothed Particle Hydrodynamics fashion by looping over 40 neighbouring particles. We project the simulation box on a fine 2400^2 grid in a random direction; thus, each pixel in the grid is $L = 200h^{-1}\text{kpc}$ on a side. This pixel scale L is about an order of magnitude larger than the $30h^{-1}\text{kpc}$ spatial resolution of the simulation. Figure 4.2 shows the simulated tSZ and kSZ maps. The entire box (of $480h^{-1}\text{Mpc}$ on a side) is shown in the figures. Notice the large scale filament structures seen in the kSZ map. Nonlinear structures in super cluster regions are clearly seen as nearby positive and negative peaks in the kSZ effect.

4.2.3 Kinematic effect

The optical depth along a line-of-sight dl is defined by

$$\tau = \sigma_{\text{T}} \int n_e(l) dl \approx \frac{\sigma_{\text{T}}}{m_{\text{proton}}} \frac{\Omega_{\text{b}}}{\Omega_0} \rho_{\text{crit}} \int dl \frac{\rho_{\text{dm}}(l)}{\rho_{\text{crit}}}, \quad (4.12)$$

where σ_{T} is the Thomson scattering cross-section, $n_e(l)$ is the density of electrons along the line of sight at l , $\rho_{\text{dm}}(l)$ is the mass density along the line of sight at l , $\rho_{\text{crit}}\Omega_0$ is the average mass density of the background, and Ω_{b} denotes the abundance of baryons. Throughout this chapter we use as a fiducial value $\Omega_{\text{b}} = 0.0125/h^2$. The second equality shows our assumption to relate the properties of the dark matter particles to those of baryons: baryons traces the dark matter.

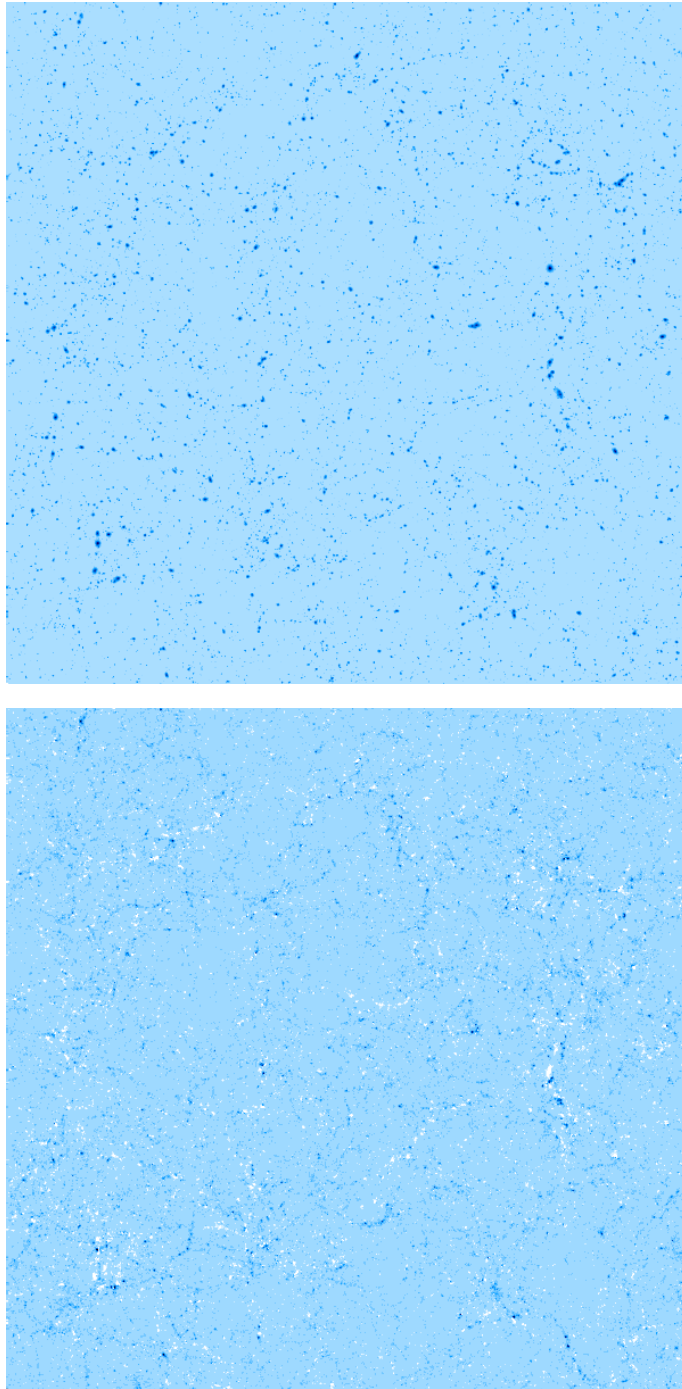


Figure 4.2 Simulated map of the tSZ decrements in the simulation box at $z=0$ (top), and of the kSZ effect (bottom). The comoving resolution is $0.2h^{-1}\text{Mpc}$. Black spots correspond to negative fluctuations, whereas the white spots in the bottom panel correspond to positive fluctuations. The color scales are such that the temperature decrements $\Delta T/T_{\text{CMB}}$ are logarithmically scaled from grey to black in the top panel, while the temperature fluctuations are linearly scaled between white ($+3 \times 10^{-5}$) and black (-3×10^5) in the bottom panel.

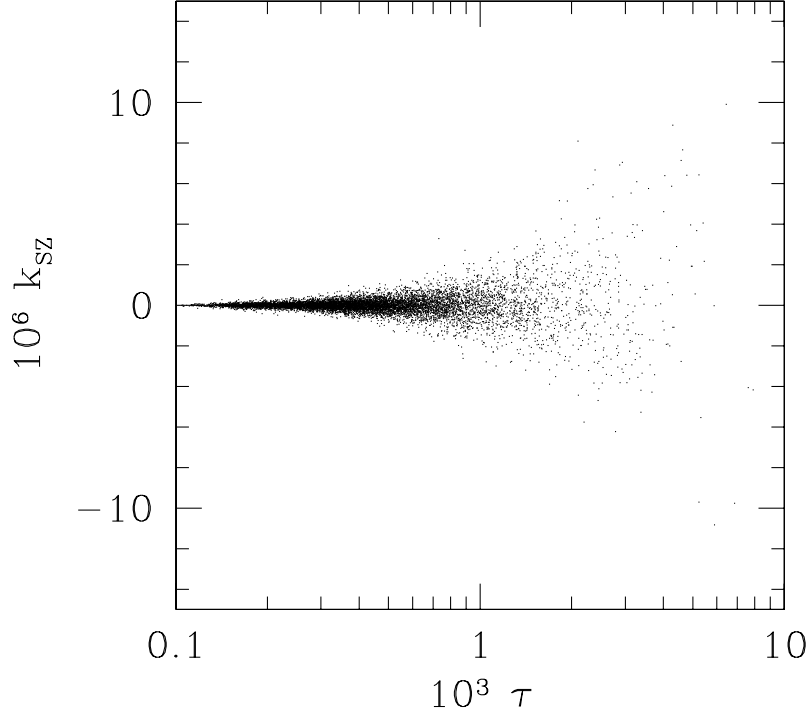


Figure 4.3 Scatter plot showing the height of a k_{SZ} peak as a function of optical depth τ .

The temperature fluctuation due to the kinematic Sunyaev-Zel'dovich effect k_{SZ} is then defined by

$$k_{\text{SZ}} = \frac{\Delta T}{T} = \frac{\Omega_b}{\Omega_0} \frac{\sigma_{\text{T}}}{m_{\text{proton}}} \rho_{\text{crit}} \int dl \frac{\rho_{\text{dm}}(l)}{\rho_{\text{crit}}} \frac{v(l)}{c_{\text{light}}}, \quad (4.13)$$

where $v(l)/c_{\text{light}}$ is the bulk velocity along the line of sight at l , divided by the speed of light. Notice that if one thinks of the optical depth as a measure of the density, then the kinematic effect is a measure of the momentum. In the following, we first describe what is found in simulations of the kinematic effect, and then we present a model which provides a good fit to the simulations.

Figure 4.3 shows the heights of the peaks in the kinematic effect, k_{SZ} , as

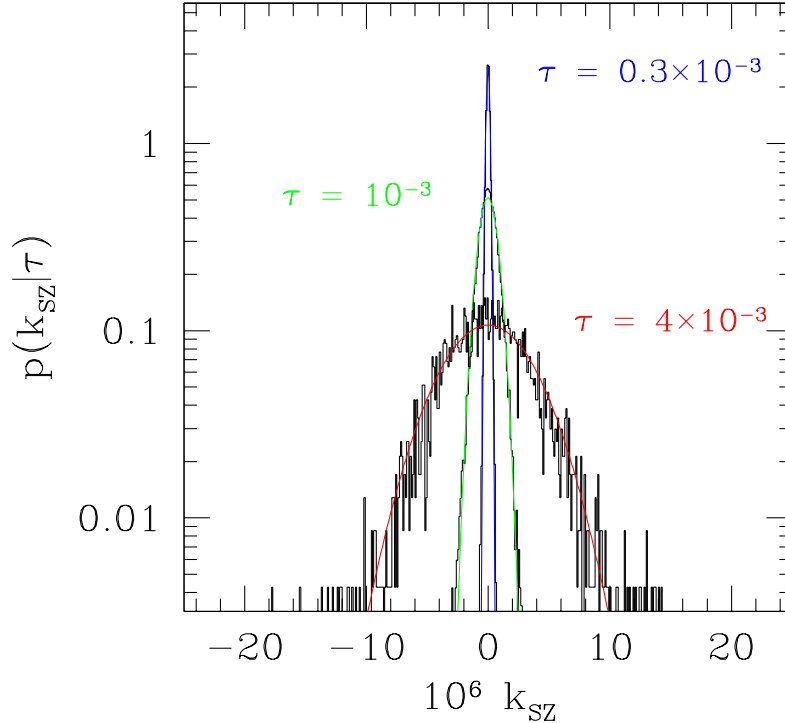


Figure 4.4 Distribution of k_{SZ} peak heights at fixed optical depth. Curves show Gaussians with the same rms.

a function of optical depth (see also Figure 3 in Diaferio et al. 2000). It was constructed following the procedures Diaferio et al. outlined; the only difference is that here we use a ~ 40 times larger simulation described in the previous section hence it provides better statistics. Notice that the mean k_{SZ} peak height is zero for all τ , but the scatter around zero increases as τ increases. In fact, at fixed τ , the distribution around the mean is well fit by a Gaussian as shown in Figure 4.4. Further, the width of the Gaussian increases linearly with τ as is shown in Figure 4.5.

The *total* distribution of the peak heights is obtained by integrating over all τ :

$$p(k_{SZ}) = \int d\tau p(\tau) G(k_{SZ}|\tau), \quad (4.14)$$

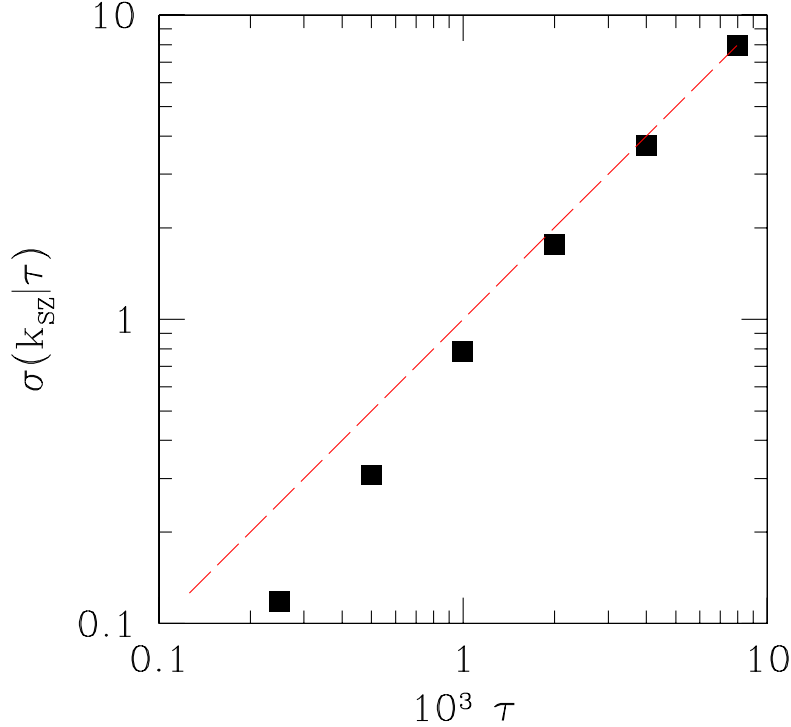


Figure 4.5 The rms value of k_{SZ} at fixed τ as a function of τ . Dashed line shows the scaling expected if $\sigma(k_{SZ}|\tau)$ increases linearly with optical depth.

where G denotes the Gaussian distribution of k_{SZ} at fixed τ . Because the width of the Gaussian depends on τ , the resulting $p(k_{SZ})$ is a summation of Gaussians of different dispersions. This is the fundamental reason why the distribution $p(k_{SZ})$ is expected to be highly non-Gaussian. (Note that a summation of two Gaussian functions is a Gaussian only if they have the same dispersions.) The histogram in Figure 4.6 shows the total distribution. It has a central cusp and indeed looks quite non-Gaussian.

In what follows, we will describe why the distribution of k_{SZ} at fixed τ is Gaussian, and why the dispersion $\sigma(k_{SZ}|\tau)$ is approximately proportional to τ . We will then provide a model for $p(\tau)$. When inserted into the expression above, these ingredients allow us to model the distribution of k_{SZ} —this

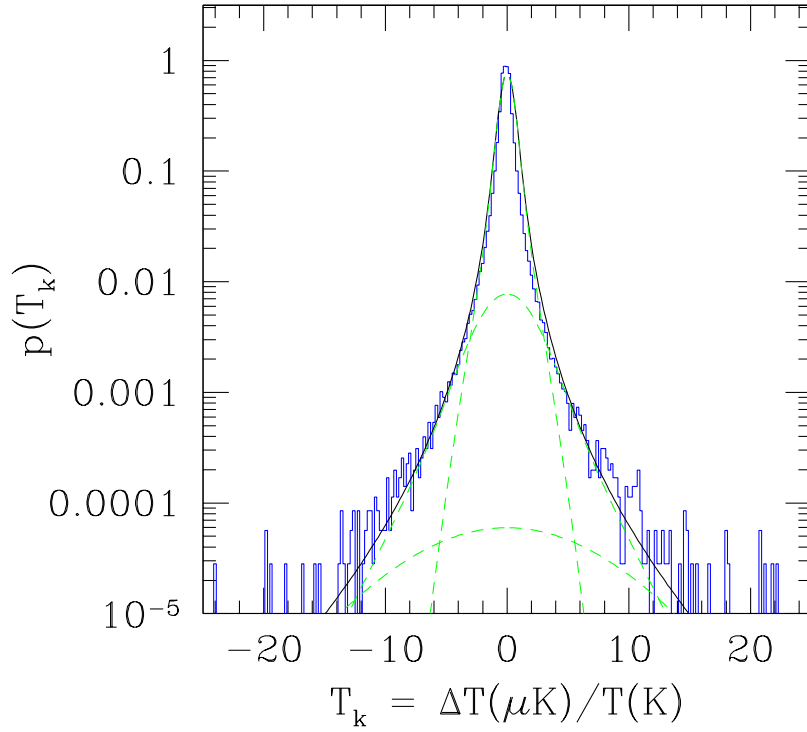


Figure 4.6 Distribution of k_{SZ} fluctuations from sources at $z = 0$. Histogram shows the measurements in the N -body simulation, solid curve shows what our model predicts (eq. 4.26 below). Dashed curves show the predicted contribution to the solid curve from halos with mass in the range $10^{12} - 10^{13}$ (narrowest distribution), $10^{13} - 10^{14}$, and $10^{14} - 10^{15} M_{\odot}/h$ (broadest distribution with lowest peak).

produces the solid curve shown in Figure 4.6.

4.2.4 Analytic model

Let us consider a case where a line-of-sight (or a pixel in the map) will contain or lie within only one dark halo. There may be contributions to the integral from regions which do not contain halos. However, the density within a halo is on the order of two hundred times ρ_{crit} . Therefore, provided that the motions of halos are not significantly smaller than the motions in less dense regions, and provided that the velocities are not correlated over scales which are on the order of two hundred times larger than the size of a typical halo, pixels associated with halos contribute much more to the line of sight integral than do the much less dense pixels which are not associated with halos. In this respect, our analysis is similar to that in Cole & Kaiser (1988) and Peebles & Juszkiewicz (1998). Because the virial motions within halos are random, the component of $v(l)$ which is due to the virial motions will fluctuate around zero. The result of integrating over all l is that these internal virial motions will cancel out, and only the bulk peculiar velocities of the halos contribute to the line of sight integration.

For a high resolution map, whose pixels are sufficiently small, it is unlikely that a given line of sight will contain more than one halo *center*. Moreover, the halos have central density cusps (e.g. Navarro, Frenk & White 1997). Therefore, peaks in the k_{SZ} distribution occur in those pixels which contain the density cusps. We assume that there is one density cusp per halo and ignore the possible contribution from subhalos. We discuss the contributions from the halos' substructure in section 4.2.7. There it will be shown that such contributions are indeed small. We replace the integral over the line of sight by the value the integrand has at the position of the peak:

$$k_{\text{SZ}} = \left(\frac{v}{c_{\text{light}}} \right) \frac{\Omega_b}{\Omega_0} \frac{\sigma_{\text{T}}}{m_{\text{proton}}} \rho_{\text{halo}} R_{\text{halo}} = (v/c_{\text{light}}) \tau, \quad (4.15)$$

where v is the bulk velocity of the halo, ρ_{halo} and R_{halo} are intended to denote the average density contributed by the halo over the integration range along the line of sight, R_{halo} , it occupied. The final expression defines τ , the optical depth of the pixel containing the central density cusp of the halo. To model the distribution of k_{SZ} , we need to model how the optical depth τ and the velocity v depend on halo mass m . We incorporate the pixel width in the following manner. The optical depth in a square pixel of side L which contains the central density cusp of a halo of mass m and central concentration parameter

c , can be estimated by setting

$$\tau(m) = 2 \int_0^W \frac{dw}{W} \frac{w}{W} \tau(w|c, m), \quad (4.16)$$

where $W = [L/r_s(m)]/\sqrt{\pi}$, and

$$\begin{aligned} \tau(w|c, m) &= \frac{\sigma_{\text{T}}}{m_{\text{proton}}} \frac{\Omega_{\text{b}}}{\Omega_0} r_s \int dl \rho(x|c, m) \\ &= \frac{\sigma_{\text{T}}}{m_{\text{proton}}} \frac{\Omega_{\text{b}}}{\Omega_0} r_s(m) \rho_s(m) \frac{2[1 - h(w)]}{w^2 - 1}. \end{aligned} \quad (4.17)$$

This expression for $\tau(w|m)$ is obtained by projecting a NFW density profile along the line-of-sight (Cramphorn 2001):

$$\begin{aligned} \rho(x|c, m) &= \frac{\rho_s}{x(1+x)^2}, \quad \text{where } x^2 = l^2 + w^2, \\ \rho_s(m) &= \rho_{\text{crit}} \delta_c(m) \\ &= \rho_{\text{crit}} \frac{\Delta_{\text{nl}}}{3} \frac{c^3(m)}{\ln[1+c(m)] - c(m)/[1+c(m)]}, \\ r_s(m) &= \frac{r_{\text{vir}}}{c(m)} = \frac{1}{c(m)} \left(\frac{3m}{4\pi\rho_{\text{crit}}\Delta_{\text{nl}}} \right)^{1/3}, \\ c(m) &= 12 \left(\frac{m}{m_*} \right)^{-0.13}, \\ h(w) &= \frac{\text{arccosh}(1/w)}{\sqrt{1-w^2}} \quad \text{if } w \leq 1 \\ &= \frac{\arccos(1/w)}{\sqrt{w^2-1}} \quad \text{if } w > 1, \end{aligned} \quad (4.18)$$

and $\Delta_{\text{nl}} \approx 100$ for the Λ CDM model we are considering here. The quantity $c(m)$ is often called the concentration parameter of the halo, defined as the ratio r_{vir}/r_s . Massive halos have small values of c , i.e., less centrally concentrated (Navarro, Frenk & White 1997). We use the parametrization of this mass dependence given by Bullock et al. (2001). The final averaging over the circular beam of radius W can also be done analytically:

$$\tau(m) = \frac{\sigma_{\text{T}}}{m_{\text{proton}}} \frac{\Omega_{\text{b}}}{\Omega_0} r_s(m) \rho_s(m) \frac{2}{W^2} \left[\ln(W^2/4) + 2h(W) \right]. \quad (4.19)$$

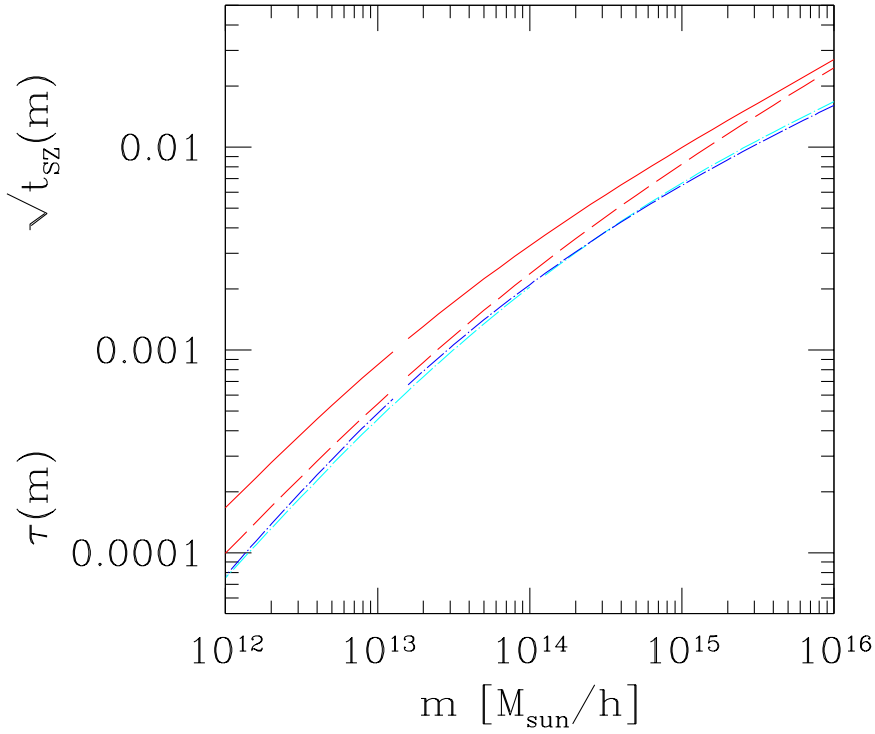


Figure 4.7 Optical depth τ and thermal SZ effect t_{SZ} peak heights as functions of halo mass m . Lower dot-dashed curves show $\tau(m)$ for profiles of the form given by Hernquist (1990) and by Navarro et al. (1997). Upper solid and dashed curves show $\sqrt{|t_{SZ}|}$ for Hernquist profiles when the circular velocity and the isotropic dispersion, respectively, are used to estimate the temperature.

One of the dot-dashed curves in Figure 4.7 shows the optical depth given by equation (4.19). Notice that, for low mass halos, $L \gg r_s$, and the term in square brackets in equation (4.19) tends to be a constant. In this limit $\tau \propto r_s^3 \rho_s$ (recall that $W^2 \propto r_s^{-2}$), which means that the optical depth is approximately proportional to m . This is the case when the entire halo fits in a cell. The more massive halos have larger scale radii and so they also have larger optical depths; at large m , $\tau(m)$ is approximately proportional to $m^{2/3}$ (see Figure 4.7). We emphasize that, for our purposes in this section, an important point is that the optical depth is a monotonically increasing function of halo mass.

To show that this conclusion is not sensitive to the details of the density profile in the outer regions of halos, the other dot-dashed curve in Figure 4.7 shows the optical depth associated with the profile shape presented in Hernquist (1990). The appendix to this section shows that the relevant integrals for this profile can all be computed analytically. We will describe the other two curves in Figure 4.7 in the next section. The Hernquist profile scales as $1/x/(1+x)^3$, while the NFW profile scales as $1/x/(1+x)^2$. Although the Hernquist profile falls more steeply at large radii, it has the same small scale slope as the NFW profile. The fact that the optical depths for these two parametrizations of halo profile shapes are so similar implies that most of the contribution to the optical depth comes from the inner parts of the halos, where the profiles themselves are similar.

We now describe our model for the halo peculiar velocities based on linear theory. Sheth & Diaferio (2001) showed that, if the initial density fluctuation field was Gaussian, then to a good approximation, the peculiar velocities of dark matter halos are drawn from a Maxwellian distribution, even at late times. In addition, they showed that the rms velocity can be computed from linear theory, and that it has a weak dependence on halo mass. In the linear theory of gravitational instability, the peculiar velocity of a mass element grows with cosmic scale factor a as

$$v \propto a\dot{D}, \quad (4.20)$$

where $D(t)$ is the growth factor for linear density perturbation. (see, for example, Lahav et al. 1991 for explicit expressions for D and \dot{D} .)

Bardeen, Bond, Kaiser, & Szalay (1986, hereafter BBKS) developed a peak model where nonlinear objects like galaxy clusters are associated with peaks in the *smoothed* initial density field. For a Gaussian random field, the smoothed initial peculiar velocity field is isotropic and Gaussian with a three-dimensional dispersion

$$\sigma_v(R) = H\Omega^{0.6}\sigma_{-1}(R), \quad (4.21)$$

where R is the smoothing scale related to the mass scale as $M = 4\pi\bar{\rho}R^3/3$, and σ_j are the spectral moments defined by

$$\sigma_j^2(R) = \frac{1}{2\pi^2} \int P(k)W^2(kR)k^{2j+2}dk, \quad (4.22)$$

for the density fluctuation power spectrum $P(k)$ and the window function W . BBKS showed that the rms peculiar velocity at peaks of the smoothed density field differs systematically from σ_v but given by

$$\sigma_p(R) = \sigma_v(R)\sqrt{1 - \sigma_0^4/\sigma_1^2\sigma_{-1}^2}. \quad (4.23)$$

Following Sheth & Diaferio (2001) we parametrize the rms peculiar velocity for the Λ CDM model we are considering,

$$V_{1d}(m) = \frac{430/\sqrt{3}}{1 + (m/2487)^{0.284}} \text{ km/s}, \quad (4.24)$$

where the halo mass m is expressed in units of $10^{13}M_\odot/h$. At $z = 0$ a typical halo has $m \approx 10^{13}M_\odot/h$, so the results essentially remain unchanged if we set $V_{1d} = 387/\sqrt{3}$ km/s and ignore the m dependence. This means that, to a good approximation, the distribution of the peculiar velocities along the line of sight, v , is Gaussian, and that this Gaussian is independent of the optical depth along the line of sight, τ .

Since the peaks in the kinematic effect have $k_{SZ} \sim \tau (v/c_{\text{light}})$, where τ and v are the values for the halo in the peak pixel, the discussion above implies that the distribution of k_{SZ} peak heights is obtained by taking the product of two independent distributions. In particular, because a halo's motion is nearly independent of its mass, the distribution of v is independent of τ , and therefore the width of the distribution of k_{SZ} at fixed τ should be proportional to τ . This is consistent with our Figure 4.5. Secondly, at fixed τ , the distribution of k_{SZ} is just the distribution of a constant τ times the distribution of v . Because halo motions are Gaussian, the distribution of k_{SZ} at fixed τ should be Gaussian; this is consistent with our Figure 4.4. (It is worth mentioning that Sheth & Diaferio 2001 showed that the rms motions of halos are higher in the dense regions. The dependence of a halo's peculiar velocity on its environment is the subject of work in progress.)

Let $p(\tau|m)d\tau$ denote the probability that a halo of mass m has optical

depth τ . Then

$$\begin{aligned}
 p(k_{\text{SZ}}) dk_{\text{SZ}} &= \int \frac{dm n(m)}{n_{\text{halos}}} \int d\tau p(\tau|m) \frac{p(v/c_1 = k_{\text{SZ}}/\tau|\tau, m) dk_{\text{SZ}}}{\tau} \\
 &= \int dm p(m) \int d\tau p(\tau|m) \frac{p(v/c_1 = k_{\text{SZ}}/\tau) dk_{\text{SZ}}}{\tau} \\
 &= \int d\tau \frac{p(v/c_1 = k_{\text{SZ}}/\tau) dk_{\text{SZ}}}{\tau} p(\tau) \int dm p(m|\tau), \quad (4.25)
 \end{aligned}$$

where we have written c_1 instead of c_{light} , and $n_{\text{halos}} \equiv \int d\tau n(\tau)$. The second equality follows from writing $n(m)/n_{\text{halos}} \equiv p(m)$, and using our assumption that the distribution of v is approximately independent of halo mass. The final expression follows from the fact that $p(m)p(\tau|m) = p(m|\tau)p(\tau)$ and rearranging the order of the integrals. Because the integral over m leaves a function of τ only, the final expression shows that, at fixed τ , the distribution of k_{SZ} is given by the distribution of v . Since this is Gaussian, our model produces a distribution of k_{SZ} which, at fixed τ , is Gaussian, in agreement with the simulations (Figure 4.4).

To compute the full distribution of k_{SZ} , we need a model for the distribution of τ at fixed m . We will do this in the next section. Here we note that if this distribution is sharply peaked about a mean value, $\tau(m)$ given by equation (4.16), we can replace $p(\tau|m)$ with a delta function. It then yields,

$$p(k_{\text{SZ}}) = \int \frac{dm n(m)}{n_{\text{halos}}} \frac{e^{-[k_{\text{SZ}}/\tau(m)/(V_{1d}/c_1)]^2/2}}{\sqrt{2\pi}(V_{1d}/c_1)\tau(m)}, \quad (4.26)$$

where we have explicitly shown the result when we substitute the Gaussian with width V_{1d} for the distribution of halo peculiar velocities.

The final integrand above is the product of the halo mass function and a Gaussian whose width increases as m increases, approximately as $\tau(m) \propto m^{2/3}$. In the next section we will show that $p(\tau|m)$ is not a delta function. Nevertheless, it is reasonably sharply peaked, so that the delta function is a good approximation. Our final expression above suggests that the distribution of k_{SZ} at fixed m should be Gaussian. This is a direct consequence of our neglect of the scatter in τ at fixed m . If we include the effects of the scatter (as will be described in the next section) then the first line of equation (4.25) above shows clearly that, even at fixed m , the distribution of k_{SZ} is a summation of Gaussians of different dispersions, so it will have a non-Gaussian feature.

Finally, we need to specify how the number density of halos depends on halo mass. To get the solid curve in Figure 4.6, we used the halo mass function

$n(m)$ given by Sheth & Tormen (1999). The model provides a good description of the simulations at $z = 0$. The dashed curves show the predicted contribution to the distribution from halos in different mass bins: the central spike of the distribution is from small mass halos ($10^{12} - 10^{13} M_\odot/h$), whereas the broad tails are entirely due to the more massive halos ($\geq 10^{14} M_\odot/h$).

4.2.5 Thermal effect

The CMB temperature fluctuation due to the thermal effect is given by

$$\begin{aligned}
 t_{\text{SZ}} &= \frac{\Delta T}{T} = \left(x \frac{e^x + 1}{e^x - 1} - 4 \right) \int n_e \sigma_{\text{T}} \frac{k_{\text{B}} T_e}{m_e c_{\text{light}}^2} dl \\
 &= -2 \int n_e \sigma_{\text{T}} \frac{k_{\text{B}} T_e}{m_e c_{\text{light}}^2} dl \quad (\text{as } x \rightarrow 0) \\
 &\approx -2 \frac{\sigma_{\text{T}} \Omega_{\text{b}}}{m_e \Omega_0} \int dl \frac{\sigma_{\text{dm}}^2(l)}{2c_{\text{light}}^2} \rho_{\text{dm}}(l), \tag{4.27}
 \end{aligned}$$

where $x \equiv h\nu/kT$, the second line shows the result in the Rayleigh-Jeans limit $x \rightarrow 0$, (throughout the chapter we will consider this limit), and the third line shows the approximation Diaferio et al. (2000) used to relate the density ρ_{dm} and line-of-sight velocity dispersion σ_{dm}^2 of dark matter particles in their simulations to the density and temperature of electrons. Namely, we assume the gas and the dark matter have similar spherically symmetric density profiles with isotropic velocity dispersions, so the additional assumption of hydrostatic equilibrium determines the velocity dispersion profile of the gas uniquely.

Before moving on we mention the relative amplitudes of the thermal and kinematic effects. The first line of equation (4.27) shows that the amplitude of the thermal effect depends on frequency. The kinematic effect, on the other hand, is independent of frequency. In the Rayleigh-Jeans limit, the amplitude of the thermal effect is much larger, typically an order of magnitude, than that of the kinematic effect. However, the thermal effect effectively vanishes at a frequency near 217GHz. Because the kinematic effect does not depend on frequency, the non-Gaussian signature due to the kinematic effect will be important near 217GHz.

Diaferio et al. (2000) found an approximate relation $t_{\text{SZ}} \approx -2\tau^2$, where the optical depth τ was defined in the previous section. Figure 4.8 shows that this relation also describes the thermal effect peaks in our considerably larger simulation box. This section describes a model to explain this relation, which allows us to compute the distribution of t_{SZ} peak heights. (We note that the

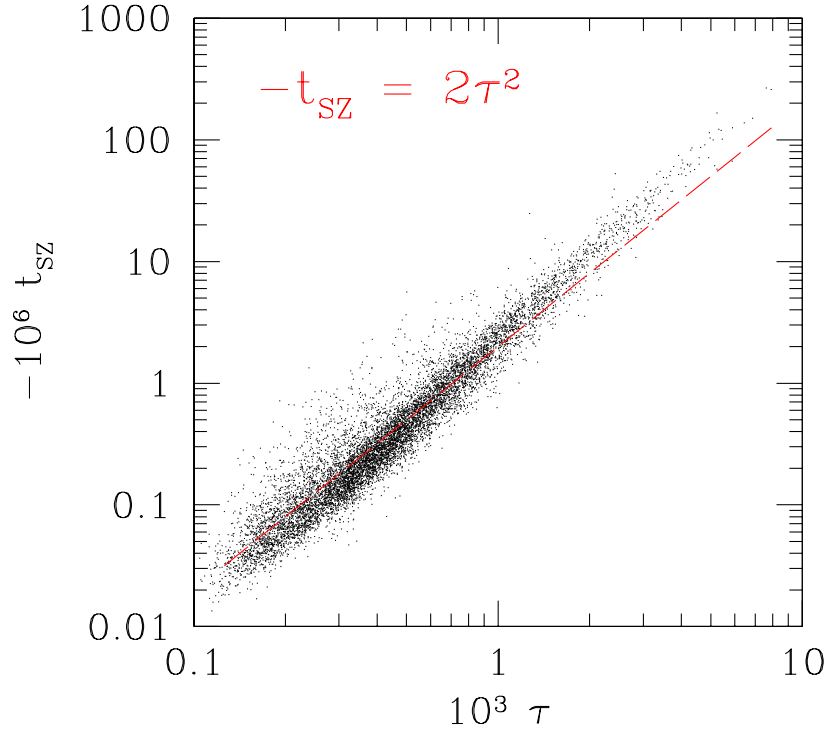


Figure 4.8 Scatter plot showing the height of a t_{SZ} peak as a function of optical depth τ .

mean relation between t_{SZ} and τ is analytically obtained by Cramphorn (2001). In the following we first repeat the derivation of the mean relation, and then include a scatter in the halo concentration parameter in order to obtain the peak distribution of τ .)

4.2.6 Mean relation between τ and t_{SZ}

Our model for the distribution of peaks in the thermal effect is similar in spirit to that for the kinematic effect: each peak in t_{SZ} is associated with the centre of a dark matter halo, and we ignore the possible but unlikely overlapping of halo *centers* along the line of sight. We can replace the integral over the line of

sight in equation (4.27) by an integral over the density-weighted temperature profile of a single halo of mass m and concentration c which happens to be in the line of sight:

$$t_{\text{SZ}}(c, m) = -2r_s \frac{\sigma_T \Omega_b}{m_e \Omega_0} \int_0^W \frac{2w \, dw}{W^2} \int dl \frac{\sigma^2(x|c, m)}{2c_{\text{light}}^2} \rho(x|c, m), \quad (4.28)$$

where $x^2 = l^2 + w^2$, and all distances are in units of the scale radius $r_s = r_{\text{vir}}/c(m)$, with r_{vir} the virial radius and c the concentration parameter (equation 4.18). As before, the integral over w represents the beam smoothing. This shows that the thermal effect is proportional to the integral of the density times the internal velocity dispersion, projected along the line of sight (recall that the kinematic effect is proportional to the density times the line-of-sight bulk motion of the halo).

In practice, there is some freedom in deciding what to use for the velocity dispersion σ^2 within a halo. Because we are assuming that the gas and the dark matter have similar spherically symmetric density profiles with isotropic orbits, the additional assumption of hydrostatic equilibrium determines the gas velocity dispersion profile, and hence the gas temperature profile uniquely. For the NFW profile, as well as for the Hernquist profile which we discussed earlier, the velocity dispersion profile $\sigma^2(r)$ has a fairly complicated functional form (Hernquist 1990; Cole & Lacey 1996). Although the shape of $\sigma^2(r)$ is indeed different from the circular velocity profile $Gm(< r)/2r$, the difference is not very large. The circular velocity profile has a much simpler functional form, and Cramphorn (2001) shows the result of setting $\sigma^2(r) = Gm(< r)/2r$, and then evaluating the required integral above for the NFW profile numerically. He shows that the result is well approximated by $\tau^2 \approx -t_{\text{SZ}}/2$.

For the Hernquist profile, the integral above can be done analytically, both for the correct one-dimensional dispersion, and for the case when the circular velocity is used to approximate the dispersion (see the Appendix). Recall that, on small scales, Hernquist's profile has the same slope as that of NFW, so we expect that using the Hernquist profile provides a reasonable analytic approximation. The upper solid curve in Figure 4.7 shows our analytic expression for the beam averaged $\sqrt{-t_{\text{SZ}}}$ associated with Hernquist profiles when the squared circular velocity is used for σ^2 , and the dashed curve shows the result of using the actual dispersion. The other curves in the Figure show the optical depth. Thus, Figure 4.7 shows that both $|t_{\text{SZ}}|$ and τ increase monotonically with halo mass. It can be seen that $-t_{\text{SZ}} \propto \tau^2$ is a good approximation. Notice however that the dashed line has a slope slightly steeper than two at high masses, and

this explains the slight deviation of the line from the dots at large τ in Figure 4.8. The constant of proportionality is of order two, consistent with the simulations. The difference between the solid and the dashed t_{SZ} curves can be thought of approximately illustrating what might happen if our assumption that the gas traces the spherically symmetric dark matter distribution is relaxed.

4.2.7 Distribution of τ and t_{SZ}

We have shown how to estimate the beam averaged optical depth and thermal SZ effect due to single halos of mass m . If all halos of a given mass had exactly the same density and velocity dispersion profiles, then we would be able to translate the distribution of halo masses into distributions of τ and t_{SZ} . In fact, halos of fixed m do *not* all have the same profile shape: the distribution of shapes is well parametrized by assuming that the profile is always of the form given by a unique NFW profile, but letting the concentration parameter c defined earlier follow a lognormal distribution (Jing 2000; Bullock et al. 2001). Therefore, we assume that

$$p(t_{\text{SZ}}|m) dt_{\text{SZ}} = \frac{dc/c}{\sqrt{2\pi\sigma_c^2}} \exp\left(-\frac{\ln^2[c(t_{\text{SZ}}, m)/\bar{c}(m)]}{2\sigma_c^2}\right), \quad (4.29)$$

where the mean concentration at fixed mass, $\bar{c}(m)$, is given by equation (4.18), and we adopt the rms scatter, $\sigma_c \approx 0.2$, which is approximately independent of halo mass. The number density of the thermal effect peaks of height t_{SZ} is just this times the number of halos of mass m , integrated over all m :

$$n(t_{\text{SZ}}) dt_{\text{SZ}} = \int dm n(m) p(t_{\text{SZ}}|m) dt_{\text{SZ}}. \quad (4.30)$$

To proceed, we need $c(t_{\text{SZ}}, m)$. By inverting the $t_{\text{SZ}}(c, m)$ relation given above, we obtain the expression. Recall that $t_{\text{SZ}}(c, m)$ can be evaluated analytically if the profile has the form given by Hernquist (1990), so that the Jacobian dc/dt_{SZ} can also be given analytically.

The number density of peaks of height τ in the optical depth distribution can be calculated analogously:

$$n(\tau) d\tau = \int dm n(m) p(c(\tau, m)|m) \frac{dc(\tau, m)}{d\tau} d\tau. \quad (4.31)$$

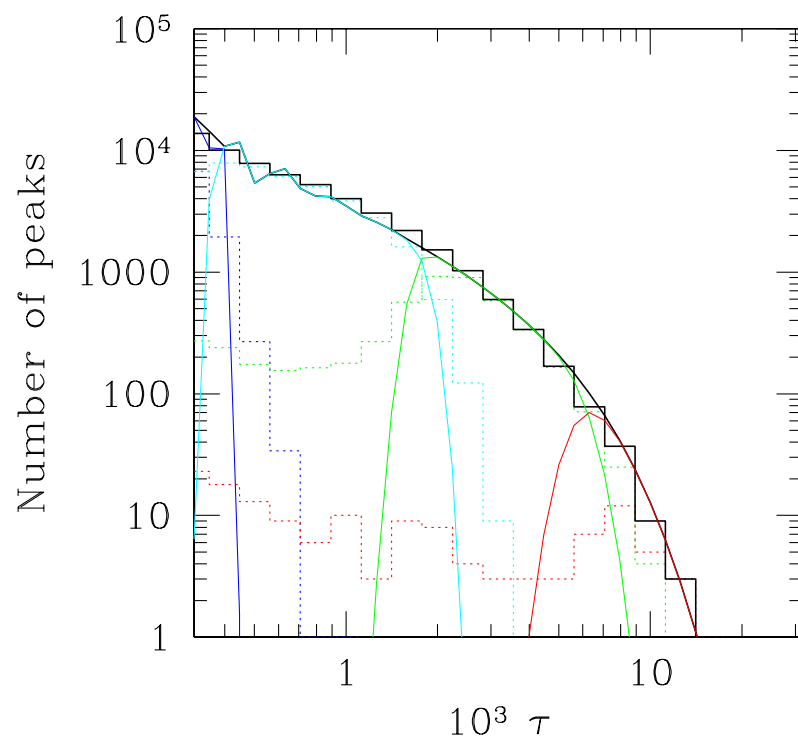


Figure 4.9 Distribution of optical depth peaks τ in the simulations (solid histograms) and in our model (smooth solid curves). Dashed lines show the contributions to the total from halos with mass in the range 10^{13} – 10^{14} , 10^{14} – 10^{15} , and $\geq 10^{15} M_{\odot}/h$.

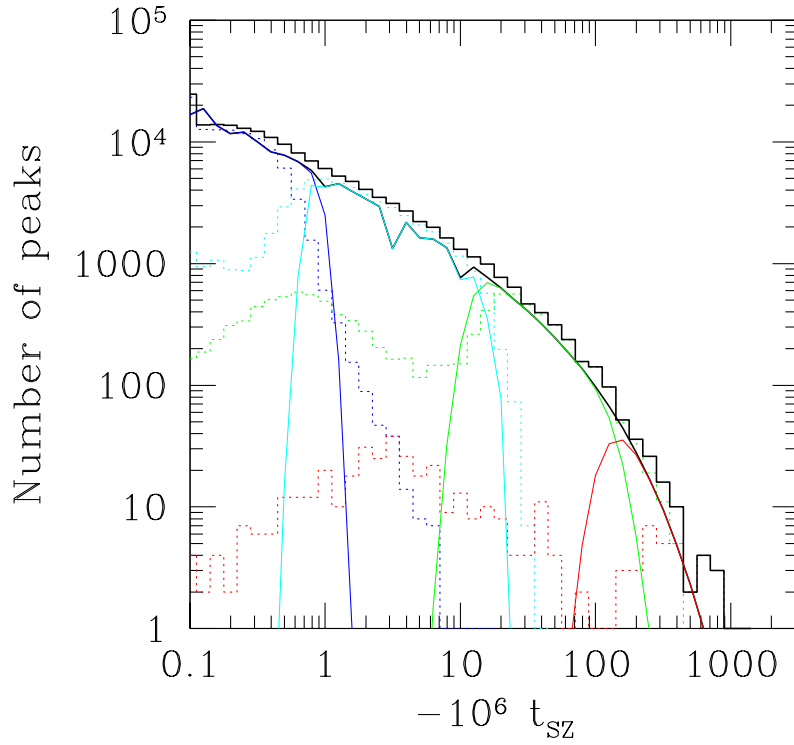


Figure 4.10 Distribution of peak heights t_{SZ} in the thermal effect in the simulations (solid histograms) and in our model (smooth solid curves). Both simulations and model assume that the gas traces the dark matter. Dashed lines show the contributions to the total from halos with mass in the range 10^{13} – 10^{14} (dominate at small τ), 10^{14} – 10^{15} , and $\geq 10^{15} M_{\odot}/h$ (dominate at large τ).

Figs. 4.9 and 4.10 show the distributions of optical depth and thermal effect peak heights in the simulations. Solid lines show the total number density of peaks, and dashed lines show the contributions to the total from halos in small mass ranges. In the model, for the sake of simplicity, we compute t_{SZ} (see equation (4.28)) using the Hernquist profile and its corresponding circular velocity. The dashed lines were computed by locating dark matter halos using the spherical overdensity algorithm with density threshold 200 (details are in Tormen 2001, in preparation). Simulation particles which reside in the dark matter halos in a given mass range were marked, and then the SZ effect and the Thomson optical depth were computed by using only the marked particles. A slight deviation of the model prediction for the most massive halos ($\geq 10^{15} M_{\odot}/h$) is partly due to the fact that the Sheth-Tormen mass function slightly overestimates the number of massive halos (Jenkins et al. 2001).

Note that these distributions are bimodal; our model fits the large τ peak for each mass range reasonably well. This suggests that the large τ peak is due to the central cusp of a halo, whereas the increase at small τ is primarily due to the substructure of halos which our model does not account for. Since we identify peaks in the simulated maps as the local maxima, it is expected that substructures in large halos appear also as peaks. Note, however, hot gas in real clusters is observed to be smoothly distributed. The increase at small τ is due to our simple assumption that the baryons trace the dark matter even within dark halos, which is invalid for hot gas.

The careful reader will have noticed that a scatter in c at fixed m leads to a scatter in optical depth τ at fixed mass m . This, in turn, leads to scatter in the kinematic effect k_{SZ} , which is in addition to the scatter due to halos' peculiar velocities v . Since the scatter in bulk velocities v is the dominant cause of the scatter in k_{SZ} at fixed m , we do not take into account the scatter which is due to the distribution of halo concentrations at fixed m .

4.2.8 Discussion

We have presented a simple model for the distribution of peak heights in maps of the kinematic and thermal Sunyaev-Zeldovich effects.

In our model there is a one-to-one correspondence between a peak in the kinematic or the thermal effect and the presence of a massive cluster. The shape of the distribution of peaks is determined by the mass function of clusters, and by the peculiar velocity distribution. If the distribution of initial density fluctuations is Gaussian, then the motions of clusters along the line of sight

should be reasonably well fit by a Gaussian, so one might have expected the distribution of k_{SZ} peak heights to also be Gaussian. Our simulations showed that, in fact, the distribution of k_{SZ} peak heights is highly non-Gaussian. We argued that this is explained by the fact that the kinematic effect is proportional to the product of the cluster velocity and its optical depth. The optical depths of clusters depend strongly on cluster mass, and the mass range of clusters which cause peaks in the kinematic effect is quite large. In our model, the cluster mass function and the rms motions of clusters are quantities which can be computed if the initial spectrum of density perturbations is specified. Therefore, the kinematic effect can be used to constrain the shape of this spectrum.

Our model also allowed us to estimate the distribution of peak heights in the optical depth (which is not observable) and in the thermal effect (which is). We used a simple but rigorous model to predict the shapes of these non-Gaussian distributions if gas traces the dark matter, and tested the prediction against the numerical simulation. Our model was able to describe the simulations quite well. For the optical depth and for the thermal effect, the non-Gaussianity was a consequence of the non-Gaussian shape of the halo mass function.

The main aim of this chapter was to show how our knowledge of halo speeds and profiles can be used to model the thermal and kinematic SZ effects. Many physics are missing in our model for the density and temperature distribution of the gas in real clusters, so the model should be regarded as a simplest approach, rather than a precise method. However, it is straightforward to incorporate additional physical processes such as the core evolution of the intracluster gas if they can be appropriately modelled.

We have only dealt with the *secondary* CMB temperature fluctuations. Real CMB maps will have the peaks of the SZ effects on top of the primary fluctuations. The primary fluctuations are Gaussian distributed with an rms, on arcminute scales, of about 4×10^{-5} . This rms is about the same order as decrements due to the thermal SZ effect, and an order of magnitude larger than the typical kinematic SZ effect. The *spatial* and *spectral* features of the SZ effects will help us to distinguish the two contributions. First, the angular structure of the SZ effect is quite different from that of the primary fluctuation. In our Λ CDM model, the SZ effect fluctuations and the primary fluctuations dominate the angular power spectrum of the CMB on substantially different scales, which separate at $\ell \sim 3000$ (see the next section and also Springel, White & Hernquist 2001). Thus, in principle, an optimal high-pass filter for the arcminute scale should be able to isolate the peaks due to the SZ effects from the primary fluctuations. We have carried out the following experiment.

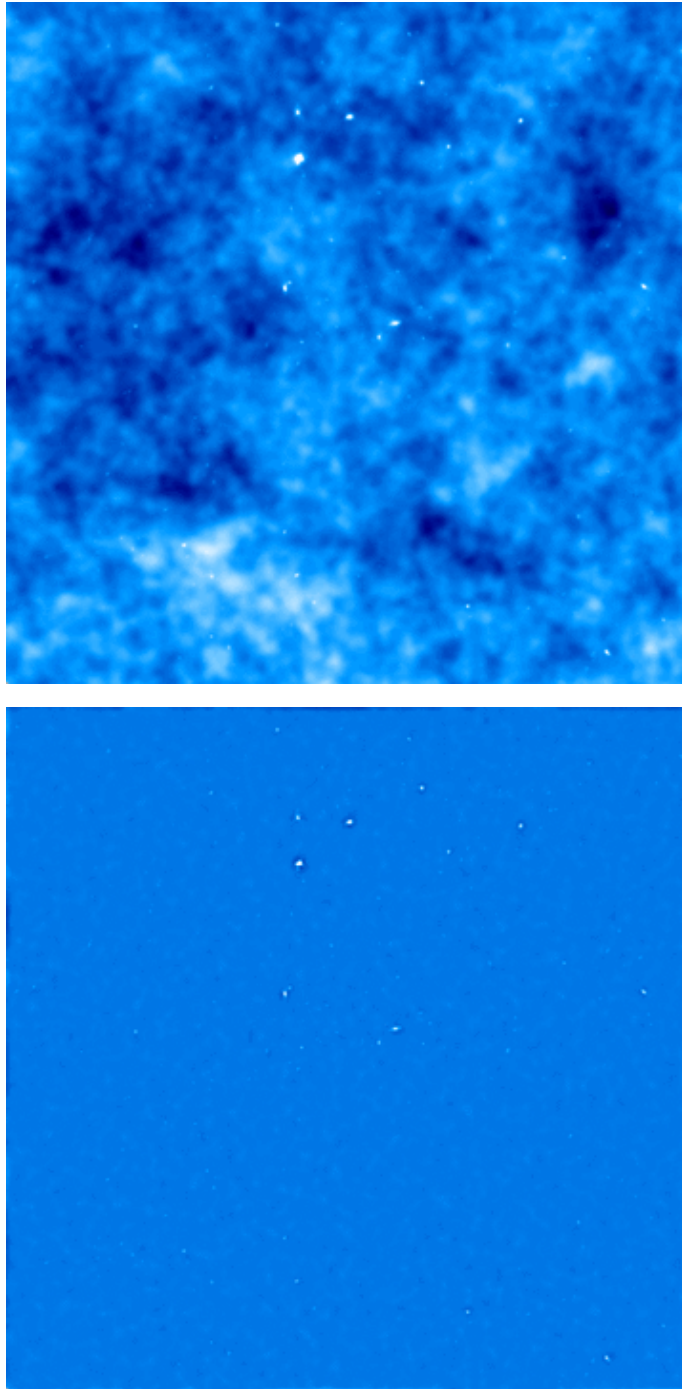


Figure 4.11 Distribution of temperatures in simulated $8^\circ \times 8^\circ$ maps of the intrinsic CMB fluctuations with the thermal SZ effect fluctuations superimposed. Top panel shows the full map, and bottom panel shows what remains after applying a high-pass filter of scale one arcminute. The maps shown here are part of the full map computed from the entire $480\text{Mpc}/h$ box.

If we put our simulation box at $z=0.218$, then the angular size of one pixel is 1 arcminute, and the whole box occupies $40^\circ \times 40^\circ$ square-degrees. In Figure 4.11, we show a small $8^\circ \times 8^\circ$ piece of the whole map, so as to make smaller angular scale structures visible. (For the analysis in Figure 4.12, however, we use the entire map.) The top panel in Figure 4.11 shows a simulated temperature map in which the t_{SZ} effect fluctuations are superimposed on the primary fluctuations generated at the last scattering epoch. We made a two dimensional random Gaussian field for the primary temperature fluctuations. We computed the angular power spectrum by CMBFAST for the Λ CDM model we consider here. The bottom panel shows the effect of applying a high-pass filter of scale one arcminute to this map; the large scale modulations (mostly due to the primary fluctuations) are gone, and only small scale fluctuations (due to the SZ effect) remain.

Figure 4.12 shows the distribution of temperature peak heights in the simulated map which has both primary and t_{SZ} fluctuations (dashed histogram) and in the high-pass filtered map (solid histogram); i.e., the peak height distributions in the maps shown in Figure 4.11. The Gaussian-like shape of the dashed curve for the unfiltered map is primarily due to the peak height distribution of the intrinsic peaks (we have verified that it is well described by the analytic formula for peaks in two-dimensional Gaussian random fields given in Bond & Efstathiou 1987); the t_{SZ} peaks account for most of the large decrement tail. The solid histogram in the left panel, from the filtered map, is slightly asymmetric. If we assume that the positive peaks are due to the intrinsic CMB fluctuations, whereas the decrements are either intrinsic or t_{SZ} peaks, then subtracting the positive side from the negative should leave the t_{SZ} peak distribution. The dashed histogram in the right panel shows what remains after doing this subtraction. It should be compared with the true distribution of t_{SZ} peaks which we presented earlier, and is now shown as the solid histogram. The smooth solid curve shows what our model predicts. Notice how similar the dashed and solid histograms are. This demonstrates that by suitably filtering the map, it should be possible to recover the true distribution of t_{SZ} peaks, and that our model gives an excellent estimate of this distribution.

Unfortunately, this simple method will not work for recovering the distribution of the k_{SZ} peaks because of the smallness of the k_{SZ} amplitudes. It is however possible to distinguish the kinematic from the thermal effect. To do so we must use their different spectral properties: multi-band follow-up observations of regions with deep and highly clustered t_{SZ} decrements will assure the presence of a supercluster where the k_{SZ} effect is largest (e.g. Diaferio et al. 2000).

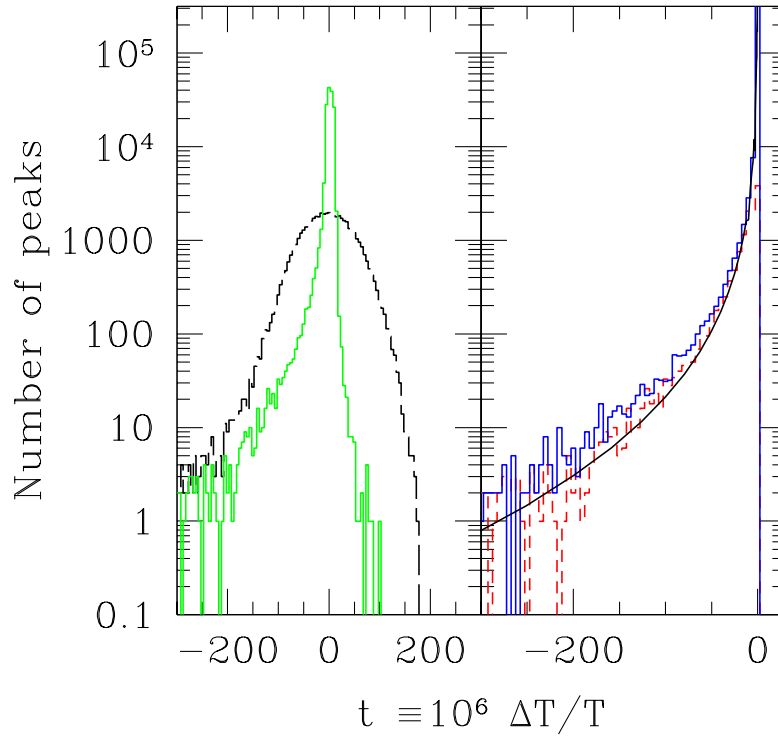


Figure 4.12 Distribution of peak heights in simulated temperature maps. Dashed histogram in panel on left shows the peaks in the unfiltered map shown (Figure 4.11 top). Solid, slightly asymmetric histogram shows the peak heights in the high-pass filtered map (Figure 4.11 bottom). Right panel compares the actual t_{SZ} peak decrements (solid histogram) and the peak distribution after subtracting the positive peak height distribution from the negative side in the filtered map (dashed histogram). Solid curve shows what our model predicts. The final distribution in the filtered map is similar to the actual t_{SZ} distribution, and is similar to what our model predicts.

It is worth mentioning that, in fact, the t_{SZ} peaks will also appear in clustering statistics. The shape of the correlation function of the peaks which were imprinted on the background radiation at the last scattering surface depends on peak height (Bond & Efstathiou 1987; Heavens & Sheth 1999; Heavens & Gupta 2001). The presence of t_{SZ} peaks will change this dependence because, as our model shows, the two-point correlation function of the SZ peaks is related to the two-point correlation function of massive clusters. Since accurate analytical models for the clustering of clusters exist (e.g. Mo & White 1996; Sheth & Tormen 1999; Colberg et al. 2001), the clustering of the peaks in the SZ effect can be estimated rather easily, although we have not done so here. The clustering of clusters depends differently on the initial spectrum of fluctuations than the clustering of intrinsic peaks does. Therefore, our model for the t_{SZ} peak distribution will be important if one wishes to obtain constraints on the initial fluctuation spectrum by studying the two-point and higher order moments of peaks in the microwave background on arcminute scales.

Finally, note that our model assumes that there is a one-to-one correspondence between a peak in the kinematic or thermal effects and the presence of a massive cluster. We showed that, at low redshift, this is a good approximation—our model describes the simulations quite well. At higher redshifts this assumption is likely to break down for the kinematic SZ effect. This is because, at higher redshifts, there are fewer massive halos with sufficiently high optical depths to produce obvious peaks. In particular, the number density of massive clusters drops faster than the typical coherent-flow speed does, so that an increasing fraction of peaks will be caused by the velocity field at higher redshifts, rather than by the density field.

Since the kinematic peaks due to coherent flows at high redshift have a different angular structure from those due to nearby clusters, an optimal filter will be able to distinguish the two types of peaks. Developing a model for this additional effect is the subject of work in progress.

4.3 THE SZ POWER SPECTRUM

The Sunyaev-Zel'dovich effect from clusters can have a great influence on the CMB temperature fluctuation because the surface brightness of the Sunyaev-Zel'dovich effect from a cluster is redshift independent and does not suffer $(1+z)^{-4}$ fading. Thus the number of clusters at high redshifts significantly affect the fluctuation pattern in the CMB and the amplitude of the CMB power spectrum on arcminute scales. There have been a number of studies on the fluctuation power spectrum, both by analytical methods (Cole & Kaiser 1988; Komatsu & Kitayama 1999; Cooray 2000) and by numerical simulations (Refregier et al. 2000; da Silva et al. 2000; Springel et al. 2000; Seljak et al. 2001). The shape and the amplitude of the Sunyaev-Zel'dovich power spectrum is quite sensitive to assumed cosmological parameters (hence it is useful to put a constraint on the cosmological and cluster evolution models). Unfortunately the published results seem to lack a consistency even for an almost identical cosmology (see Springel et al. 2000 for a comparison of the results by various authors). Presumably the differences are due to the treatment of the gas distribution in clusters in the analytic models, and due to finite box sizes and limited resolution in the numerical simulations. Sheth & Diaferio (2001) showed that lack of large scale power in a small simulation box results in a significant underestimate of the halo peculiar velocities. Refregier & Teyssier (2000) state that a small simulation box will misestimate the number of massive clusters which give a significant contribution to the mean Compton y -parameter, and a follow-up study of Komatsu et al. (2000) showed that the expected deviation due to the finite box size in the power spectra does exist between their analytical estimate and the simulation result, both on large and small angular scales. We make simulated SZ effect maps from our large simulation. The large simulation box allows us to make a simulated map for a wide patch of the sky.

4.3.1 Map making

We use the same simulation set as in the previous section. In order to make fake “lightcone” outputs, we use a number of simulation outputs at discrete redshifts. The redshift intervals are chosen such that the comoving separation between adjacent outputs is always less than the box side length. By putting

the simulation outputs one by one along the past lightcone of a hypothetical observer, the comoving volume within the lightcone can be entirely filled. The resulting set of the outputs includes, although not smoothly, the clustering evolution along the lookback time. We stack 13 simulation boxes in total over a redshift range $0 < z < 7$. In practice, when we create SZ maps, we randomly re-orient the boxes so that the same structure does not appear more than once along a line-of-sight. In Figure 4.13 we show the simulated maps of the thermal and kinematic Sunyaev-Zel'dovich effect. The field of view shown is 3.4×3.4 square-degree field, and the map resolution is 0.1 arcminute. In creating the tSZ effect map, we consider only the matter in collapsed halos in the same manner described in section 4.2.8. For the kinematic effect, we consider two extreme cases. One is that only the matter within collapsed halos contributes, and the other is to assume that the universe is ionised by redshift 7 (the farthest point in our fake lightcone output). Therefore, for the latter case, we consider all the dark matter particles in the simulation to create the kSZ maps on the assumption that baryons trace the dark matter.

In Figure 4.13, some of the large clusters found in the tSZ map do *not* appear as obvious spots in the kSZ map; their line-of-sight velocities are small and do not cause large kSZ fluctuations. It is also interesting that the bright spots (massive clusters) in the tSZ map appear in dipole shapes consisting of nearby positive and negative peaks, as suggested by Diaferio et al. (2000). Often, such regions in the kSZ map are not just because of a superposition of clusters along a line-of-sight, but they are indeed *supercluster* regions, where clusters are moving fast due to nonlinear effects.

4.3.2 The angular power spectrum

From the simulated SZ maps, we compute the angular power spectrum in the flat sky limit. We have created 10 maps for both the thermal effect and the kinematic effect. The power spectra measured from an ensemble of the 10 maps are shown in Figure 4.14. Our result broadly agrees with the other published estimates for the same cosmology, and the agreement is particularly good with the result of Springel et al. (2000). In Figure 4.14, the thermal effect dominates over the primary fluctuations from $l \sim 2000$, and on these scales the kinematic effect is about an order of magnitude lower than the thermal effect. The dashed line in the figure is the kSZ power spectrum computed from the same set of maps, but with only the matter in dark halos considered. The amplitude is about a factor of two smaller than the power spectrum computed by taking *all* the particles into account. The difference may suggest that the

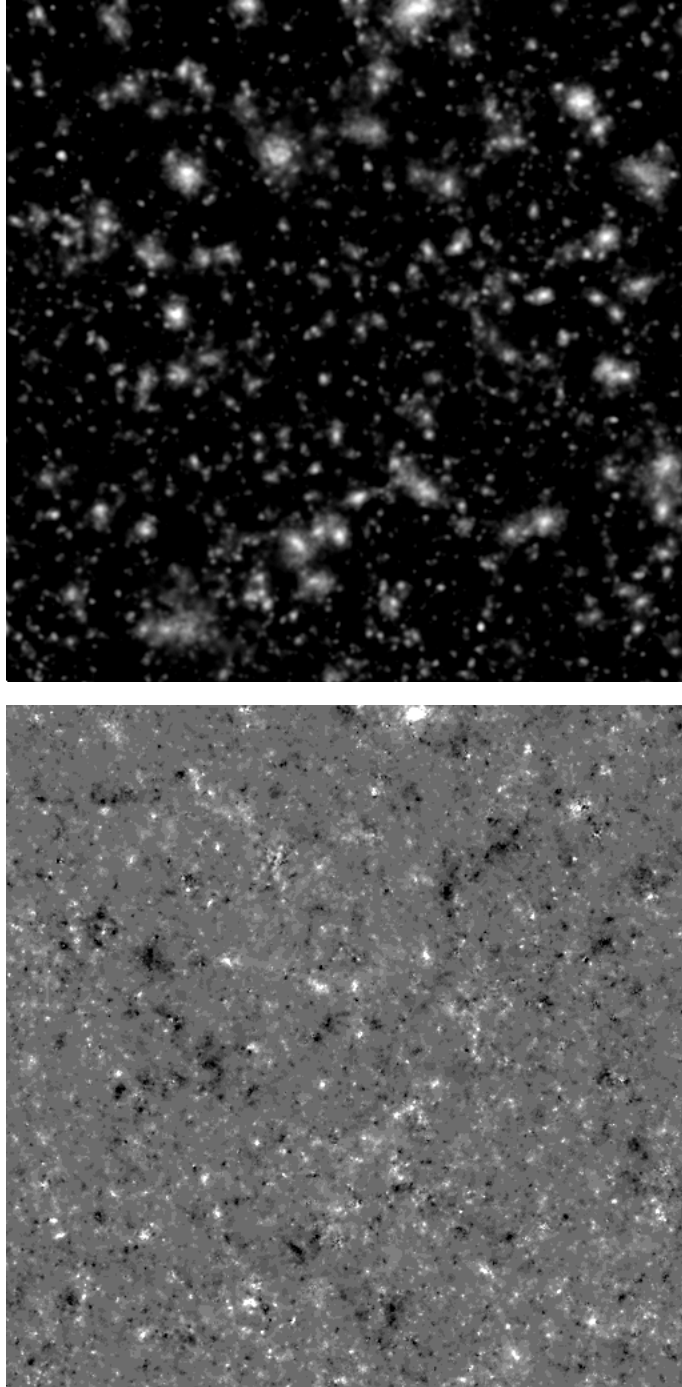


Figure 4.13 Simulated map of the tSZ (top) and kSZ (bottom) effect. The maps cover the same field of view of 3.4° on a side. The color scales are such that the temperature decrements $\Delta T/T_{\text{CMB}}$ are logarithmically scaled from black to white (1×10^{-3}) in the top panel, where the fluctuations below 1×10^{-5} are saturated, while the temperature fluctuations are linearly scaled between white ($+3 \times 10^{-5}$) and black (-3×10^5) in the bottom panel.

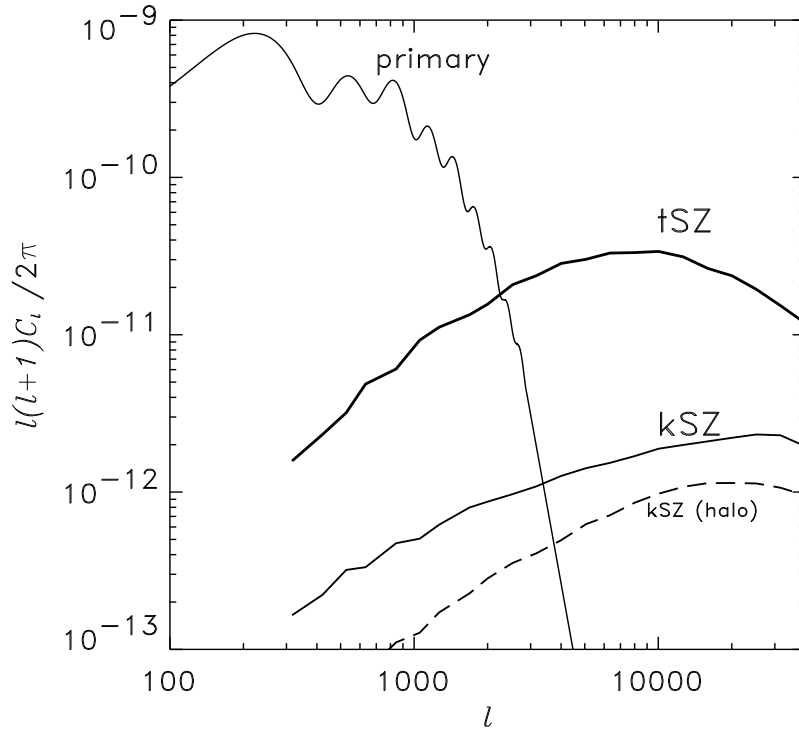


Figure 4.14 The angular power spectra of the thermal and kinematic Sunyaev-Zel'dovich effect computed from our simulated maps. The power spectrum of the primary fluctuations is also plotted for a reference. We computed it by CMBFAST (Seljak & Zaldarriaga 1996). The dashed line is the contribution from collapsed objects to the total power spectrum of the kinematic effect.

resulting power spectrum is sensitive to the assumption on the reionisation history of the universe. Recall that we assumed that the universe is fully ionised by redshift 7. Since a large fraction of the power on large angular scales is due to large-scale coherent motions, the “diffuse” materials outside halos at high redshift makes a substantial contribution to the power on large angular scales, as seen in Figure 4.14. We emphasise that the situation is quite different for the thermal effect. Since the thermal effect is proportional to the product of the density and the temperature of a gas cloud, most of the power is generated by massive clusters, and the “diffuse” material makes only a negligible contribution to the total power.

4.3.3 Discussion

By using a large box simulation, we have made a reliable estimate for the angular power spectrum of the kinematic Sunyaev-Zel'dovich effect. For the thermal Sunyaev-Zel'dovich effect, although our assumptions on the gas distribution in clusters are very simple, the computed power spectrum has turned out to be consistent with the published estimates from hydrodynamic simulations. The measured kSZ power spectrum is about an order of magnitude smaller than the tSZ power spectrum in the range $1000 < l < 100000$. The angular scales discussed in this chapter are well beyond the reach of the planned satellite missions *MAP* and *Planck*, but the future mm-wavelength interferometric experiment ALMA will be able to detect the kinematic effect and measure (or at least provide an upper limit to) the power spectrum on scales $10^4 < l < 10^5$.

If the reionisation happens in a *patchy* pattern, it will cause appreciable secondary CMB anisotropies. The degree of the anisotropies caused by reionisation depends quite sensitively on the reionisation epoch and detailed scenario, i.e. what the ionising sources are and how large ionised bubbles can be made. Recent studies on the patchy reionisation (Gruzinov & Hu 1998; Valageas, Balbi & Silk 2000; Gnedin & Jaffe 2001) seem to agree on that the expected amplitude of the effect is smaller than that due to the kinematic Sunyaev-Zel'dovich effect from clusters.

Since our simulation gives the estimate for the power spectrum for only a specific cosmology (Λ CDM model), an important extension is to develop an analytic model to compute the power spectrum and test such a model against the simulation result. In the light of this, applying the model described in section 4.2 for a range of redshift is planned.

There are various applications using the simulated maps. An interesting question is whether appreciable non-Gaussian signatures due to the SZ effect are found in the CMB temperature fluctuations. Since, unlike the thermal effect, the kinematic effect cannot be disentangled from the primary fluctuations by using their spectral features, it is important to know the degree of non-Gaussianity due to the kinematic effect. In a paper in preparation (Yoshida & Schmalzing 2001), we will address the question by using the Minkowski functionals.

Appendix: Projections of Hernquist profiles

The main text uses expressions for the density and the density-weighted temperature profiles of dark matter halos integrated along the line of sight. For the Hernquist profile, both these integrals can be done analytically (Hernquist 1990). (Analytic results can also be obtained for many of the more general profiles in Zhao 1996; in the interests of brevity, we have not provided explicit expressions here.)

The density at $x = r/r_s$, where r_s is a scale radius, from the centre of a Hernquist profile is

$$\rho(x) = \frac{m(1+b)^2}{2\pi b^3 r_{\text{vir}}^3 x(1+x)^3}, \quad (4.32)$$

where $b = r_s/r_{\text{vir}}$ is the scale radius in units of the virial radius. Reasonable agreement with Navarro et al. (1997) profiles of the same m and concentration c can be got by setting $b = \sqrt{2}/c^{0.75}$ (Sheth et al. 2001).

The integral over the density, which is related to the optical depth, is

$$I(z) = \int \rho(x) dl = \frac{m(1+b)^2}{2\pi b^2 r_{\text{vir}}^2} \frac{(2+z^2)h(z) - 3}{(z^2-1)^2}, \quad (4.33)$$

where, in the integrand, $x^2 = l^2 + z^2$, with x , l , and z all in units of the scale radius br_{vir} , and $h(z)$ is given in the main text. This quantity, averaged over a circular window of radius R , is

$$2 \int_0^Z \frac{dz}{Z} \frac{z}{Z} I(z) = 2 \frac{m(1+b)^2}{2\pi b^2 r_{\text{vir}}^2} \frac{1-h(Z)}{Z^2-1}, \quad (4.34)$$

where $Z \equiv R/(br_{\text{vir}})$.

There is some freedom as to how we should estimate the temperature. If we assume that the halo is not rotating, then the quantity of interest is the density-weighted line-of-sight velocity dispersion. If the distribution of orbits of dark matter is isotropic, and the gas moves like the dark matter, then this is

$$S(z) = \frac{Gm}{br_{\text{vir}}} \frac{m(1+b)^4}{2\pi b^2 r_{\text{vir}}^2} \left[\frac{6 - 65z^2 + 68z^4 - 24z^6}{12(1-z^2)^3} - \pi z \frac{z^2 h(z)(8z^6 - 28z^4 + 35z^2 - 20)}{4(1-z^2)^3} \right], \quad (4.35)$$

and the average over a circle is

$$\begin{aligned}
2 \int_0^Z \frac{dz}{Z} \frac{z}{Z} S(z) &= 2 \frac{Gm}{br_{\text{vir}}} \frac{m(1+b)^4}{2\pi b^2 r_{\text{vir}}^2} \\
&\times \left[\frac{3 - 17Z^2 + 22Z^4 - 8Z^6}{12(1-Z^2)^3} - \frac{\pi Z}{3} \right. \\
&\quad \left. + h(Z) \frac{15Z^2 - 20Z^4 + 8Z^6}{12(1-Z^2)^2} \right]. \tag{4.36}
\end{aligned}$$

If, instead, we use one half of the circular velocity squared,

$$\frac{v_c^2}{2} \equiv \frac{Gm(< r)}{2r} = \frac{Gm(1+b)^2}{2br_{\text{vir}}} \frac{x}{(1+x)^2}, \tag{4.37}$$

then we need

$$V(z) = \int \frac{v_c^2(x)}{2} \rho(x) dl = \frac{Gm}{br_{\text{vir}}} \frac{m(1+b)^4}{2\pi b^2 r_{\text{vir}}^2} \frac{h_2(z)/2}{(z^2-1)^4}, \tag{4.38}$$

where

$$h_2(z) = \frac{6 + 83z^2 + 16z^4}{12} - \frac{5z^2(4 + 3z^2)}{4} h(z).$$

This, averaged over a circle of radius Z is

$$2 \int_0^Z \frac{dz}{Z} \frac{z}{Z} V(z) = \frac{Gm}{br_{\text{vir}}} \frac{m(1+b)^4}{2\pi b^2 r_{\text{vir}}^2} \left[\frac{-3 - 14Z^2 + 2Z^4}{12(Z^2-1)^3} + \frac{15Z^2 h(Z)}{12(Z^2-1)^3} \right]. \tag{4.39}$$

CHAPTER 5

**Gas cooling and the formation of
galaxies in clusters**

5.1 INTRODUCTION

Gasdynamical and radiative processes coupled with gravitational instability play a crucial role in the formation of galaxies. In hierarchically clustering universes galaxies are formed via the dissipative condensation of baryonic components in dark matter halos (White & Rees 1978). Analytic theories of galaxy formation within this framework are well developed (White 1994 and references therein), and more sophisticated semi-analytic models that incorporate the formation and evolution of dark matter halos and of baryons within them have met great success (White & Frenk 1991; Lacey & Silk 1991; Kauffmann, White & Guiderdoni 1993; Cole et al. 1994; Kauffmann et al. 1999).

A full description of galaxy formation requires treatment of a number of complex physical processes, and the required huge dynamic range makes it almost impossible to model the processes from first principles in a numerical simulation. Semi-analytic modelling of galaxy formation tackles this problem by treating the complicated physics in a simplified yet physically motivated manner. In the models the merging history of the dark matter halos in which galaxies are to be embedded is used as the principal dynamical input, and the following key physics are then implemented: (1) the shock heating and virialisation of the gas in the halos, (2) the radiative cooling of the gas, (3) the star formation in the cooled gas, and (4) the energy feedback by supernovae and stellar winds. The original work by White & Frenk (1991) already suggested that incorporating star formation and subsequent energy release from supernovae is necessary to circumvent the early over-production of stars, i.e., all of the above processes must be taken into account in realistic models. The output from such semi-analytic models has been studied in detail and tested against observational data, showing that the models can successfully reproduce many observed properties of galaxies (Kauffmann et al. 1999; Benson et al. 1999; Somerville & Primack 1998, Springel et al. 2001).

Although the analytical treatments in these models are physically plausible and the resulting statistical properties of galaxies such as luminosity functions and populations of different morphological types are in reasonable agreement with observations, the validity and the limitations of each model assumption are as yet unclear. Among the four major ingredients listed in the above, the first two are well understood physical processes and they can be incorporated in hydrodynamical simulations in a direct and transparent manner. Recently

Benson et al. (2001) studied the evolution of cooling gas associated with galaxy formation both in Smoothed Particle Hydrodynamics simulations and in a semi-analytic model using Monte Carlo merger trees. By comparing the outputs from the two different models, they found a reasonable agreement in gas properties such as the global fractions of gas in cold, hot and uncollapsed phases, and the amount of cold gas in dark halos. While their results suggest that the basic assumptions in the semi-analytic models give an appropriate description of the galaxy formation, it remains unclear whether the gas in the dark matter halos behaves in detail as assumed in the models. It is therefore natural to ask whether the prescriptions in the semi-analytic modelling are consistent with the actual dynamics at various stages of the formation of *individual* objects. Studies at an “object-by-object” level are clearly needed to verify this.

In this chapter we present the analysis of a set of numerical simulations of rich galaxy clusters. We carry out a hydrodynamic simulation with an adiabatic gas and repeat the same simulation with radiative cooling and a UV radiation background. We study the effect of gas cooling on the properties of simulated clusters and galaxies. Using the dark matter part of the simulation only, we run a modified semi-analytic model which closely mimics various features of the hydrodynamic simulation. We compare the properties of galaxies in the semi-analytic model and in the hydrodynamic simulation. Specifically we study the mass fractions of the cold dense gas and the diffuse hot gas in dark matter halos. Since all of our simulations start from an identical initial condition, an almost perfect matching of dark halos (and hence of galaxies) can be made among the outputs of the different simulations. We explicitly study the level of agreement between the properties of individual galaxies in the two different models of galaxy formation.

5.2 THE N -BODY/SPH SIMULATIONS

We work with a flat Λ -dominated Cold Dark Matter universe, with matter density $\Omega_m = 0.3$, cosmological constant $\Omega_\Lambda = 0.7$ and expansion rate $H_0 = 70\text{km}^{-1}\text{Mpc}^{-1}$. We select the second most massive cluster in the GIF

Table 5.1 Parameters of the cluster simulation

Run	N_{tot}	N_{high}	$m_{\text{dark}} (h^{-1}M_{\odot})$	$m_{\text{gas}} (h^{-1}M_{\odot})$	$l_{\text{s}}(h^{-1}\text{kpc})$
S0	3.2×10^6	0.2×10^6	1.19×10^{10}	2.1×10^9	30

simulation (Kauffmann et al. 1999) and resimulate the cluster by a multiple mass technique with a gaseous component. The simulation parameters are given in Table 5.1, where N_{tot} is the total number of dark matter particles in the simulation, N_{high} the number of particles in the central high-resolution region (=the number of gas particles), m_{dark} is the mass of each high-resolution particle, m_{gas} is the mass of each gas particle, and l_{s} stands for the gravitational softening length. The simulations are carried out with the parallel tree N -body/SPH code GADGET developed by Springel (1999; see also Springel, Yoshida & White 2001). We implement gas cooling in the SPH part of the code in a similar manner to that in Katz, Weinberg & Hernquist (1996, hereafter KWH). As in KWH we compute the abundances of ionic species by assuming collisional equilibrium for a primordial composition gas consisting of 76% hydrogen and 24% helium. The cooling functions are taken from Sutherland & Dopita (1993). We call the simulation ‘‘S0-C’’ (for cooling).

In the simulation a time-dependent uniform UV background radiation is also included as in KWH, but its effect, especially on the destruction of small objects, is very small at the resolution of our simulation (Weinberg, Katz, & Hernquist 1997), hence the inclusion of the UV heating is not important for our analysis. We fix the minimum smoothing length and do not allow the gas smoothing length to drop below one-fifth of the gravitational softening length. We set the number of neighbouring particles in the SPH simulation, N_{NGB} , to be 32. The gas can cool efficiently in objects above this mass limit. This resolution effect results in the absence of cold dense gas in small halos.

We carried out a simulation with the gas cooling and the UV heating turned off. The gas then behaves adiabatically except in shock regions. We call this simulation ‘‘S0-A’’ (for adiabatic). We dumped 50 outputs between redshift 20 and 0. The output times are chosen such that the expansion parameter grows by a constant factor between adjacent two outputs.

5.3 CLUSTER PROPERTIES

We first present the basic properties of the simulated clusters. The virial radius of the main cluster at the present epoch is $1.48h^{-1}\text{Mpc}$, and the corresponding virial mass is $7.7 \times 10^{14}h^{-1}M_{\odot}$. Figure 5.1 shows the projected gas mass distribution around the main cluster in S0-A and S0-C. Bright clumps seen in the bottom panel (S0-C) are groups of cold gas particles, which we later define as ‘galaxies’. The diffuse component in the figure consists mainly of a shock-heated hot gas around the cluster. It is more smoothly distributed, similar to the gas distribution in S0-A. Note the difference in the amount of the hot (smoothly distributed) gas. In Figure 5.1, S0-A appears considerably brighter than S0-C. While the baryon fraction in the main cluster in S0-C is very close to that in S0-A, about 50% of the gas in the cluster in S0-C is in a cooled phase, so the net amount of hot gas in S0-C is about a half of that in S0-A. In Figure 5.2 we plot the radial dependence of the enclosed baryon fractions in S0-A and S0-C. They are normalised to the global baryon fraction in the simulation. The fraction of hot gas in S0-C is also plotted in the figure. At the virial radius (indicated by a vertical bar) the baryon fraction differs only by 4% between S0-A and S0-C. An apparent difference is that the gas is more centrally concentrated in S0-C; the baryon fraction steeply rises towards the cluster centre because of the existence of a large clump of cold gas at the centre, whereas in S0-A the baryon fraction *decreases* towards the centre.

Figure 5.3 shows the radial density profiles of our clusters. For reference, the density profile of the same cluster in the S0-Dark Matter simulation (see chapter 3) is shown. The inclusion of an adiabatic gas does not have much effect on the total density profile. This agrees with the conclusion of Frenk et al. (1999) and Lewis et al. (2000). On the other hand, the effect of gas cooling on the total density profile is significant, appearing as a steepening within the central $200h^{-1}\text{kpc}$. A significant amount of gas in the cluster has already cooled, and formed a massive dense clump at the cluster centre (notice the high density at the inner most point for S0-C in Figure 5.3). The mass of the central clump is $3.8 \times 10^{13}M_{\odot}/h$, which is much larger than estimated by a simple analytic model if the clump is formed via cooling of the gas in the central region of the cluster. In fact, the mass of the central clump in S0-C corresponds to the mass of the inner 450 kpc/h hot gas in S0-A, whereas an analytic estimate of the cooling radius is $50h^{-1}\text{kpc}$ for this cluster. Using the

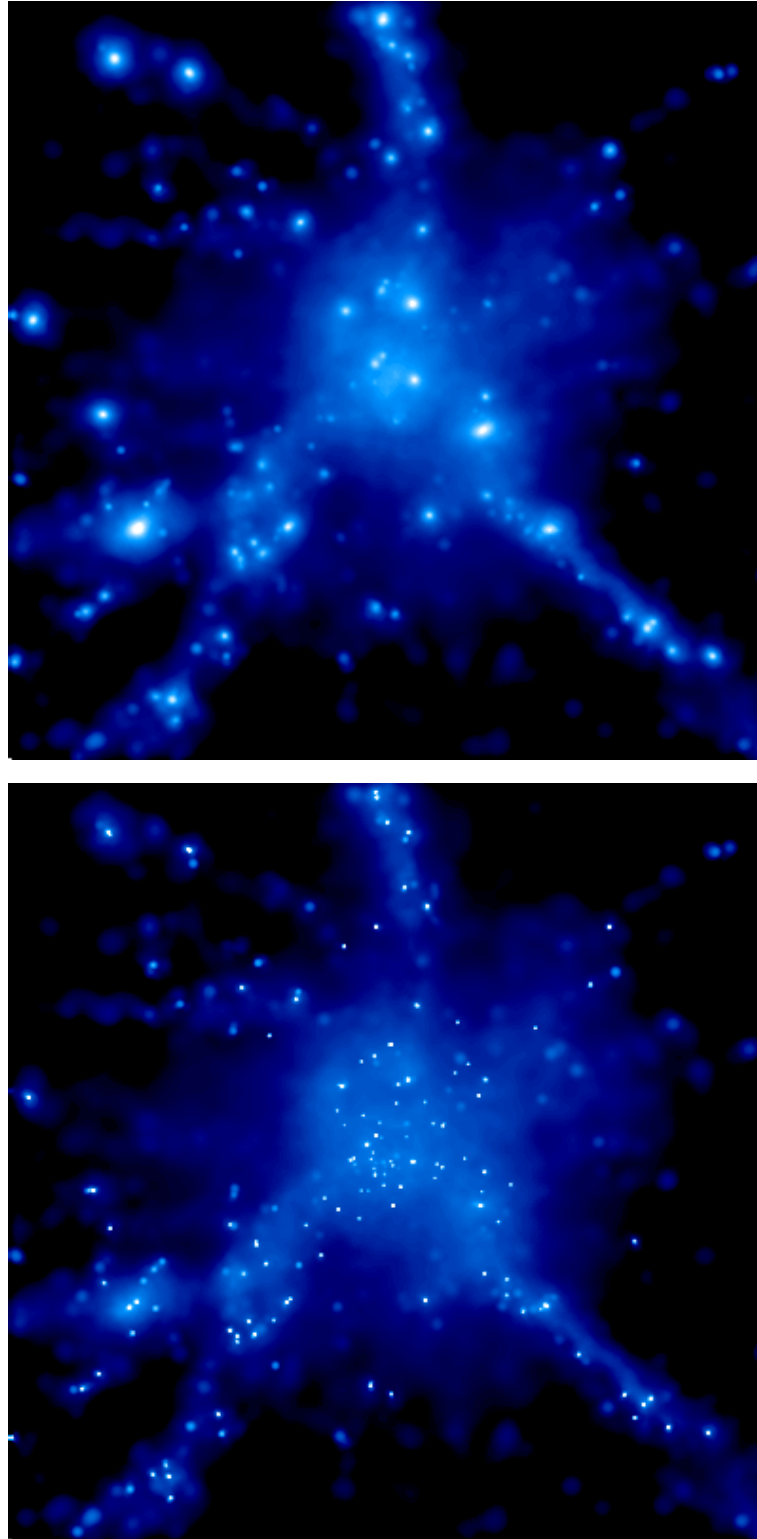


Figure 5.1 The projected gas mass distribution in the S0-cluster simulations. The adiabatic simulation (S0-A) is on the top and the cooling simulation (S0-C) is on the bottom. The region shown is a cube of $15h^{-1}\text{Mpc}$ on a side.

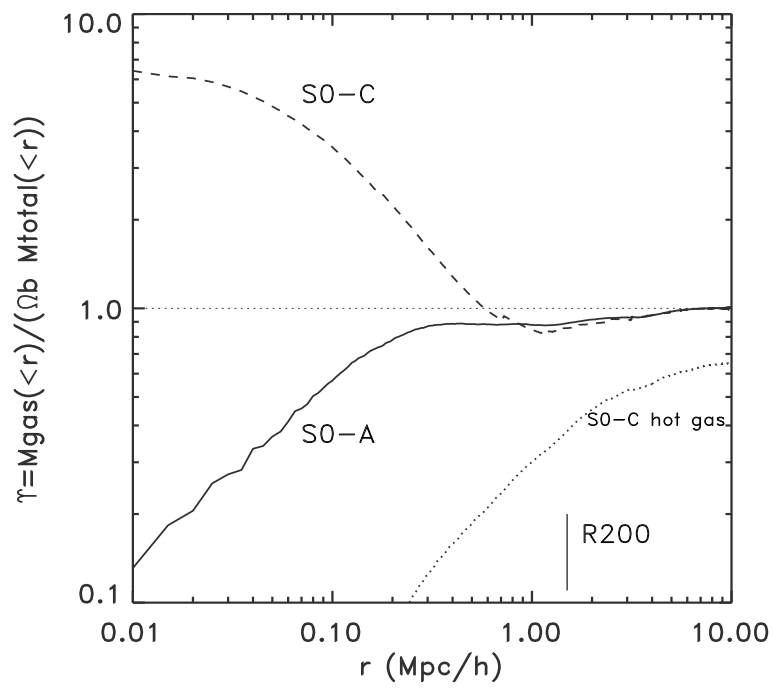


Figure 5.2 Radial dependence of the gas fraction. The quantity plotted is the enclosed gas fraction within radius r normalised to the value of the global mean in the simulation (=15%).

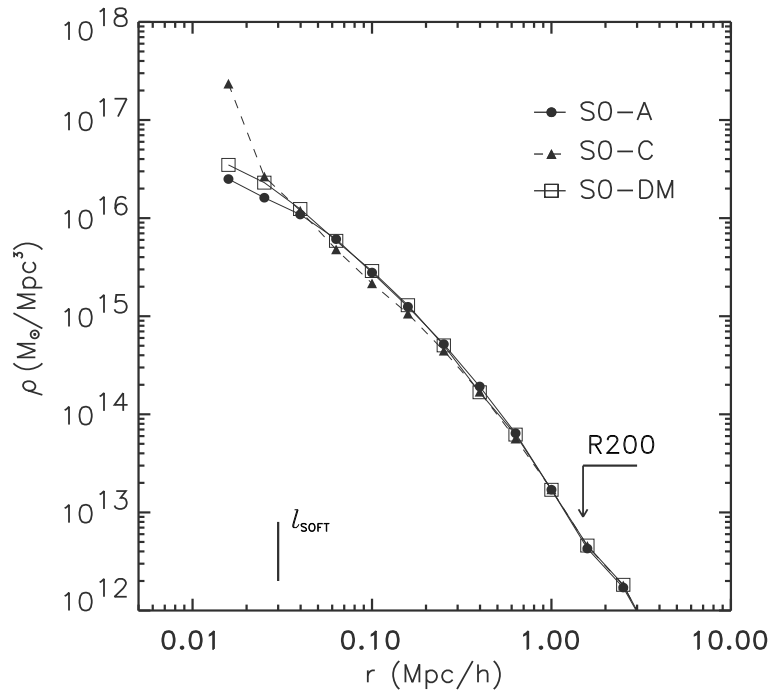


Figure 5.3 Radial density profiles for our clusters. The vertical lines indicate the gravitational softening lengths employed in the simulations.

analytic expression (given in the next section), we obtain the cooling time for the inner 450 kpc/h gas in the cluster to be 80 Gyr(!), about six times larger than the age of the universe at the present epoch. Apparently gas cooling in the SPH simulation is much more efficient than expected in the simple analytic model.

Figure 5.4 shows the distribution of gas in the thermodynamic phase plane. The cold dense gas particles are clearly seen in the narrow tail in the bottom panel. The rectangular box in the bottom panel approximately separates out the gas particles in the galaxy phase. In practice we identify galaxies by linking the cold gas particles by the standard FOF technique for a small linking length. We describe the galaxy identification in the next section.

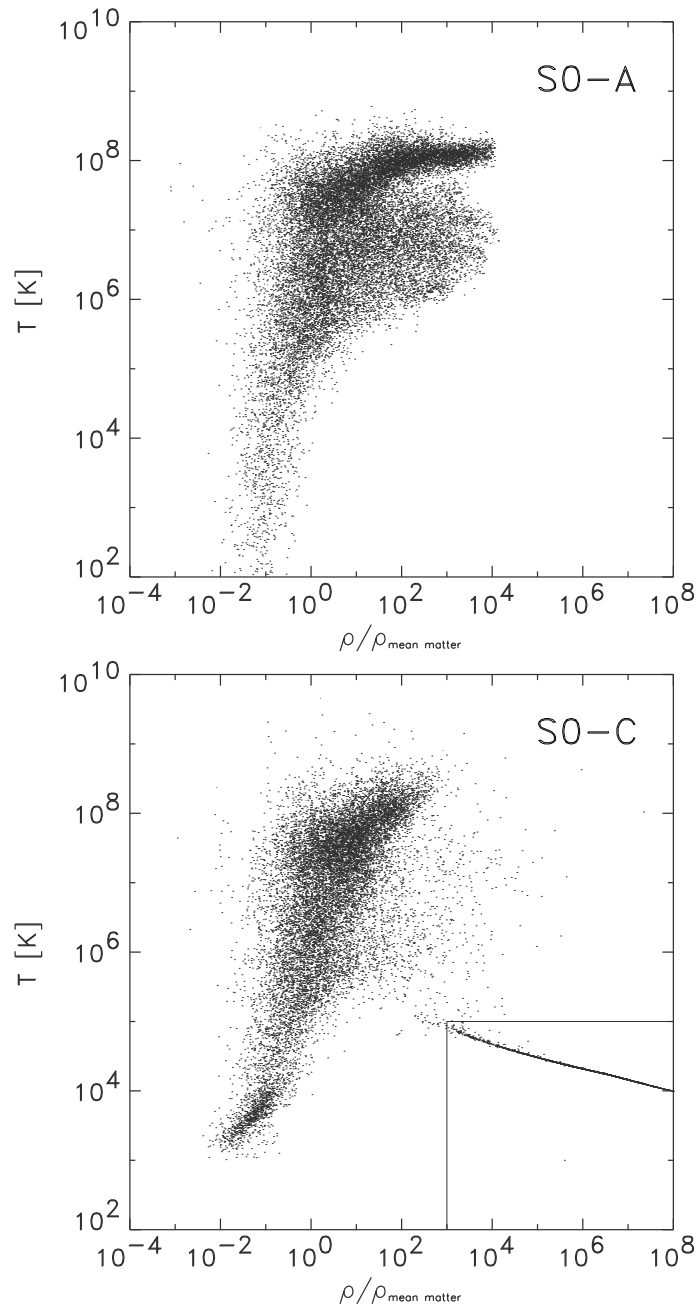


Figure 5.4 Distribution of gas in the density-temperature plane at $z=0$ in S0 simulations with adiabatic gas (S0-A, top panel) and with radiative cooling and an ionising background (S0-C, bottom panel). Densities are normalised to the mean matter density.

5.4 BARYONS IN DARK MATTER HALOS

In this section we extend our analysis for the main cluster presented in section 5.3 to all the dark halos in the simulations. Since our simulation S0-A and S0-C started from an identical initial particle distribution, the location and the mass of a dark matter halo is almost identical in the two simulations at an arbitrary output time. We locate dark halos in the two simulations by running a FOF group finder with linking parameter $b = 0.164$. In this halo-identification procedure the distribution of gas particles is not taken into account, i.e., the virial radii and the virial masses of the dark halos are computed only from the dark matter particle distribution. We define the virial radius R_{vir} as the radius of the sphere centred on the most bound particle of the FOF group having an overdensity 200 with respect to the critical density, and the virial mass M_{vir} as the enclosed mass within R_{vir} .

5.4.1 Gas mass fraction

In Figure 5.5 we plot the cold, hot, and total gas mass against the host halo mass in the S0-C simulation. Here we define the cold gas mass in a dark halo as the total mass of all the cold gas ($T < 10^5$ K) particles within the halo. Hot gas mass is computed as the total gas mass minus the cold gas mass. We plot three sets for the outputs at $z=0, 1,$ and 2 , each of which consists of four panels. In the panels in Figure 5.5, the solid line indicates the global mean baryon fraction in the simulation, $f_b=0.15$. In each set, top-left panel shows the total gas mass against the host halo mass in S0-A. A tight relation between the total gas mass and the host halo mass is clearly seen. Most of the points lie on a straight line, showing that the total gas mass is just its host halo mass times the global baryon fraction f_b . The scatter at small masses is partly due to the simulation's resolution limit. Above a mass of $1.0 \times 10^{12} M_\odot$, which corresponds to a mass of 70 particles, the scatter is substantially smaller than at the low mass end. We assign a very small value of gas mass to the halos that contain no gas particles, so that they also appear in the figure.

Similarly a good correlation is seen in the top-right panels, which show the total gas mass in S0-C. It is worth noting that the measured total gas mass is slightly higher in S0-C than in S0-A. When the gas in a halo cools and forms a dense clump, pressure balance is lost and the ambient hot gas drifts inward

until it arrives at pressure equilibrium again. This process, together with a steep gravitational potential produced by the central massive galaxy, makes dark halos in S0-C draw more gas within the virial radii than in S0-A. Bottom-left and bottom-right panels show the hot gas mass and the cold gas mass, respectively, against the halo mass. From the figures for three outputs ($z=0, 1, 2$), it can be inferred that the cold gas mass to hot gas mass ratio becomes progressively higher at lower redshift. This indicates that in our simulation which does not include any feedback mechanism, the gas in halos continuously cools over the evolution time scale of the halos. Katz & White (1993; see also Evrard, Summers & Davis 1995; Sugihara & Ostriker 1998) argued that hydrodynamic simulations without any implementation of feedback produce an unrealistically high fraction of cooled gas. Their work was followed by Lewis et al. (2000) and Pearce et al. (2001), confirming that the cold gas fraction increases with increasing resolution. In our simulation, the cold gas fraction for the main cluster in S0-C is about 50% (see section 5.3), which is already far too high to be compatible with observations (Pearce et al. 2001). Since our aim is to compare the evolution of cooling gas in the SPH simulation and in the semi-analytic modelling with star formation and feedback suppressed, this “cooling catastrophe” problem is not relevant for our analysis.

5.4.2 Galaxies in the SPH simulation

In the S0-C simulation, we define the cold, dense clumps of gas as galaxies. We locate these galaxies by running a FOF group finder for gas particles with a very small linking parameter, $b = 0.0164$. In this way the dense gas clumps are easily separated into discrete objects. We set the minimum number of particles to be 10, corresponding to minimum mass of $2.1 \times 10^{10} h^{-1} M_{\odot}$. In the following these objects are referred to as SPH-galaxies in contrast to SAM-galaxies in the semi-analytic model. We define the mass of an SPH galaxy simply as the mass of the particles in the FOF group.

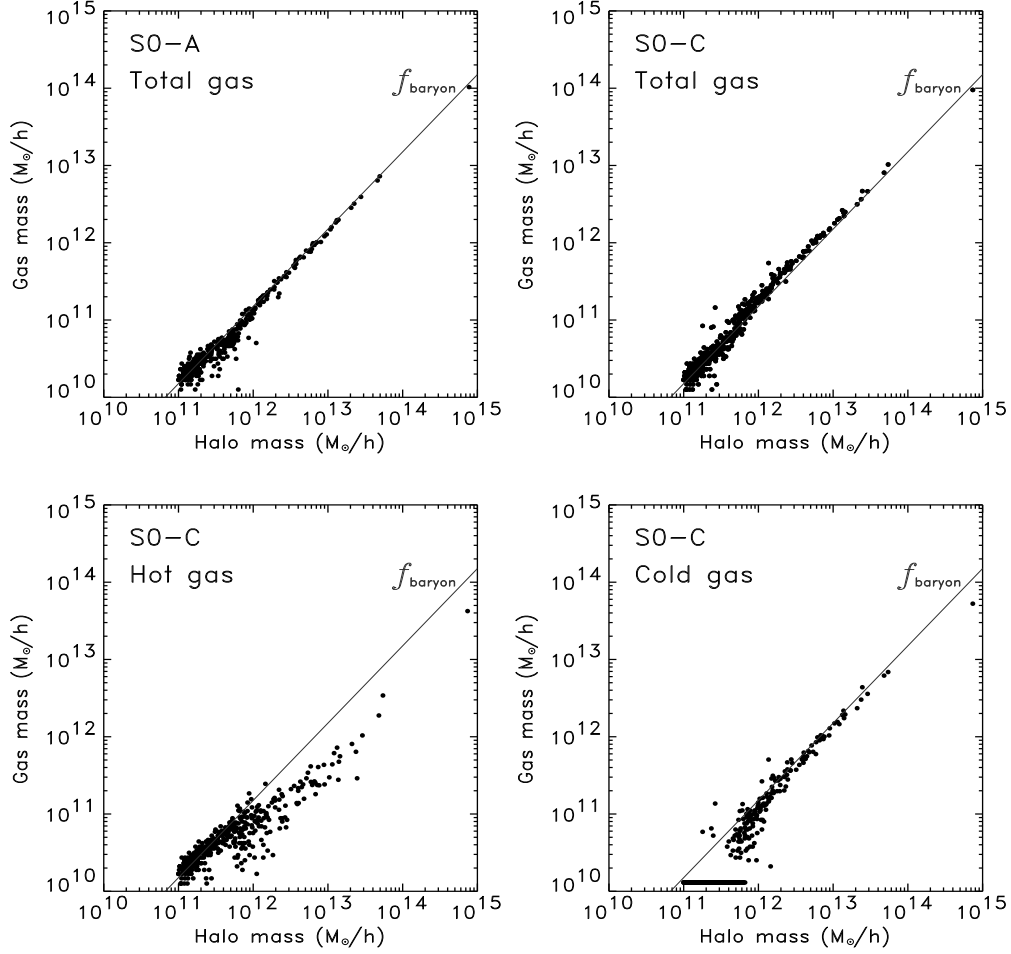
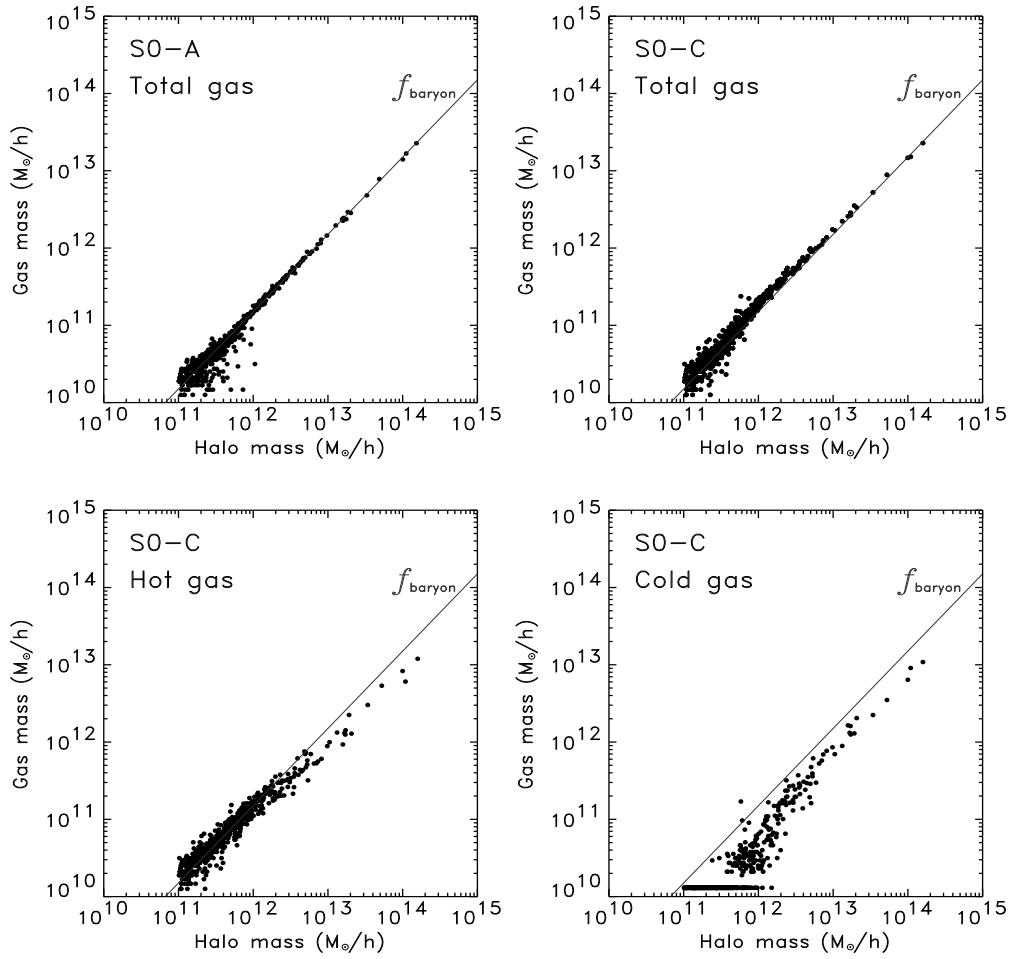
$$z=0$$


Figure 5.5 We plot the total gas mass in S0-A (top-left), the total gas mass in S0-C (top-right), the hot gas mass in S0-C (bottom-left), and the cold gas mass in S0-C (bottom-right) against the halo mass. The grey solid line indicate the global baryon fraction. If a dark halo is empty in cold gas, we assign a very small value instead of zero as corresponding cold gas mass, so that those halos also appear in the figure.

$z=1$ Figure 5.5 - *continued*.

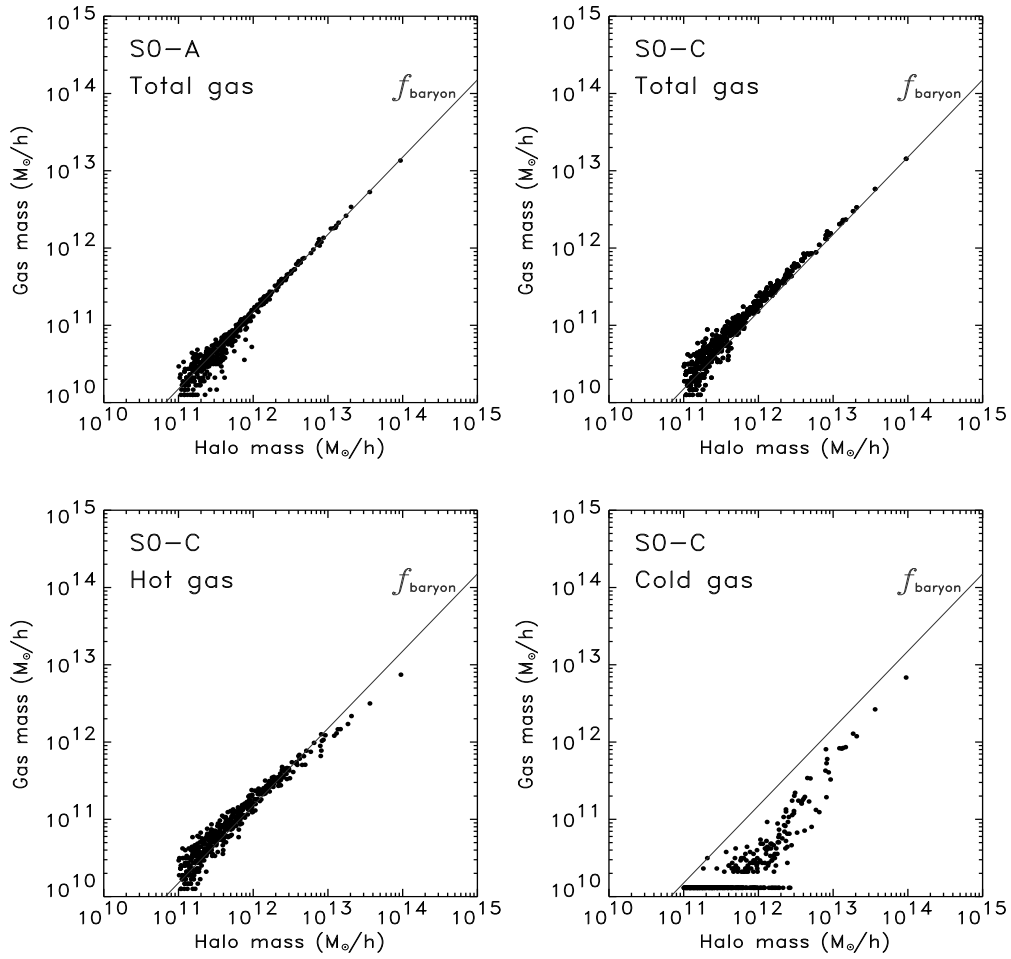
$z=2$ 

Figure 5.5 -continued.

5.5 SEMI-ANALYTIC MODELLING OF GALAXY FORMATION

In the semi-analytic models in Kauffmann et al. (1999) and Springel et al. (2001), outputs of N -body simulations are used to follow the evolution and formation of dark matter halos. The merging process of the halos is realized in the simulation, and some physically motivated simple rules are applied to model the dynamics and evolution of the gas in the halos. For each dark halo in the simulation outputs, we assign among others the following halo properties: the virial radius R_{vir} , the virial mass M_{vir} , and the circular velocity $V_{\text{vir}}^2 = GM_{\text{vir}}/R_{\text{vir}}$.

5.5.1 Gas cooling

Gas cooling is modelled as in White & Frenk (1991). We assume that the hot gas within a dark halo is distributed like an isothermal sphere with density profile ρ_g . The local cooling time of the gas, t_{cool} , can be defined as the ratio of the specific thermal energy content of the gas to the cooling rate per unit volume:

$$t_{\text{cool}}(r) = \frac{3}{2} \frac{kT\rho_g}{\bar{\mu}m_p n_e^2(r)\Lambda(T, Z)}, \quad (5.1)$$

where $\bar{\mu}$ is the mean molecular weight, m_p is the proton mass, n_e is the electron number density, T is the gas temperature which we approximate with the virial temperature of the halo $T = 35.9(V_{\text{vir}}/\text{kms}^{-1})^2$ K, and $\Lambda(T, Z)$ is the cooling rate. We employ the cooling functions in Sutherland & Dopita (1993), as in our SPH simulations.

We define the cooling radius r_{cool} such that the cooling time at this radius is equal to the time for which the halo has been able to cool quasi-statistically. We approximate this time with the halo's dynamical time $R_{\text{vir}}/V_{\text{vir}}$.

5.5.2 Stripped down semi-analytic model

Our SPH simulations do not include star formation and subsequent supernova feedback. In order to make a direct comparison with the simulations, we construct a 'stripped down' version of the semi-analytic modelling. In the stripped-down model, the star formation and feedback are switched off, and the cooling cut-off for halos with circular velocity larger than 350 km/sec employed in the semi-analytic models in Springel et al. (2001) is *not* implemented. In

principle, the cooling rate strongly depends on the metallicity of the gas Z . However, as star formation is suppressed in our stripped-down semi-analytic model, the gas does not enrich with metals but stays at primordial metallicity. Therefore the primordial cooling functions are used which is again consistent with what is done in the SPH simulations.

To further approximate the two methods we artificially reduce the resolution of the semi-analytic model by allowing gas to cool only in halos with more than a certain threshold number of particles, N_{res} . This threshold number is determined by carrying out the following experiment. We found that, for small N_{res} , there are many SAM-galaxies whose host halos do not contain any SPH-galaxy. Starting from $N_{\text{res}} = 32$, we progressively increase the threshold number. We then look for the best value for N_{res} such that there are almost equal number of SAM-galaxies that have no SPH counterpart and SPH-galaxies that have no SAM counterpart. We found that fixing $N_{\text{res}} = 56$ satisfies the above condition. We therefore take this value as the *effective resolution* of our SPH cooling simulation and implement the resolution cut-off with this value in the stripped-down model. We note that for this test we turned off the merging of satellite galaxies in our semi-analytic model, so that we can trace the formation history of all the SAM galaxies and their correspondences to SPH-galaxies. For the actual analysis in the following, we let SAM satellite galaxies to merge with central galaxies as described in the next section.

5.5.3 Galaxies in the semi-analytic model

Galaxies in our stripped-down semi-analytic model do not possess any properties such as luminosity or morphological type. There are basically only two populations of galaxies. In our model, each dark halo carries exactly one *central* galaxy and its position is given by the most-bound particle of the halo. Many halos have also one or more *satellite* galaxies. Satellites are galaxies that had been central galaxies in earlier outputs, but their host halos merged at some time to form a larger halo in which they now reside. Satellite galaxies are assumed to merge with the central galaxy in a time characterised by the dynamical friction time. In our implementation, only the central galaxy is supplied with additional gas that cools within the halo, hence the mass of a satellite galaxy is kept constant.

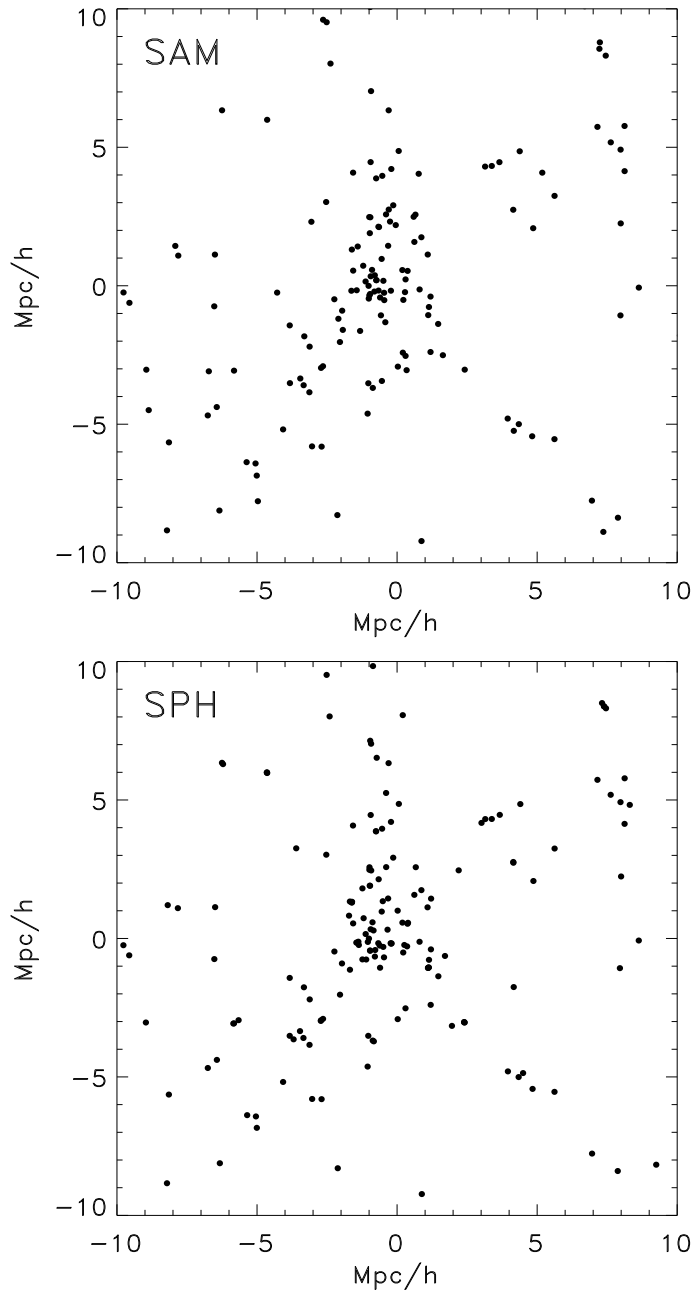


Figure 5.6 Distribution of SAM-galaxies (top) and SPH-galaxies (bottom) in the S0-C simulation at $z=0$. Only galaxies with mass larger than $6 \times 10^{10} h^{-1} M_{\odot}$ are plotted in the figures. For this mass range there are 162 SAM galaxies and 178 SPH galaxies.

5.6 OBJECT-BY-OBJECT BASIS COMPARISON

In the introduction we raised an interesting question: do the semi-analytic modelling and the SPH simulation produce a consistent result for *individual* objects? We shall now address this question by comparing the outputs from the two different models. We first compare the masses of the central galaxies in the two models. Identification of central galaxies is automatically done in our semi-analytic model as described in section 5.5, whereas locating central galaxies in the SPH simulation is not without subtleties. For simplicity, we take the most massive SPH-galaxy within a halo as the central galaxy.

The top panels in Figure 5.7 shows the mass comparison for the central SAM- and SPH-galaxies. The solid line in each plot indicates a perfect linear relation. We plot also the galaxies which find no counterpart in host halos, by assigning a small value for the counterpart's mass instead of zero. At $z=0$, the SPH-galaxy mass and the SAM-galaxy mass are closely related. There are only a few galaxies that significantly deviate from the perfect relation. However, there is a systematic deviation from perfect agreement on large mass scales. The difference is about a factor of two in mass; apparently the semi-analytic model predicts a 50% smaller mass of cooled gas within each halo than the SPH simulation. The deviation is also seen at higher redshifts, although the scatter is so large that the deviation is not characterised by a constant factor.

The reasonably good relation between the SAM-galaxy mass and the SPH-galaxy mass over a wide mass range suggests that the semi-analytic model and the SPH simulation predict a consistent behaviour of the gas in dark matter halos. On the other hand, the trend that the semi-analytic model produces a smaller amount of cold gas within a halo may indicate either that the cooling radius in the semi-analytic model is estimated to be somewhat too small, or that the assumption of quasi-static cooling is not valid. It is also possible that the SPH simulation *over*-estimates the cooling rate. There are various numerical issues which may induce over-cooling in the SPH simulation, such as improper density estimate near dense clump due to the smoothing. Such effects might have caused, singly or jointly, the gas to cool too rapidly in the dense regions. We note also that the choice of the linking parameter in group-finding is arbitrary to some extent. In principle, increasing the linking parameter results in more mass in galaxies, as more particles are joined into groups. We checked how increasing (or decreasing) the linking parameter can

affect the result by running a FOF groupfinder for gas particles with linking parameter $b=0.05$. In Figure 5.7 we plot the mass function of the SPH-galaxies identified both with $b=0.0164$ and with $b = 0.05$. The mass function appears fairly insensitive to the value of b . Thus the discrepancy in galaxy mass between the SPH simulation and the semi-analytic model cannot be attributed to the choice of the linking parameter.

We made the mass comparison also for satellite galaxies. The results are shown in the bottom panels in Figure 5.7. For satellite galaxies, SAM galaxy - SPH galaxy matching is much more complicated than for central galaxies. Their relative positions within a halo need not correspond any more. In order to make sure which SAM-galaxy corresponds to a SPH-galaxy, we trace the formation history of each satellite galaxy. For a satellite galaxy marked in an output of the semi-analytic modelling, say at redshift z_1 , we keep track of its index in earlier outputs until we find the time when the satellite galaxy was last a central galaxy. Let us denote this time z_2 . (Recall that, in our semi-analytic model, a central galaxy becomes a satellite when its host halo merges with a larger halo. Thus all the satellite galaxies were central galaxies at some earlier time.) In the output at redshift z_2 , we look for a SPH-galaxy which resides in the host halo of the target SAM-galaxy. A problem arises in this matching. There are some dark matter halos which are empty in cold gas and hence do not host any SPH-galaxy. The opposite case can also be found, because we set an artificial resolution limit in our stripped-down semi-analytic model as described in section 5.5.2. In such cases, we assign a small value as a fiducial mass to the “missing” galaxies. We found 77 SAM satellite galaxies with no SPH counterpart in their host halos at z_2 . We see them in the figure as the points at a very low mass.

Once a central SPH-galaxy is found within the same halo, we trace its merging history in the SPH simulation, this time forward in time, and tag its descendent SPH galaxy at z_1 as the counterpart of the marked satellite SAM-galaxy. By this procedure, 33 galaxies among 128 SAM satellite galaxies at $z=0$ find their counterpart SPH-galaxies. These galaxies are plotted as filled diamonds in Figure 5.7. For 18 satellite galaxies, their counterpart are found at z_2 but the descendents are lost at some later time, due to either evaporation or disruption of the small clumps which we identified as galaxies. We plot these galaxies as open circles in Figure 5.7. Note that for these galaxies, we plot their masses at z_2 , which differs from one galaxy to another.

In the SPH simulation output at $z=0$, there are 359 SPH-galaxies, of which 216 are the central galaxies. The remaining 143 galaxies are satellites or *field* galaxies that do not reside within any dark halo. We have found counterpart

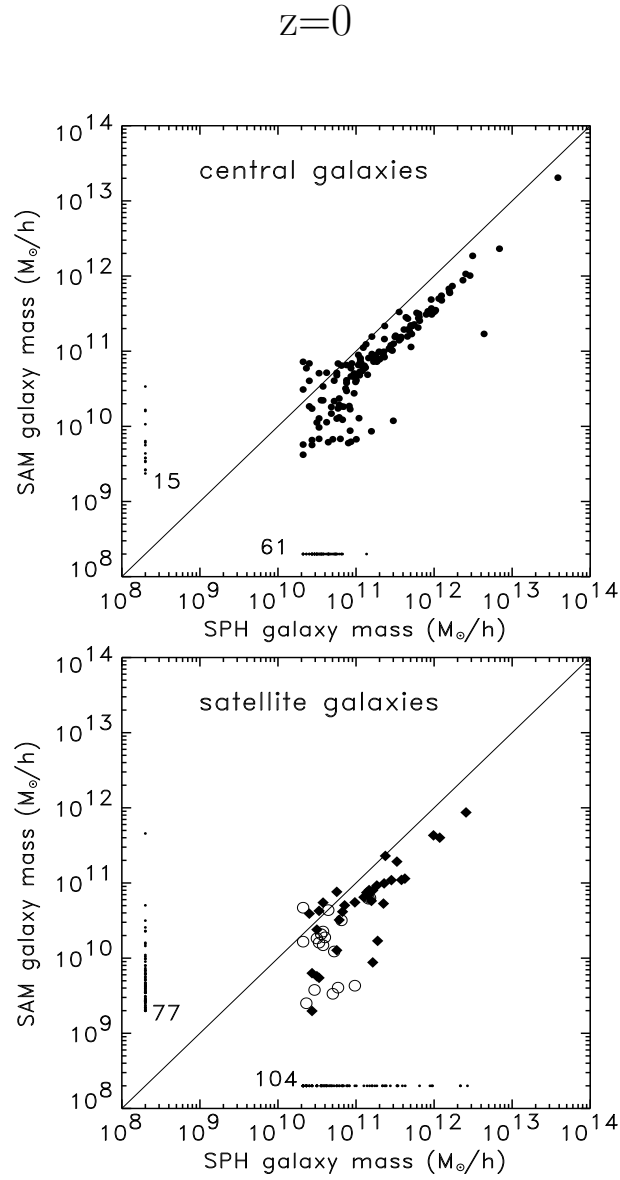


Figure 5.7 The SAM-galaxy mass is plotted against the SPH-galaxy mass for central galaxies (top) and for satellite galaxies (bottom). If a dark halo hosts a SAM(SPH) central galaxy but no SPH(SAM) galaxy, we assign a very small value instead of zero as corresponding SPH(SAM) galaxy mass, so that those galaxies also appear in the figure. The number of such galaxies is given beside the points at very low mass. For satellite galaxies, we use two different symbols: filled diamonds are for those which find a counterpart at time z_1 (see the text) and open circles are for those which find a counterpart at time z_2 but their descendent SPH galaxies are lost before z_1 . Thus open circles indicate the masses at z_2 , which differs from one galaxy to another.

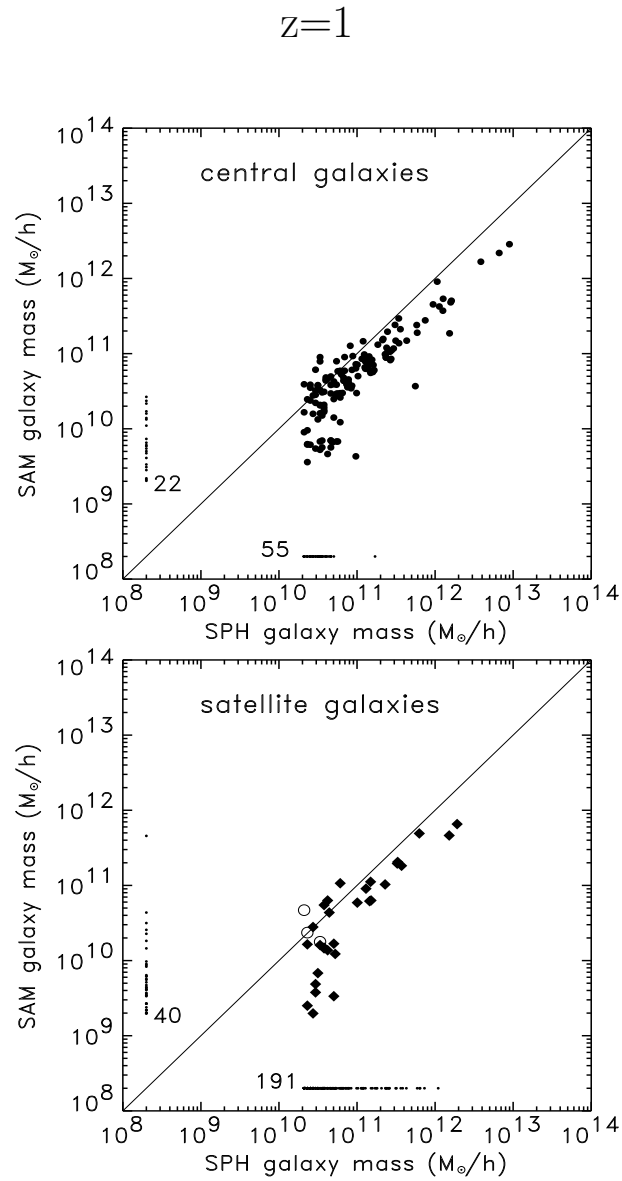


Figure 5.6 -continued

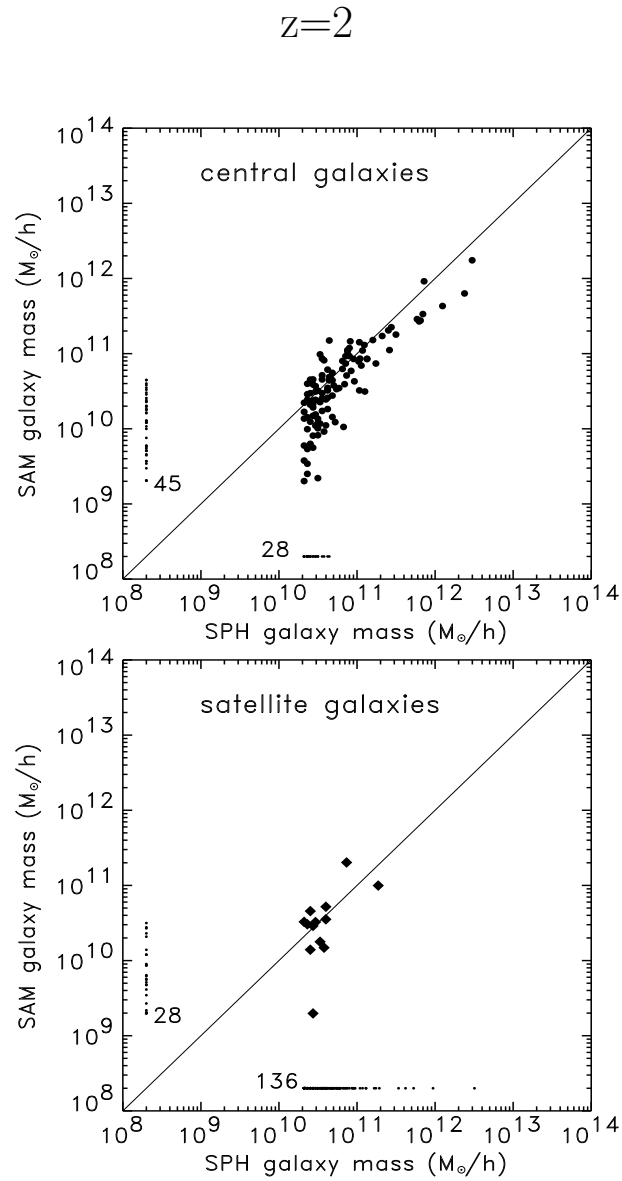


Figure 5.6 -continued

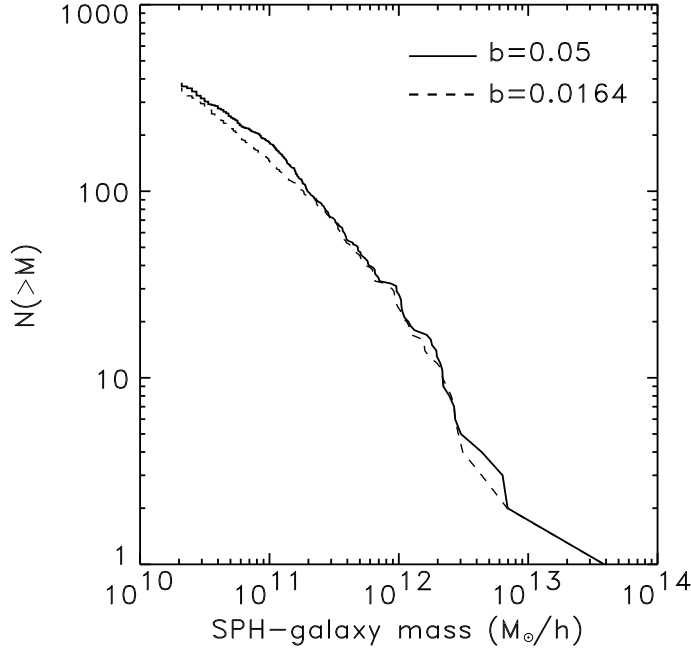


Figure 5.7 The cumulative number of SPH-galaxies as a function of the galaxy mass at $z=0$.

SAM-galaxies for 155 central and 33 satellite SPH-galaxies. Almost all of the rest can be matched to SAM-galaxies if the resolution parameter N_{res} is lowered to the effective resolution limit of the full semi-analytic model.

It is interesting that there are many more SPH satellites with no SAM counterpart at higher redshift. In fact, there are 136 SPH satellites with no SAM counterpart at $z=2$, whereas only 28 SAM satellites are with no SPH counterpart. This may reflect the time-dependence of the effective resolution of the SPH simulation.

In the mass comparison plots in Figure 5.7, the mass difference by a factor of about two is seen also for satellite galaxies. An important question is *why* such a mass discrepancy exists, and it is interesting to test whether the discrepancy can be eliminated by changing one or more parameters in the semi-analytic model. We shall now address this question by studying various possibilities.

In practice, it is straightforward to lessen the mass difference by forcing more gas in halos to cool in the semi-analytic model. We achieve this by increasing the coefficient of the cooling rate. Namely, we multiply the cooling rate by a constant factor. Let us denote the factor as C_{cool} . The value $C_{\text{cool}} = 1$ is the standard case adopted so far and in Springel et al. (2001). We applied

our semi-analytic scheme to the same simulation outputs by progressively increasing the factor to be $C_{\text{cool}} = 2, 4,$ and 10 .

Figure 5.8 clearly shows that increasing the cooling efficiency produces more massive SAM-galaxies, as expected. Note, however, that the increase in C_{cool} by a factor of ten does not simply result in ten times larger masses for individual galaxies. This is because the supply of hot gas in a halo is limited approximately by the halo mass times the global baryon fraction, and because larger objects are formed not only by quasi-static cooling of gas but also via successive mergers of small objects.

From Figure 5.8, one might have inferred that in order for the semi-analytic model to predict the same amount of cold gas as in the SPH simulation, cooling must be about a factor of four or more efficient. One must be careful in interpreting the above result, because there are other possibilities that the cooling in the SPH simulation is too efficient for some numerical reason. In fact, over-cooling induced by cold dense gas clumps in SPH simulations is a well known problem (Ritchie & Thomas 2000). Although the degree of the effect is unclear and will probably differ from one code to another, it is likely to have happened also in our simulations since we did not implement special treatments to avoid over-estimating the local density near cold gas particles (see, e.g. Pearce et al. 2000).

We can indeed check the cooled gas mass in the simulation against an analytic estimate. To do so, we directly measure the mass increase of the central galaxy of the main cluster in the SPH simulation from $z = 0.2$ to $z = 0$. We measure the total mass of gas which was hot and resided in the main cluster in an earlier output, but has become cold. This amount should give an accurate measure for the cooling rate as it does not include the mass increase due to merging of satellite galaxies onto the central galaxy. The expected mass of newly cooled gas can also be computed analytically by assuming that the hot gas is distributed isothermally in the host halo, just as in the semi-analytic model. Figure 5.9 shows the predicted and actual mass increase of the central galaxy in the SPH simulation. The dashed line in the figure is the actual mass increase assigned in the semi-analytic model. Recall that the analytic estimate (dotted line) is computed *for the SPH simulation*. In the SPH simulation about 50% of the total baryons are in the hot gas phase in the main cluster over the redshift range $0 < z < 0.2$. We have used this value to compute the newly cooled gas mass. Thus the difference between the estimate (dotted line in Figure 5.9) and the cooled gas mass in the semi-analytic model (dashed line) is due to the difference in the fraction of hot gas in the main cluster. The semi-analytic model predicts about 75% of the total baryons to

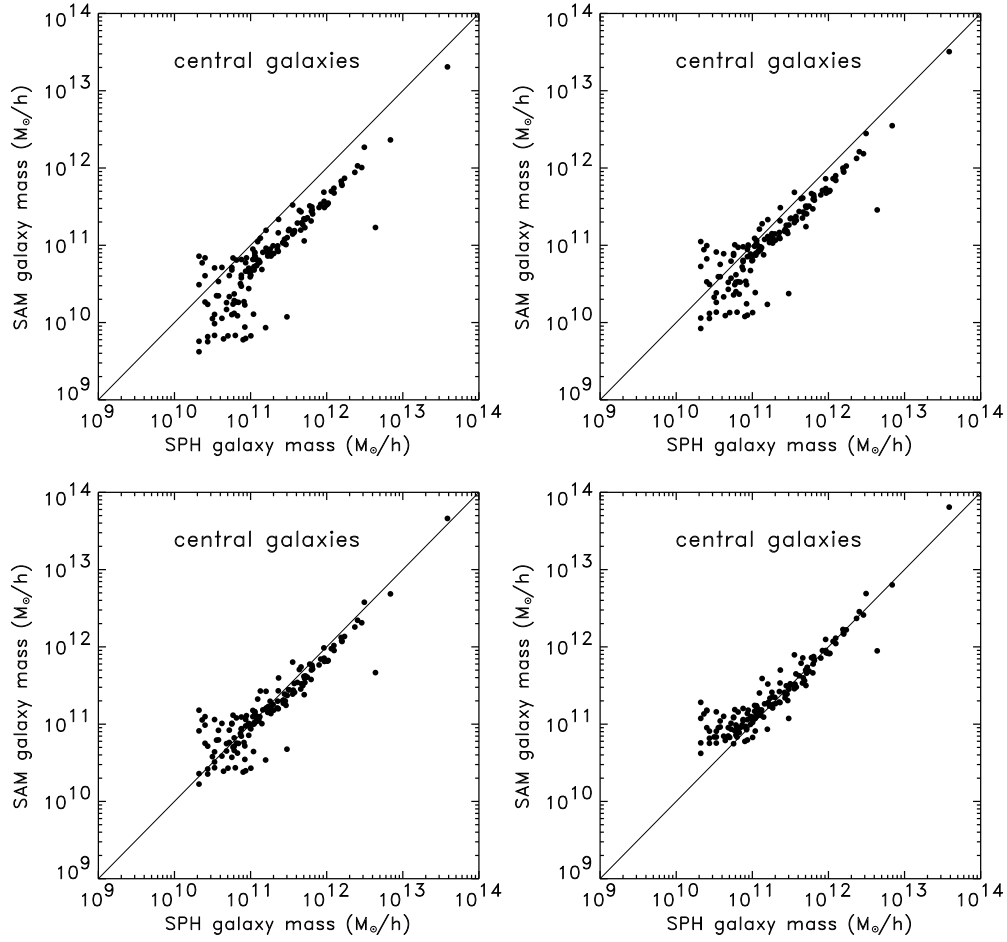


Figure 5.8 The mass comparison for the central galaxies at $z=0$. We progressively increase the coefficient of the cooling rate in the semi-analytic model from 1 (top-left) to 2 (top-right), 4 (bottom-left), and 10 (bottom-right).

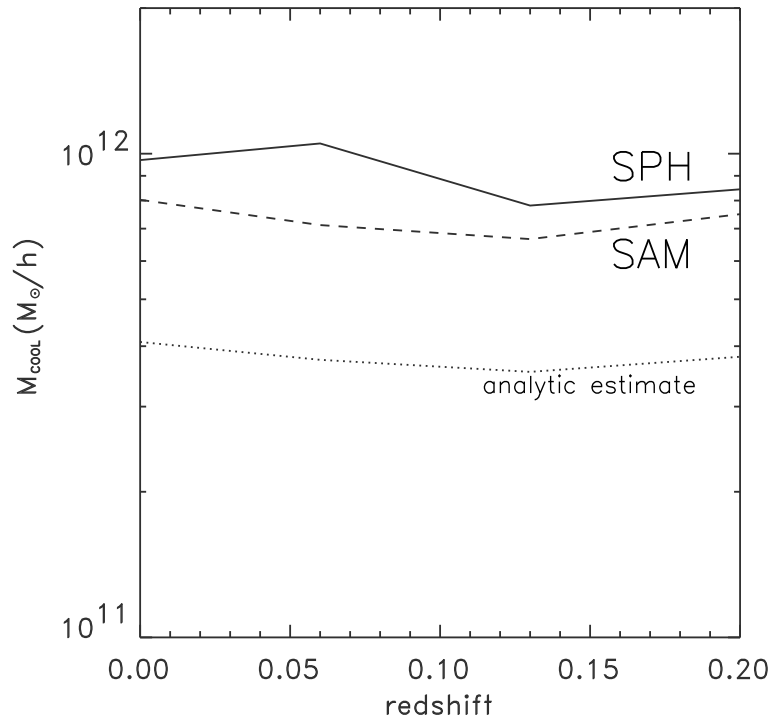


Figure 5.9 The mass increase of the central galaxy in the main cluster.

be in the hot gas phase in the cluster in this redshift range.

Figure 5.9 clearly shows that in the SPH simulation, gas cooling is a factor of two more efficient than expected. The above mentioned over-cooling problem in SPH is likely to be the main cause of this efficient cooling. There may be another reasons in that the analytic estimate is based on the assumption of spherical symmetry and isothermality to the hot gas in the cluster. Although reasonable, these assumptions are invalid in detail in the central region of the cluster where satellite galaxies are accreted onto the central galaxy.

5.7 SUMMARY AND DISCUSSION

We have studied gas cooling associated with galaxy formation using a set of hydrodynamic simulations. We explicitly calculated the evolution of cooling gas in galaxy clusters in the semi-analytic model as well as in the numerical simulations. Comparisons of an adiabatic gas simulation and a simulation with radiative cooling showed that the gas cooling can significantly affect the distribution of *hot* gas and even the distribution of the total material in galaxy clusters.

Assumptions commonly made in the semi-analytic models of galaxy formation were tested against the numerical simulations. We compared the masses of individual galaxies in the two models, both for central galaxies and satellite galaxies by following their formation history explicitly. We found a reasonable agreement between the results of the two cases, but also systematic differences. While the assumptions, the so-called “recipe” in the semi-analytic model were validated as a good approximation, the quantitative studies in the present chapter suggest that the semi-analytic model predicts a smaller amount of gas cooled in dark halos than the numerical simulations. We investigated various possibilities which might have caused the discrepancy. We found that increasing the cooling efficiency in the semi-analytic model can improve the agreement in the galaxy mass, but only if the efficiency is increased by an unrealistically large factor. This may, in turn, suggest that the cooling in the SPH simulation is too efficient, as has often been discussed in the literature (e.g. Pearce et al. 2000). We indeed found such a feature in the simulation by comparing the measured cooled gas mass against an analytic estimate. Adequate treatment of large density gradients in the SPH simulation may substantially improve this behaviour (Marri 2001, private communication). In future work we will clarify the degree of the over-cooling by employing such multi-phase treatments in SPH simulations.

Overall our study shows a reasonable consistency between the hydrodynamic simulation and the semi-analytic model at an individual object level. Although quantitative differences exist, they are mostly due to well known features in the model and in the simulation, and thus can be easily checked by further simulations. Such work should then be very useful both for refining the semi-analytic models and for improving the hydrodynamics implementation in the SPH simulations.

CHAPTER 6

Concluding remarks

6.1 SUMMARY AND CONCLUSIONS

In this work various aspects of the currently popular Cold Dark Matter models were studied.

In Chapter 2, I addressed a problem persistent in cosmology since the discovery of the periodic distribution of galaxies in a deep pencil-beam survey by Broadhurst, Ellis, Koo & Szalay in 1990. The Hubble Volume Simulations made it possible for the first time to test directly whether such apparent periodic structures should be found in a CDM universe. In order to make ‘galaxy’ catalogues from the simulation output, biasing of galaxies was quantitatively studied and a simple biasing prescription was applied so that the ‘galaxy’ distribution resembles the distribution of galaxies in the nearby Universe. I created a large number of dynamically consistent realisations of the mock pencil-beam redshift survey and applied various statistical tests, to compare them with the Broadhurst et al. data. From the results obtained from the power spectrum analysis, I concluded that the probability of obtaining a sample as regular as the Broadhurst et al. observation is well below 10^{-3} in CDM universes. It is, however, too early to come to the definite conclusion that the CDM models are incompatible with the observed periodicity. Two other deep redshift surveys by Bellanger & de Lapparent (1995) and by Cohen et al. (1999) have found no evidence for periodic structure on the $\sim 130h^{-1}\text{Mpc}$ scale. Therefore it may be that the Broadhurst et al. data are just a fluke, probing a particular direction where galaxies are by chance found to be regularly distributed. As our result now gives an *a priori* probability for the kind of periodicity found by Broadhurst et al., future redshift surveys can easily test the CDM models. In the near future the VIRMOS Deep Survey (Le Fèvre et al. 1998) will probe the distribution of galaxies in the range $0.3 \leq z \leq 1$ and will provide, together with the large volume 2dF and Sloan surveys, much larger and more complete samples.

In recent years evidence has accumulated that the standard cosmological models based on cold collisionless dark matter may conflict with observations on galactic and sub-galactic scales. Studies presented in chapter 3 were motivated by a suggestion that an explanation for the discrepancy should be sought in fundamental physics. I studied the viability of a recently proposed alternative model in which cold dark matter interacts strongly with itself. Specifically I investigated how such modifications alter the internal structure of nonlinear

objects (“dark halos”), by carrying out a set of large numerical simulations of the formation of galaxy clusters. I showed the result for an extreme case in which the dark matter behaves as a “fluid” in the large scattering cross-section limit. Through mergers to build up larger objects, such a “fluid” of dark matter produces a cluster which is more spherical and has a more singular central density profile than in the collisionless case. I then showed that in the intermediate regime, where the CDM mean free path is comparable to the sizes of halos, the dark matter self-interaction makes the cluster rounder and less dense in the centre, and also reduces the subhalo abundance. These *plausible* features for dwarf galaxies, however, appear to be less favoured on larger scales. An extension of the work led by Massimo Meneghetti (2001) showed that dark matter self-interaction has a massive impact on clusters’ ability to produce strongly lensed images of background galaxies. A few collisions per particle per Hubble time at the halo centre can substantially reduce this ability. Thus gravitational lensing provides a useful probe of the matter distribution in galaxy clusters and offers a way to limit certain intrinsic properties of the dark matter particles.

In chapter 4, I studied secondary CMB anisotropies due to the Sunyaev-Zel’dovich effect by clusters of galaxies. I presented a detailed analysis of CMB temperature fluctuations and discussed non-Gaussian features in the CMB temperature map caused by the Sunyaev-Zel’dovich effect. An analytic model based on the “halo-approach” was developed to predict the distribution of the peak height in the temperature fluctuations, and the model prediction was tested against the estimates from a large numerical simulation. I showed that the model accurately predicts the distribution of the peak height. Since the model prediction can be made if the initial density fluctuation is specified, it will be possible to put a constraint on the initial matter distribution within the framework of the standard Gaussian models. In the latter part of chapter 4, I created simulated maps of the SZ effect by a commonly used stacking technique. The angular power spectra of the thermal and kinematic effects were computed and compared to other published analytical and numerical results. Although the simulation employs only dark matter particles, the large simulation box has a number of advantages over published hydrodynamical simulations and makes it possible to create SZ maps for a wide patch of 3.4×3.4 square-degree. Such realistic maps will be very useful to study further the properties of secondary CMB anisotropies using higher order statistics.

In chapter 5, I studied gas cooling and its role in galaxy formation. Among the complex physical processes involved in galaxy formation, gas cooling is probably the most important, and is a relatively well understood process. By

carrying out a set of hydrodynamic simulations I explicitly showed how the gas behaves at various stages of the formation of galaxy clusters. Assumptions commonly made in the semi-analytic models of galaxy formation were discussed based on the results of the numerical simulations. I compared the masses of individual galaxies in the two different models, both for central galaxies and satellite galaxies by following their formation history. I found a reasonable agreement between the results in the two cases, but also systematic differences. While the assumptions, the so-called “recipes” in the semi-analytic models were validated as a good approximation, the quantitative studies in this chapter showed that the semi-analytic models predict a smaller amount of gas cooled in dark halos than the direct numerical simulations. Further simulations will clarify the reason for the discrepancy.

6.2 FUTURE PROSPECT

The coming ten years will definitely be a golden age of cosmology. Data from the two ongoing wide-field redshift surveys, the 2dF and the Sloan surveys, will substantially improve the statistics of the distribution of galaxies and quasars. Clustering properties of high-redshift objects determined by these large surveys will put strong constraints on theoretical models of structure formation. Two planned satellite missions, the European *Planck* and NASA’s *MAP*, will provide us with a considerable amount of information on CMB temperature fluctuations, which will enable us to determine the fundamental cosmological parameters with excellent precision. On completion of these redshift surveys and CMB experiments, about a decade from now, cosmology will become truly a *precision* science.

We naturally expect that numerical simulations will have to be more sophisticated than now. This field of research – the theory of structure formation of the universe – has met great success with the help of numerical simulations. Looking back over the past two decades, one easily sees that numerical simulations have played an important role in establishing what we now call the standard paradigm. Now and in the future, theoretical models are and will be tested against observations to a high level of accuracy using numerical simulations.

Regarding the progress in computing power, it seems that we may still expect a constant growth in the speed of computation. Without being too optimistic, I predict that, within about ten years, the first cosmological simulation will be performed with a sufficiently high resolution to resolve individual galaxies in a cosmological volume. Such “ultimate” cosmological simulations will include the major physical processes associated with galaxy formation, as well as the formation of large-scale structure governed by gravity. The computational techniques for cosmological simulations with dissipative processes are still in their infancy, so developing an efficient algorithm to incorporate radiative as well as hydrodynamical processes will be necessary.

I would like to close this thesis by making a self-inconsistent comment. A dream of numerical cosmologists is to perform a large simulation whose output is beautifully consistent with the observed, actual Universe; whereas a common desire of astronomers is to discover a new astronomical object or understand a new phenomenon which cannot be explained within standard theories. It is not trivial for me to reconcile these two desires. Certainly it would be a great pity if the Universe were really like a simulation output shown on a computer monitor. Considering these two opposing desires, I still hope that future observations reveal a completely new face of the Universe, and I expect them to make us all surprised and puzzled. I look forward to being perplexed by new observational data which are *not* consistent with my simulation outputs.

BIBLIOGRAPHY

- [1] Bahcall, N. A., *Superclusters and pencil-beam surveys - The origin of large-scale periodicity -*, ApJ, 376, 43 (1991)
- [2] Bahcall, N. A., Ostriker, J. P., Perlmutter, S., & Steihardt, P. J. *Science*, 284, 148 (1999)
- [3] Bardeen, J. M., Bond, J. R., Kaiser, N., & Szalay, A. S. *The statistics of peaks of Gaussian random fields*, ApJ, 304, 15 (1986)
- [4] Bardeen, J. M., Steinhardt, P. J., & Turner, M. S., *Spontaneous creation of almost scale-free density perturbations in an inflationary universe*, Phys. Rev. D, 28, 679 (1983)
- [5] Baugh, C. M., *The real-space correlation function measured from the APM Galaxy Survey*, MNRAS, 280, 267 (1996)
- [6] Bellanger, C. & de Lapparent, V., *Mapping the galaxy distribution at large distances*, ApJ, 455, 103 (1995)
- [7] Benson, A. J., Cole, S., Frenk, C. S., Baugh, C. M., & Lacey, C. G., *The nature of galaxy bias and clustering*, MNRAS, 311, 793 (2000)
- [8] Benson, A. J., Pearce, F. R., Frenk, C. S., Baugh, C. M., & Jenkins, A., *A comparison of semi-analytic and smoothed particle hydrodynamics galaxy formation*, MNRAS, 320, 261 (2001)
- [9] de Bernardis, P. et al., *A flat Universe from high-resolution maps of the cosmic microwave background radiation*, Nature, 404, 955 (2000)
- [10] Bertschinger, E., *The evolution of cooling flows: self-similar cooling waves*, ApJ, 340, 666 (1989)
- [11] Birkinshaw, M., *The Sunyaev-Zel'dovich effect*, Physics Reports, 310, 97 (1995)

- [12] Bode, P., Ostriker, J. P., & Turok, N., *Halo Formation in Warm Dark Matter Models*, ApJ, 556, 93 (2001)
- [13] Bond, J. R. & Efstathiou, G., *Cosmic background radiation anisotropies in universes dominated by nonbaryonic dark matter*, ApJ, 285, 45 (1984)
- [14] Bond, J. R. & Efstathiou, G., *The statistics of cosmic background radiation fluctuations*, MNRAS, 226, 655 (1987)
- [15] Bond, J. R. & Myers, S. T., *The peak patch picture of cosmic catalogs III. Application to clusters*, ApJS, 103, 63 (1987)
- [16] Bonnet, H., Mellier, Y., & Fort, B., *First detection of a gravitational weak shear at the periphery of CL 0024+1654*, ApJ, 427, 83 (1994)
- [17] Broadhurst, T. J., Ellis, R. S., Koo, D. C., & Szalay, A. S., *Large-scale distribution of galaxies at the Galactic poles*, Nature, 343, 726 (1990)
- [18] Bullock, J. S., Kolatt, T. S., Sigad, Y., Somerville, R. S., Kravtsov, A. V., Klypin, A. A., Primack, J. R., & Dekel, A., *Profiles of dark haloes: evolution, scatter and environment*, MNRAS, 321, 559 (2001)
- [19] Burkert, A., *The structure and evolution of weakly self-interacting cold dark matter halos*, ApJ, 534, L143 (2000)
- [20] Carignan, C. & Beaulieu, S., *Optical and H I studies of the "gas-rich" dwarf irregular galaxy DDO 154*, ApJ, 347, 760 (1989)
- [21] Carlson, E., D., Machacek, M. E., & Hall, L. J., *Self-interacting dark matter*, ApJ, 398, 43 (1992)
- [22] Cavaliere, A., Danese, L., & de Zotti, G., *Constraints on dynamical properties of clusters of galaxies*, Astron. Astrophys., 60, 15 (1977)
- [23] Cohen, J. G., *Clustering in the Caltech Faint Galaxy Redshift Survey*, in Mazure, A. & Le Fèvre, O. eds, *Clustering at High Redshift*, ASP Conference Series, Vol. 200, p314 (1999)
- [24] Colberg, J., *Parallel supercomputer simulations of cosmic evolution*, PhD thesis, Ludwig-Maximilian University, Munich. (1998)

- [25] Colberg, J. M., White, S. D. M., Yoshida, N., MacFarland, T. J., Jenkins, A., Frenk, C. S., Pearce, F. R., Evrard, A. E., Couchman, H. M. P., Efstathiou, G., Peacock, J. A., Thomas, P. A. (The Virgo Consortium), *Clustering of galaxy clusters in cold dark matter universes*, MNRAS, 319, 209
- [26] Cole, S. M. & Kaiser, N., *Sunyaev-Zel'dovich fluctuations in the cold dark matter scenario*, MNRAS, 233, 637 (1998)
- [27] Cole, S., Aragon-Salamanca, A., Frenk, C. S., Navarro, J., & Zepf, S. E., *A recipe for galaxy formation*, MNRAS, 271, 781 (1994)
- [28] Cole, S. M., Hatton, S. J., Weinberg, D. H., & Frenck, C. S., *Mock 2dF and SDSS galaxy redshift surveys*, MNRAS, 300, 505 (1998)
- [29] Coles, P., *Understanding recent observations of the large-scale structure of the universe*, *Nature*, 346, 446 (1990)
- [30] Coles, P. & Luccin, F., *COSMOLOGY –the origin and evolution of cosmic structure*, John Wiley & Sons, West Sussex (1997)
- [31] Copi, C. J., Schramm, D. N., & Turner, M. S., *Assessing Big-Bang nucleosynthesis*, *Phys.Rev.Lett*, 75, 3981 (1995)
- [32] Cramphorn C., *A scaling relation between the SZ decrement and the Thomson depth in clusters of galaxies*, *Astronomy Letters*, 27, 135 (2001)
- [33] Croft, R. A. C., Weinberg, D. H., Pettini, M., Hernquist, L., & Katz, N., *The power spectrum of mass fluctuations measured from the Ly-alpha forest at redshift $z=2.5$* , *ApJ*, 520, 1 (1999)
- [34] Davé, R., Spergel, D. N., Steinhardt, P. J., & Wandelt, B. D., *Halo properties in cosmological simulations of self-interacting cold dark matter*, *ApJ*, 547, 574 (2001)
- [35] Dekel, A., Blumenthal, G. R., Primack, J. R., & Stanhill, D., *Large-scale periodicity and Gaussian fluctuations*, MNRAS, 257, 715 (1992)
- [36] Dekel, A. & Lahav, O., *Stochastic Nonlinear Galaxy Biasing*, *ApJ*, 520, 24 (1999)
- [37] Diaferio, A., Nusser, A., & Sunyaev, R. A., *Large-scale motions in superclusters: their imprint in the cosmic microwave background*, *ApJ*, 533, L71 (2000)

- [38] Duari, D., Das Gupta, P., & Narlikar, J. V., *Statistical tests of peaks and periodicities in the observed redshift distribution of quasi-stellar objects*, ApJ, 384, 35 (1992)
- [39] Einasto, M., Tago, E., Jaaniste, J., Einasto, J., & Andernach, H, *The supercluster-void network I. The supercluster catalogue and large-scale distribution*, Astron. Astrophys., 123, 119 (1997)
- [40] Einstein, A., *Kosmologische Betrachtungen zur allgemeinen Relativitätstheories*, Sitzungsberichte der Preuss. Akad. Wiss. 142 (1917)
- [41] Eisenstein, D. J., Hu, W., Silk, J., & Szalay, A. S., *Can baryonic features produce the observed $100 h^{-1} \text{Mpc}$ Clustering?*, ApJ, 494, L1 (1998)
- [42] Eke, V. R., Cole, S., & Frenk, C. S., *Cluster evolution as a diagnostic for Ω* , MNRAS, 282, 263 (1996)
- [43] Eke, V. R., Navarro, J., & Frenk, C. S., *The evolution of X-ray clusters in a low-density universe* ApJ, 503, 569 (1998)
- [44] Ettori, S., Guzzo, L., & Tarenghi, M., *A study of the large-scale distribution of galaxies in the South Galactic Pole region - II. Further evidence for a preferential clustering scale ?*, MNRAS, 285, 218 (1997)
- [45] Evrard, A. E., MacFarland, T. J., Couchman, H. M. P, Colberg, J. M., Yoshida, N., White, S. D. M., Jenkins, A., Frenk, C. S., Pearce, F. R., Efstathiou, G., Peacock, J. A., Thomas, P. A., *Galaxy clusters in Hubble Volume Simulations: Sky survey populations and cosmological constraints*, submitted to ApJ, 2001
- [46] Feller, W., *An Introduction to Probability Theory and Its Applications*, Volume 2, 2nd Edition, John Wiley and Sons, New York (1971)
- [47] Le Fèvre, O., et al., *Deep redshift surveys with the VLT-VIRMOS and the NGST*, in Giuricin, G., Mezzetti, M., & Salucci, P. eds, *Observational Cosmology: The development of Galaxy Systems*, ASP Conference Series, Vol. 176, p250 (1999)
- [48] Firmani, C., D'Onghia, E., Avila-Reese, V., Chincarini, G., & Hernandez, X., *Evidence of self-interacting cold dark matter from galactic to galaxy cluster scales*, MNRAS, 315, 457 (2000)

- [49] Flores, R. A. & Primack, J. A., *Observational and theoretical constraints on singular dark matter halos*, ApJ, 427, L1 (1994)
- [50] Freese, K., *Death of stellar baryonic dark matter*, in Weiss A. et al., eds, The First Stars, Proc. MPA/ESO workshop (2000)
- [51] Frenk, C. S., *Models of large scale structure*, Physica Scripta, Vol. T36, 70 (1991)
- [52] Frenk et al., *The Santa Barbara cluster comparison project: A comparison of cosmological hydrodynamics solutions*, ApJ, 525, 554 (1999)
- [53] Gamow, G., *Expanding universe and the origin of elements*, Physics Review, 70, 572 (1946)
- [54] Ghigna, S., Moore, B., Governato, F., Lake, G., Quinn T., & Stadel, J., *Density profiles and substructure of dark matter halos: Converging results at ultra-high numerical resolution*, ApJ, 544, 616 (2000)
- [55] Gnedin, N. Y. & Jaffe, A., *Secondary cosmic microwave background anisotropies from cosmological reionization*, ApJ, 551, 3 (2001)
- [56] Gottlöber, S., Klypin, A. A., & Kravtsov, A. V., *Halo evolution in a cosmological environment*, in Giuricin G et al., eds., Observational Cosmology (1999)
- [57] Gradwohl, B.-A., & Friemann, J. A., *Dark matter, long-range forces, and large-scale structure*, ApJ, 398, 407 (1992)
- [58] Gruzinov, A. V. & Hu, W., *Secondary cosmic microwave background anisotropies in a universe reionized in patches*, ApJ, 508, 435 (1998)
- [59] Gunn, J. E., Longair, M. S., & Rees, M. J., *Observational cosmology*, Sauverny: Observatoire de Geneve (1978)
- [60] Guth, A. H. & Pi, S. Y., *Fluctuations in the new inflationary universe*, Phys. Rev. Lett., 49, 1110 (1982)
- [61] Guzzo, L., *Large-scale structure at the turn of the millennium*, in Paul, J., et al. eds, Abstracts of the 19th Texas Symposium on Relativistic Astrophysics and Cosmology, CEA Saclay, p 510 (1998)

- [62] Haiman, Z., Barkana, R., & Ostriker, J. P., *Warm dark matter, small scale crisis, and the high redshift universe*, preprint astro-ph/0103050 (2001)
- [63] Hanany, S. et al., *MAXIMA-1: A measurement of the Cosmic Microwave Background anisotropy on angular scales of 10'*, ApJ, 545, L5 (2000)
- [64] Hawking, S. W., *The development of irregularities in a single bubble inflationary universe*, Physics Letters, 115B, 295 (1982)
- [65] Heavens, A. F. & Sheth, R. K., *The correlation of peaks in the microwave background*, MNRAS, 310, 1062 (1999)
- [66] Heavens, A. F. & Gupta, S., *Full-sky correlations of peaks in the microwave background*, MNRAS, 324, 960 (2001)
- [67] Hernquist, L., *An analytical model for spherical galaxies and bulges*, ApJ, 356, 359 (1990)
- [68] Hill, C. T., Steinhardt, P. J., & Turner, M., *Coherent peculiar velocities and periodic redshifts*, ApJ, 366, L57 (1991)
- [69] Hogan, C. J. & Dalcanton, J. J., *New dark matter physics: clues from halo structure*, Phys. Rev. D, 62, 063511 (2000)
- [70] Hui, L., *Unitarity bounds and the cuspy halo problem*, Phys.Rev.Lett, 86, 3467 (2001)
- [71] Jenkins, A., Frenk, C. S., Pearce, F. R., Thomas, P. A., Colberg, J. M., White, S. D. M., Couchman, H. M. P., Peacock, J. A., Efstathiou, G., Nelson, A. N. (The Virgo Consortium), *Evolution of structure in cold dark matter universes*, ApJ, 499, 20 (1998)
- [72] Jenkins, A., Frenk, C. S., White, S. D. M., Colberg, J. M., Cole, S., Evrard, A. E., Couchman, H. M. P., & Yoshida, N., *The mass function of dark matter halos*, MNRAS, 321, 372 (2001)
- [73] Jing, Y. P., *The density profile of equilibrium and nonequilibrium dark matter halos*, ApJ, 535, 30 (2000)
- [74] Jing, Y. P., & Suto, Y., *The density profiles of the dark matter halo are not universal*, ApJ, 529, L69 (2000)

- [75] Kaiser, N. & Peacock, J. A., *Power-spectrum analysis of one-dimensional redshift surveys*, ApJ, 379, 482 (1991)
- [76] Kauffmann, G., White, S. D. M., & Guiderdoni, B., *The formation and evolution of galaxies within merging dark matter haloes*, MNRAS, 264, 201 (1993)
- [77] Kauffmann, G., Colberg, J. M., Diaferio, A., & White, S. D. M., *Clustering of galaxies in a hierarchical universe - I. Methods and results at $z=0$* , MNRAS, 303, 188 (1999)
- [78] Katz, N., Weinberg, D. H., & Hernquist, L., *Cosmological simulations with TreeSPH*, ApJ, 105, 19 (1996)
- [79] Klypin, A. A., Gottlöber, S., Kravtsov, A. V., & Khokholov, A. M., *Galaxies in N-body simulations: Overcoming the overmerging problem*, ApJ, 516, 530 (1999)
- [80] Kneib, J. P., Mellier, Y., Fort, B., & Mathez, G., *The distribution of dark matter in distant cluster-lenses: modelling A 370*, Astron. Astrophys., 273, 367 (1993)
- [81] Kochanek, C. S. & White, M., *A quantitative study of interacting dark matter in halos*, ApJ, 543, 514 (2000)
- [82] Komatsu, E. & Kitayama, T., *Sunyaev-Zel'dovich fluctuations from spatial correlations between clusters of galaxies*, ApJ, 526, L1 (1999)
- [83] Komatsu, E., Kitayama, T., Refregier, A., Spergel, D. N., & Pen, U.-L., *CMB anisotropy from spatial correlation of clusters of galaxies*, preprint astro-ph/0012196 (2000)
- [84] Kogut et al., *Dipole anisotropy in the COBE Differential Microwave Radiometers first-year sky maps*, ApJ, 419, 1 (1993)
- [85] Kompaneets, A. S., Soviet Physics JETP, 4, 730 (1957)
- [86] Koo, D. C., Ellmann, N., Kron, R. G., Munn, J. A., Szalay, A. S., Broahurst, T. J., & Ellis, R. S., *Deep pencil-beam redshift surveys as probes of large scale structure*, in Chiancarini, G., Iovino, A., & Maccagni, D. eds., Observational Cosmology (1993)

- [87] Kravtsov, A. V., Klypin, A. A., Bullock, J. S., & Primack, J. R., *The cores of dark matter-dominated galaxies: Theory versus observations*, ApJ, 502, 48 (1998)
- [88] Kurki-Suonio, H., Matthews, G. J., & Fuller, G. M., *Deviation from periodicity in the large-scale distribution of galaxies*, ApJ, 356, 5 (1990)
- [89] Lahav, O., Rees, M. J., Lilje, P. B., & Primack, J. R., *Dynamical effects of the cosmological constant*, MNRAS, 251, 128 (1991)
- [90] Lange, A. E. et al., *Cosmological parameters from the first results of Boomerang*, Phys.Rev.D, 630, 411 (2001)
- [91] Lacey, C. & Silk, J., *Tidally triggered galaxy formation. I - Evolution of the galaxy luminosity function*, ApJ, 381, 14 (1991)
- [92] Lee, A. T. et al., *A high spatial resolution analysis of the MAXIMA-1 cosmic microwave background anisotropy data*, ApJ, 561, 7 (2001)
- [93] Lewis, G. F., Babul, A., Katz, N., Quinn, T., Hernquist, L., & Weinberg, D. H., *The effects of gasdynamics, cooling, star formation, and numerical resolution in simulations of cluster formation*, ApJ, 536, 623 (2000)
- [94] Luppino, G. A., Gioia, I. M., Annis, J., Fevre, O., & Hammer, F., *The complex, gravitationally lensed arc system in the X-ray-selected cluster of galaxies MS0440+0204*, ApJ, 416, 444 (1993)
- [95] Ma, C. P. & Fry, J. N., *The nonlinear kinetic Sunyaev-Zeldovich effect*, preprint astro-ph/0106342 (2001)
- [96] MacFarland, T., Couchman, H. M. P., Pearce, F. R., & Pichlmeier, J., *A new parallel P3M code for very large-scale cosmological simulations*, New Astronomy, 8, 687 (1998)
- [97] Machacek, M. E., *Growth of adiabatic perturbations in self-interacting dark matter*, ApJ, 431, 41 (1994)
- [98] MacLow, M. M., & Ferrara, A., *Starburst-driven mass loss from dwarf galaxies: efficiency and metal ejection*, ApJ, 513, 142 (1999)
- [99] Madox, S. J., Efstathiou, G., & Sutherland, W. J., *The APM Galaxy Survey - III. an analysis of systematic errors in the angular correlation function and cosmological implications*, MNRAS, 283, 1227 (1996)

- [100] Meiburg, E., *Comparison of the molecular dynamics method and the direct simulation Monte Carlo technique for flows around simple geometries*, Physics of Fluids, 29, 10 (1986)
- [101] Meneghetti, M., Yoshida, N., Bartelmann, M., Moscardini, L., Springel, V., Tormen, G., & White, S. D. M., *Giant cluster arcs as a constraint on the scattering cross-section of dark matter*, MNRAS, 325, 435 (2001)
- [102] Miralda-Escude, J., *Gravitational lensing by a cluster of galaxies and the central cD galaxy: measuring the mass profile*, ApJ, 438, 514 (1995)
- [103] Miralda-Escude, J., *A test of the collisional dark matter hypothesis from cluster lensing*, ApJ, 564, 60 (2002)
- [104] Mo, H. J. & Mao, S., *The Tully-Fisher relation and its implications for the halo density profile and self-interacting dark matter*, MNRAS, 318, 163 (2000)
- [105] Mo, H. J. & White, S. D. M., *An analytic model for the spatial clustering of dark matter haloes*, MNRAS, 282, 347 (1996)
- [106] Molnar, S. M. & Birkinshaw, M., *Contributions to the power spectrum of cosmic microwave background from fluctuations caused by clusters of galaxies*, ApJ, 537, 542 (2000)
- [107] Monaghan, J. J., *Smoothed Particle Hydrodynamics*, Annual Review of Astronomy and Astrophysics, 30, 543 (1992)
- [108] Moore, B., *Evidence against dissipationless dark matter from observations of galaxy haloes*, Nature, 370, 629 (1994)
- [109] Moore, B., *Dark matter*, Philosophical Transaction of the Royal Society of London A, 357, 3259 (2000)
- [110] Moore, B., Ghigna, S., Governato, F., Lake, G., Quinn, T., Stadel, J., & Tozzi, P., *Dark matter substructure within galactic halos*, ApJ, 524, L19 (1999a)
- [111] Moore, B., Quinn T., Governato, F., Stadel, J., & Lake, G., *Cold collapse and the core catastrophe*, MNRAS, 310, 1147 (1999b)
- [112] Moore, B., Gelato, S., Jenkins, A., Pearce, F. R., & Quillis, V., *Collisional versus collisionless dark matter*, ApJ, 535, 21 (2000)

- [113] Morikawa, M., *Oscillating universe: the periodic redshift distribution of galaxies with a scale $128h^{-1}$ megaparsecs at the Galactic Poles*, ApJ, 362, L37 (1990)
- [114] Narlikar, J. V. & Padmanabhan, T., *Inflation for astronomers*, Annual Review of Astronomy and Astrophysics, 29, 325 (1991)
- [115] Navarro, J., *The cosmological significance of disk galaxy rotation curves*, preprint astro-ph/9807084 (1998)
- [116] Navarro, J., Frenk, C. S., & White, S. D. M., *Simulations of X-ray clusters*, MNRAS, 275, 720 (1995)
- [117] Navarro, J., Frenk, C. S., & White, S. D. M., *The structure of cold dark matter halos*, ApJ, 462, 563 (1996)
- [118] Navarro, J., Frenk, C. S., & White, S. D. M., *A universal density profile from hierarchical clustering*, ApJ, 490, 493 (1997)
- [119] Navarro, J. & Steinmetz, preprint astro-ph/9908114 (1999)
- [120] Netterfield, C. B. et al., *A measurement by BOOMERANG of multiple peaks in the angular power spectrum of the cosmic microwave background*, preprint astro-ph/0104460 (2001)
- [121] Ostriker, J. P., *Collisional dark matter and the origin of massive black holes*, Phys.Rev.Lett, 84, 5258 (2000)
- [122] Ostriker, J. P. & Steinhardt, P. J., *The observational case for a low density universe with a non-zero cosmological constant*, Nature, 377, 600 (1995)
- [123] Padmanabhan, T., *Structure formation in the universe*, Cambridge University Press (1993)
- [124] Park, C. & Gott, J. R., *Simulation of deep one- and two-dimensional redshift surveys*, MNRAS, 249, 288 (1991)
- [125] Pearce, F. R., Jenkins, A., Frenk, C. S., Colberg, J. M., White, S. D. M., Thomas, P. A., Couchman, H. M. P., Peacock, J. A., Efstathiou, G. (The Virgo Consortium), *A simulation of galaxy formation and clustering*, ApJ, 521, L99 (1999)

- [126] Peebles, P. J. E., *The large scale structure of the universe*, Princeton University Press (1980)
- [127] Peebles, P. J. E. & Juskiewicz, R., *Small-scale anisotropy of the cosmic background radiation and scattering by cloudy plasma*, ApJ, 509, 483 (1998)
- [128] Penzias, A. A. & Wilson, R. W., *Measurement of excess antenna temperature at 4080 Mc/sec*, ApJ, 142, 419 (1965)
- [129] Phillips, P. R., *Calculation of the kinetic Sunyaev-Zel'dovich effect from the Boltzmann equation*, ApJ, 455, 419 (1995)
- [130] Pierre, M., *Probes for the large-scale structure*, Astron. Astrophys., 229, 7 (1990)
- [131] Refregier, A. & Teyssier, R., *Numerical and analytical predictions for the large-scale Sunyaev-Zel'dovich effect*, preprint astro-ph/0012086 (2000)
- [132] Refregier, A., Komatsu, E., Spergel, D. N., & Pen, U.-L., *The power spectrum of the Sunyaev-Zel'dovich effect*, Phys. Rev. D, 611, 79 (2000)
- [133] Rephaeli, Y., *Comptonization of the cosmic microwave background*, Annual Review of Astronomy and Astrophysics, 33, 541 (1995)
- [134] Riess, A. G. et al., *Observational evidence from supernovae for an accelerating universe and a cosmological constant*, Astronomical Journal, 116, 1009 (1998)
- [135] Ritchie, B. W. & Thomas, P. A., *Multiphase Smoothed-Particle Hydrodynamics*, MNRAS, 323, 743 (2001)
- [136] Sato, K., *First-order phase transition of a vacuum and the expansion of the Universe*, MNRAS, 195, 467 (1981)
- [137] Seljak, U. & Zaldarriaga, M., *A line-of-sight integration approach to cosmic microwave background anisotropies*, ApJ, 469, 437 (1996)
- [138] Seljak, U., Burwell, J., & Pen, Ue-Li., *Sunyaev-Zel'dovich effect from hydrodynamical simulations: Maps and low order statistics*, Phys. Rev. D, 630, 619 (2001)
- [139] Sachs, R. K. & Wolfe, A. M., *Perturbations of cosmological model and angular variations of the microwave background*, ApJ, 147, 7 (1967)

- [140] Schaeffer, R. & Silk, J., *Cold, warm, or hot dark matter - Biased galaxy formation and pancakes*, ApJ, 332, 1 (1988)
- [141] Sheth, R. K. & Diaferio, A., *Peculiar velocities of galaxies and clusters*, MNRAS, 322, 901 (2001)
- [142] Sheth, R. K. & Tormen, G., *Large-scale bias and the peak background split*, MNRAS, 308, 119 (1999)
- [143] Sigad, Y., Branchini, E., & Dekel, A., *Measuring the nonlinear biasing function from a galaxy redshift survey*, ApJ, 540, 62 (2000)
- [144] Silk, J. & White, S. D. M., *The determination of Q_0 using X-ray and microwave observations of galaxy clusters*, ApJ, 226, 103 (1978)
- [145] da Silva, A. C., Barbosa, D., Liddle, A., & Thomas, P. A., *Hydrodynamical simulations of the Sunyaev-Zel'dovich effect*, MNRAS, 317, 37 (2000)
- [146] Smoot, G. F., Bennet, C. L., Kogut, A., Wright, E. L., Aymon, J., Boggess, N. W., Cheng, E. S., de Amici, G., Gulkis, S., Hauser, M. G., Hinshaw, G., Jackson, P. D., Janssen, M., Kaita, E., Kensall, T., Keegtra, P., Lineweaver, C., Loewenstein, K., Lubin, P., Mather, J., Meyer, S. S., Moseley, S. H., Murdock, T., Rokke, L., Silverberg, R. F., Tenorio, L., Weiss, R., & Wilkinson, D. T., *Structure in the COBE Differential Microwave Radiometer first year maps* ApJ, 396, L1 (1992)
- [147] Somerville, R. S. & Primack, J. R., *Semi-analytic modelling of galaxy formation: the local Universe*, MNRAS, 310, 1087 (1999)
- [148] Somerville, R. S., Lemson, G., Sigad, Y., Dekel, A., Kauffmann, G., & White, S. D. M., *Non-linear stochastic galaxy biasing in cosmological simulations*, MNRAS, 320, 289 (2001)
- [149] Spergel, D. N. & Steinhardt, P. J., *Observational evidence for self-interacting cold dark matter*, Phys.Rev.Lett, 84, 3760 (2000)
- [150] Springel, V., *On the formation and evolution of galaxies*, PhD thesis, Ludwig-Maximilian University, Munich. (1999)
- [151] Springel, V., Yoshida, N., & White, S. D. M., *GADGET: A code for collisionless and gasdynamical cosmological simulations*, New Astronomy, 6, 79 (2001a)

- [152] Springel, V., White, M., & Hernquist, L., *Hydrodynamic simulations of the Sunyaev-Zel'dovich effects*, ApJ, 549, 681 (2001b)
- [153] Springel, V., Tormen, G., White, S. D. M., & Kauffmann, G., *Populating a cluster of galaxies*, MNRAS, 328, 726 (2001c)
- [154] Starobinsky, A. A., *Dynamics of phase transition in the new inflationary universe scenario and generation of perturbations*, Physics Letters, 117B, 175 (1982)
- [155] Steinmetz, M. & White, S. D. M., *Two-body heating in numerical galaxy formation experiments*, MNRAS, 288, 545 (1997)
- [156] SubbaRao, M. U. & Szalay, A. S., *Statistics of pencil beams in Voronoi foams*, ApJ, 391, 483 (1992)
- [157] SuginoHara, T. & Ostriker, J. P., *The effect of cooling on the density profile of hot gas in clusters of galaxies: is additional physics needed?*, ApJ, 577, 16 (1998)
- [158] Sunyaev, R. A. & Zel'dovich, Ya. B., *Microwave background radiation as a probe of the contemporary structure and history of the Universe*, Annual Review of Astronomy and Astrophysics, 18, 537 (1980a)
- [159] Sunyaev, R. A. & Zel'dovich, Ya. B., *The velocity of clusters of galaxies relative to the microwave background - The possibility of its measurement*, MNRAS, 190, 413 (1980b)
- [160] Sutherland, R. S. & Dopita, M. A., *Cooling functions for low-density astrophysical plasmas*, ApJS, 888, 253 (1993)
- [161] Szalay, A. S., Koo, D. C., Ellis, R. S., & Broadhurst, T. J., *Analysis of the large scale structure with deep pencil beam surveys*, in S. Holt, C. Bennett, & V. Trimble eds., *After the First Three Minutes*, (New York:AIP), p435 (1991)
- [162] Totsuji, H. & Kihara, T., *The correlation function for the distribution of galaxies*, Publication of the Astronomical Society of Japan, 21, 221 (1969)
- [163] Tully, R. B, Scaramella, R., Vettolani, G., & Zamorani, G., *Possible geometric patterns in 0.1c scale structure*, ApJ, 388, 9 (1992)

- [164] Tyson, J. A., Kochanski, G. P., & Dell'Antonio, I. P., *Detailed mass map of CL 0024+1654 from strong lensing*, ApJ, 498, 107 (1998)
- [165] Tytler, D., O'Meara, J. M., Suzuki, N., & Lubin, D., *Deuterium and the baryon density of the universe*, Physics Reports, 333, 409 (2000)
- [166] Valageas, P., Balbi, A., & Silk, J., *Secondary CMB anisotropies from the kinetic SZ effect*, Astron. Astrophys., 367, 1 (2000)
- [167] van de Weygaert, R., *Quasi-periodicity in deep redshift surveys*, MNRAS, 249, 159 (1991)
- [168] van den Bosch, F. C., *Semi-analytical models for the formation of disk galaxies: I. Constraints from the Tully-Fisher relation*, ApJ, 530, 177 (2000)
- [169] van den Bosch, F. C., Robertson, B. E., Dalcanton, J. J., & de Blok, W. J. G., *Constraints on the structure of dark matter halos from the rotation curves of low surface brightness galaxies*, AJ, 119, 1579 (2000)
- [170] van den Bosch, F. C. & Swaters, R. A., *Dwarf galaxy rotation curves and the core problem of dark matter halos*, MNRAS, 325, 1017 (2001)
- [171] Weinberg, D. H., Hernquist, L., & Katz, N., *Photoionization, numerical resolution, and galaxy formation*, ApJ, 477, 8 (1997)
- [172] White, S. D. M. & Rees, M. J., *Core condensation in heavy halos - A two-stage theory for galaxy formation and clustering*, MNRAS, 183, 341 (1978)
- [173] White, S. D. M., *Formation and evolution of galaxies*, Schaeffer, R., Silk, J., Zinn-Justin, J., eds. *Cosmology and Large Scale Structure*, Les Houches Lectures, (1994)
- [174] White, S. D. M., & Frenk, C. S., *Galaxy formation through hierarchical clustering*, ApJ, 379, 52 (1991)
- [175] White, S. D. M., Efstathiou, G., & Frenk, C. S., *The amplitude of mass fluctuations in the Universe*, MNRAS, 262, 1023 (1993)
- [176] White, S. D. M., Frenk, C. S., & Davis, M., *Clustering in a neutrino-dominated universe*, ApJ, 274, 1 (1983)

- [177] White, S. D. M., Frenk, C. S., Davis, M., & Efstathiou, G., *Clusters, filaments, and voids in a universe dominated by cold dark matter*, ApJ, 313, 505 (1987)
- [178] White, S. D. M., Navarro, J. F., Evrard, A. E., & Frenk, C. S., *The baryon content of galaxy clusters: a challenge to cosmological orthodoxy*, Nature, 366, 429 (1993)
- [179] White, S.D.M. & Springel, V., *Where are the first stars ?*, in Weiss A. et al., eds, The First Stars, Proc. MPA/ESO workshop (1999)
- [180] Willmer, C. N. A., Koo, D. C., Szalay, A. S. & Kurtz, M. J., *A medium-deep redshift survey of a minislice at the North Galactic Pole*, ApJ, 437, 560 (1994)
- [181] Yoshida, N., Springel, V., White, S. D. M, & Tormen, G., *Collisional dark matter and the structure of dark halos*, ApJ, 535, L103 (2000a)
- [182] Yoshida, N., Springel, V., White, S. D. M, & Tormen, G., *Weakly self-interacting dark matter and the structure of dark halos*, ApJ, 544, L87 (2000b)
- [183] Yoshida, N., Colberg, J., White, S. D. M., Evrard, A. E., MacFarland, T. J., Couchman, H. M. P., Jenkins, A., Frenk, C. S., Pearce, F. R., Efstathiou, G., Peacock, J. A., Thomas, P. A. (The Virgo Consortium), *Simulations of deep pencil-beam redshift surveys*, MNRAS, 325, 803 (2001a)
- [184] Yoshida, N., Sheth, R. K., & Diaferio, A., *Non-Gaussian CMB temperature fluctuations from peculiar velocities of clusters*, MNRAS, 328, 669 (2001b)
- [185] Yoshida, N., Stoehr, F., Springel, V., & White, S. D. M., *Gas cooling in simulations of the galaxy population*, submitted to MNRAS(2001c)
- [186] Zel'dovich, Ya B., *Gravitational instability: an approximate theory for large density perturbations*, Astron. Astrophys., 5, 84 (1970)

ACKNOWLEDGEMENT

I had a pleasant environment, excellent colleagues, a great advisor, and a wonderful family, each of these an order of magnitude better than the norm. Simple mathematics show that I was supposed to be a factor of $10 \times 10 \times 10 \times 10 = 10000$ times brilliant... I was not, obviously. The following is hence a mixture of my great gratitude to those who helped me during my PhD days and a little regret for not having made this thesis a factor of 10000 greater.

Dear Simon: I was not smart enough to fully understand complex physics of galaxy formation taught by you, but I think I have learned *management* over the past three years. I had a unique and invaluable opportunity to know how a big scientific project is managed by a great leader. Although some facts in cosmology I studied in standard text books might become dated in the future, what I have learned from you will definitely be my *standard* for the rest of my life. I thank you.

I enjoyed working at MPA, where I met many nice colleagues. They are: Robi Banerjee, Rigo Casas, Jörg Colberg, Conrad Cramphorn, Frode Hansen, Simone Marri, Hugues Mathis, Martin Reinecke, Volker Springel, Felix Stöhr, Saleem Zaroubi. I am also grateful to my Virgo collaborators Adrian Jenkins, Frazer Pearce, Ben Moore, Carlos Frenk.

I never managed to solve problems in my disk system by myself. Nevertheless, due to helpful advices from our system administrators, I could carry out computational works without difficulties. I'd like to thank to those who offered technical and computational supports: Nobert Grüner, Hans-Werner Paulsen, Achim Weiss, and Manfred Reuter at MPA for their help in local computing systems, and Tom MacFarland, Jacob Pichlmeier and Ingeborg Weidl for their support in supercomputing.

Secretaries at MPA helped me in various (and many) occasions. Thank you very much, Cornelia, Kate, and Maria.

My collaborators made an enormous effort in completing our works. Thanks are due to Massimo Meneghetti, Matthias Bartelmann, Bepi Tormen, Jens Schmalzing, Antonaldo Diaferio, and Ravi Sheth. I am also grateful to Rashid Sunyaev, Naoshi Sugiyama, and Tom Abel for fruitful discussions.

Yuka-san, to express my gratitude to you, I need probably tens of thousands of pages. Writing this thesis was not as romantic as writing love letters to you, but finally I could finish this up. Thank you for all your help during my PhD days, especially for being with me.

This work was supported by Sonderforschungsbereich 375 and DAAD.

L E B E N S L A U F

Name	Naoki Yoshida
Geburtsdatum	4. September 1973
Geburtsort	Chiba, Japan
Familienstand	verheiratet mit Yuka Yoshida
Schulbildung	
1981 - 1983	Elementary school, Kobe, Japan
1987 - 1989	Junior high school, Kobe, Japan
1989 - 1992	Nada high school, Kobe, Japan
31. März 1992	Abitur (Koutougakkou Sotsugyou)
Studium der Ingenieurwissenschaften	
1992 - 1998	Department of Aerospace Engineering University of Tokyo
28. März 1996	Bachelor of Engineering
30. März 1998	Master of Engineering
Studium der Physik	
1997 - 1998	Kungl Tekniska Högskolan, Schweden
2. Juni 1998	Teknologi Licentiat
Promotion in Astrophysik	
1998 - 2001	Max-Planck-Institut für Astrophysik Betreuer Prof. Dr. Simon D. M. White Thema „Numerical Simulations of the Formation of Large-Scale Structure of the Universe”
Stipendien	
1996 - 1998	45th Teijin Kumura Shougakusei
1997 - 1998	Axelson och Margaret Ax:son Johnsons Stiftelse
1999 - 2001	DAAD Stipendium

München, den